

REPORT DOCUMENTATION PAGE			Form Approved OMB No. 0704-0188		
Public reporting burden for this collection of information is estimated to average 1 hour per response, including the time for reviewing instructions, searching existing data sources, gathering and maintaining the data needed, and completing and reviewing this collection of information. Send comments regarding this burden estimate or any other aspect of this collection of information, including suggestions for reducing this burden to Department of Defense, Washington Headquarters Services, Directorate for Information Operations and Reports (0704-0188), 1215 Jefferson Davis Highway, Suite 1204, Arlington, VA 22202-4302. Respondents should be aware that notwithstanding any other provision of law, no person shall be subject to any penalty for failing to comply with a collection of information if it does not display a currently valid OMB control number. PLEASE DO NOT RETURN YOUR FORM TO THE ABOVE ADDRESS.					
1. REPORT DATE (DD-MM-YYYY) 31-03-2012		2. REPORT TYPE Final Performance Report		3. DATES COVERED (From - To) 01-09-2008 to 31-03-2012	
4. TITLE AND SUBTITLE Experimental Studies of Coal and Biomass Fuel Synthesis and Flame Characterization for Aircraft Engines			5a. CONTRACT NUMBER		
			5b. GRANT NUMBER FA9550-10-1-0344		
			5c. PROGRAM ELEMENT NUMBER 61102F		
6. AUTHOR(S) R. K. Agrawal, J. P. Gore, F. H. Ribeiro, W. N. Delgass, R. Lucht, L. Qiao, S. Naik, A. Smeltz, D. Guildenbecher, I. Sircar, V. Kumar, A. Sane			5d. PROJECT NUMBER 2308		
			5e. TASK NUMBER BX		
			5f. WORK UNIT NUMBER		
7. PERFORMING ORGANIZATION NAME(S) AND ADDRESS(ES) AND ADDRESS(ES) Purdue University Energy Center Mann Hall, Room 266 203 Martin Jischke Drive West Lafayette, IN 47907-2022			8. PERFORMING ORGANIZATION REPORT NUMBER		
9. SPONSORING / MONITORING AGENCY NAME(S) AND ADDRESS(ES) Air Force Office of Scientific Research 875 North Randolph St. Suite 325, Room 3112 Arlington, VA 22203-1768			10. SPONSOR/MONITOR'S ACRONYM(S)		
			11. SPONSOR/MONITOR'S REPORT NUMBER(S) AFRL-OSR-VA-TR-2012-1056		
12. DISTRIBUTION / AVAILABILITY STATEMENT Approved for public release; distribution is unlimited					
13. SUPPLEMENTARY NOTES					
14. ABSTRACT The broad objective of the research team is to establish the feasibility of an innovative idea to develop a commercially and technically viable integrated coal/biomass-to-liquid jet fuel synthesis process while mitigating the CO ₂ penalty. The production of transportation fuel from domestic coal and biomass sources would assure the U.S. Air Force a dependable and secure fuel supply. However, low efficiencies of the existing coal/biomass-to-liquid fuel processes, high capital and operating costs of the coal gasifiers and lack of combustion characteristics of the liquid fuel from coal/biomass are some of the major barriers to their use. As a result, there is a need for fundamental scientific and synergistic research in catalytic biomass fast-hydrolysis and advanced coal gasification studies. Synthetic liquid fuel combustion studies were conducted in the previous two years of the project and are also in progress elsewhere. The objective of this project was to develop experimental facilities for addressing specific scientific issues associated with the utilization of biomass and coal to produce appropriate aviation fuels.					
15. SUBJECT TERMS Biomass fast hydrolysis, hydrodeoxygenation, and coal gasification					
16. SECURITY CLASSIFICATION OF: Unclassified			17. LIMITATION OF ABSTRACT UL	18. NUMBER OF PAGES 72	19a. NAME OF RESPONSIBLE PERSON Dr. Chiping Li (chiping.li@afosr.af.mil)
a. REPORT Unclassified	b. ABSTRACT Unclassified	c. THIS PAGE Unclassified			19b. TELEPHONE NUMBER (include area code) (703)696-8478

Experimental Studies of Coal and Biomass Fuel Synthesis and Flame Characterization for Aircraft Engines

AFOSR Grant Number: FA9550-10-1-0344

Final Performance Report

Report Period: September 1, 2008 to March 31, 2012

Prepared by:

Dr. Rakesh Agrawal (PI)

765-494-4811

765-494-0805 (fax)

agrawalr@purdue.edu

Dr. Jay Gore (Co-PI)

765-494-1610

765-496-9322 (fax)

gore@purdue.edu

Dr. Fabio H. Ribeiro (Participating Investigator) Dr.

W. Nicholas Delgass (Participating Investigator) Dr.

Robert P. Lucht (Participating Investigator)

Dr. Li Qiao (Participating Investigator)

Dr. Sameer Naik

Dr. Andrew Smeltz

Dr. Daniel Guildenbecher

Mr. Indraneel Sircar Mr.

Vinod Kumar

Mr. Anup Sane

School of Chemical Engineering School
of Mechanical Engineering School of
Aeronautics and Astronautics

Purdue University
West Lafayette, IN 47907

Table of Contents

Executive Summary	4
1.0 Biomass Fast-Hydropyrolysis	5
1.1 Fundamental Studies of Fast-Pyrolysis and Fast-Hydropyrolysis	5
1.2 Micro-Scale Batch Fast-Hydropyrolysis Reactor	11
1.3 Continuous High-Pressure Fast-Hydropyrolysis Reactor	17
1.4 References	22
2.0 Investigation of Coal and Biomass Gasification using <i>In-situ</i> Diagnostics	23
2.1 Introduction	23
2.2 Continuous-Flow Experimental Arrangement	24
2.3 Fixed Bed System	41
2.4 Mathematical Modeling of Coal Gasification	54
2.5 References	63
3.0 Conclusions	65
4.0 Participating Personnel	66
5.0 Publications and Presentations	68
5.1 Publications	68
5.2 Conference Papers and Presentations	69

Executive Summary**AFOSR Grant Number: FA9550-08-1-0456****Project Title:**

Experimental Studies of Coal and Biomass Fuel Synthesis and Flame Characterization for Aircraft Engines (Final Performance Report)

Project Period: September 1, 2008 to March 31, 2012**Report Period:** September 1, 2008 to March 31, 2012**Date of Report:** March 31, 2012**Contacts:**Rakesh Agrawal Phone: 765-494-4811, E-mail: agrawalr@purdue.eduJay Gore, Phone: 765-494-1610, E-mail: gore@purdue.edu**Project Objective:**

The broad objective of the research team is to establish the feasibility of an innovative idea to develop a commercially and technically viable integrated coal/biomass-to-liquid jet fuel synthesis process while mitigating the CO₂ penalty. The production of transportation fuel from domestic coal and biomass sources would assure the U.S. Air Force a dependable and secure fuel supply. However, low efficiencies of the existing coal/biomass-to-liquid fuel processes, high capital and operating costs of the coal gasifiers and lack of combustion characteristics of the liquid fuel from coal/biomass are some of the major barriers to their use. As a result, there is a need for fundamental scientific and synergistic research in catalytic biomass fast-hydropyrolysis, advanced coal gasification and liquid fuel combustion studies. The objective of this project was to develop experimental facilities for addressing specific scientific issues associated with the utilization of biomass and coal to produce appropriate aviation liquid fuels.

Fundamentals of fast-pyrolysis and fast-hydropyrolysis were systematically studied using micro-scale batch reactor systems. A fixed-bed catalytic reactor was designed, built and integrated with a micro-scale batch fast-hydropyrolysis reactor, and hydrodeoxygenation (HDO) of hydropyrolysis vapors over a 2% Pt/Al₂O₃ water-gas-shift (WGS) catalyst was studied. After testing several prototype reactors, a continuous high-pressure cyclone-type fast-hydropyrolysis reactor and a downstream fixed-bed catalytic reactor were designed, built and tested at high pressures (up to 50 bar) and in the presence of candidate HDO catalysts. Findings from this work include: heating rates of 500 to 1000 °C s⁻¹ are needed to minimize char formation from cellulose; at high heating rates and pressures of ~25 bar, cellulose pyrolysis in the presence of He and H₂ gives similar product distributions, and downstream hydrodeoxygenation requires a balance of acid and metal functions on the catalyst.

A continuous flow reactor and a fixed bed reactor were built for the experimental investigation of coal and biomass gasification at high-pressures. In-situ diagnostics in the form of tunable-diode-laser-absorption-spectroscopy (TDLAS) was developed to study the gasification rates and associated transport and kinetics. The TDLAS technique was used to probe CO species concentration as a marker of gasification progress. In both cases, in-situ measurements were correlated with product gas composition analysis using a gas chromatograph and a FTIR based multi-gas-analyzer. Material characterization techniques were used to assess the structural changes of the solid feedstock. In addition, detailed chemistry involving multiphysics models were developed to understand the gasification process from a fundamental perspective.

1.0 Biomass Fast-Hydropyrolysis

The broad objective of the project is the development of a process to convert biomass, a rich resource of renewable carbon, to liquid products with high energy density to supplement liquid aviation fuels from traditional, non-renewable resources. The ultimate goal of the proposed fast-hydropyrolysis and catalytic hydrodeoxygenation process is to meet these requirements by thermally decomposing biomass into small molecules in the fuel range, while simultaneously upgrading these products to high-energy-density liquid fuels using catalysts in the presence of high-pressure hydrogen and carbon monoxide generated by coal gasification.

Year One and Year Two research programs on biomass fast-hydropyrolysis (Task 1.0) took different approaches to reactor design to construct working reactors capable of operating under high pressure conditions. Several prototype, lab-scale, fast-pyrolysis reactors with varying configurations were designed, built, and tested. Experiments with micro-scale reactor systems to better understand the fundamentals of fast-pyrolysis and fast-hydropyrolysis were also completed. A lab-scale, high-pressure, fast-hydropyrolysis reactor was built based on the results from previous reactors and fundamental studies on pyrolysis of cellulose.

The Year Three research program continued a two-pronged approach to study various issues related to the utilization of hydrogen (H_2) and carbon monoxide (CO), generated by coal gasification, for biomass fast-hydropyrolysis (FHP) and subsequent hydrodeoxygenation (HDO) to produce a liquid product suitable for upgrading or directly usable as a jet fuel. The first approach utilized a lab-scale, continuous-flow, high-pressure, cyclone-type, FHP reactor and a secondary fixed-bed catalytic reactor located downstream of the FHP reactor for performing product vapor upgrading and water-gas-shift (WGS) reactions. This reactor system, in addition to allowing study of the fundamentals of FHP, also allowed us to understand better the practical issues associated with operating a FHP reactor system. However, this approach did not allow us to quickly screen reaction conditions and catalysts that could result in a product distribution optimal for liquid fuel production. Additionally, the control over process variables was coarse at best, which made fundamental studies difficult. Therefore, the second approach was to study FHP, catalytic product upgrading and WGS reactions using a micro-scale, batch FHP reactor which was capable of accurately controlling variables, such as particle heating rate, which were believed to be important for controlling the product distribution. Furthermore, the system was capable of quick screening of process conditions and catalysts that were also useful for the continuous reactor. In the subsequent sections, both experimental apparatuses are briefly described, along with an account of progress made in accomplishing specific tasks of the research project.

1.1 Fundamental Studies of Fast-Pyrolysis and Fast-Hydropyrolysis

In order to optimize the fast-hydropyrolysis process and maximize selectivity towards a liquid product, it is essential to understand the fundamentals of char formation. Heating rate of the biomass particles is an important factor influencing the formation of undesirable char by-products. In Year Two research, the objective was to get an estimate of minimum heating rate required to avoid char formation in cellulose pyrolysis, which would aid in the design of the micro-scale batch and continuous high-pressure FHP reactors. In Year Three, the aim was to accurately quantify this relationship by precisely measuring the amount of char formed in cellulose pyrolysis at different heating rates and in the presence of H_2 /CO/ CO_2 mixtures.

1.1.1 Experimental Description

In Year Two research, experiments were conducted in one of two custom, six-sided, stainless-steel, micro-reactor chambers with internal volumes of roughly 0.4 L and equipped with borosilicate viewports to allow for monitoring of the reaction, as shown in Figure 1.1. The two reactors differed only in their maximum operating pressures. Biomass heating was performed using a Pyroprobe (Pyroprobe 5200, CDS Analytical, Oxford, PA), which consists of a resistively heated platinum ribbon approximately 2.1 mm x 35 mm x 0.1 mm.

Cellulose particles with a mean diameter of 50 μm were loaded onto the surface of the pyroprobe, which was inserted into the chamber through a modified 2 $\frac{3}{4}$ " flange, and the system was flushed with inert gas to remove any oxygen. The particles were held in place by electrostatic interactions with the surface in a way that prevents agglomeration or vertical stacking of particles. This procedure was a key aspect of the experiment because heat

transfer to the sample was critical, and a thick layer of sample would result in thermal lag and uneven heating of each individual particle. The intimate solid-solid contact represented the ideal heat transfer scenario and, coupled with the ability to heat the samples at rates up to $20,000\text{ }^{\circ}\text{C s}^{-1}$, made this system a much better candidate for studying the fundamentals of fast-pyrolysis than a typical thermogravimetric analysis (TGA) experiment.

The cellulose samples were heated at rates representing one of three different regimes: slow, TGA-type heating ($15\text{ }^{\circ}\text{C min}^{-1}$), intermediate heating typical of pyrolysis ($200\text{ }^{\circ}\text{C s}^{-1}$), and the maximum possible rate ($20,000\text{ }^{\circ}\text{C s}^{-1}$). The gas atmosphere was also varied to determine the effects of reaction environment. Experiments were conducted at 1 bar He, 1 bar H_2 , and 30 bar He. In each experiment, the ribbon was heated to a final temperature of $600\text{ }^{\circ}\text{C}$, where it was held for 1 s before being allowed to cool back to room temperature. Pictures of the platinum ribbon were taken using an optical microscope (Olympus BX51, Olympus, Central Valley, PA) before introduction into the chamber and after reaction in order to qualitatively determine the amount of char formation.

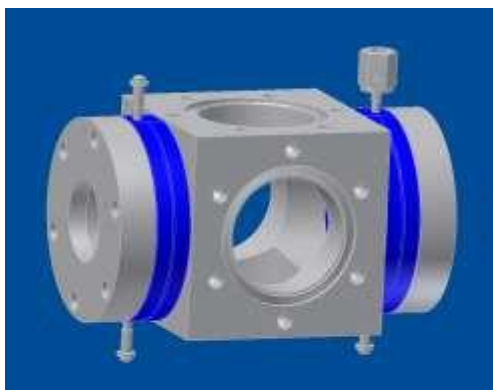


Figure 1.1: CAD drawing of the six-sided micro-reactor with two high-pressure borosilicate viewports.

In Year Three, to quantitatively study char formation during pyrolysis, a modified setup for the pyroprobe was used. The details of the experimental set-up are explained later. A crucial aspect of the study was the requirement to deposit quantifiable and reproducible amounts of cellulose onto the platinum filament of the pyroprobe. Previous experiments showed that it is necessary to load no more than a single layer of sample so that heat transfer is directed from the platinum surface to the cellulose particle rather than from one particle to an adjacent particle.

A three-step experimental method, shown in Figure 1.2, was designed to quantify char formation as a function of heating rate for cellulose. In the first step, a micro liter of an aqueous suspension of known cellulose concentration was deposited onto the platinum filament and the filament was dried at room temperature to evaporate the water. Then, the particle dispersion was observed with a standalone microscope with 20x magnification. Following pyrolysis at the desired heating rate ($^{\circ}\text{C s}^{-1}$) in $\text{H}_2/\text{CO}/\text{CO}_2$ mixtures, the pyroprobe with residual char was inserted into a decoking flow tube as shown below in Figure 1.3.

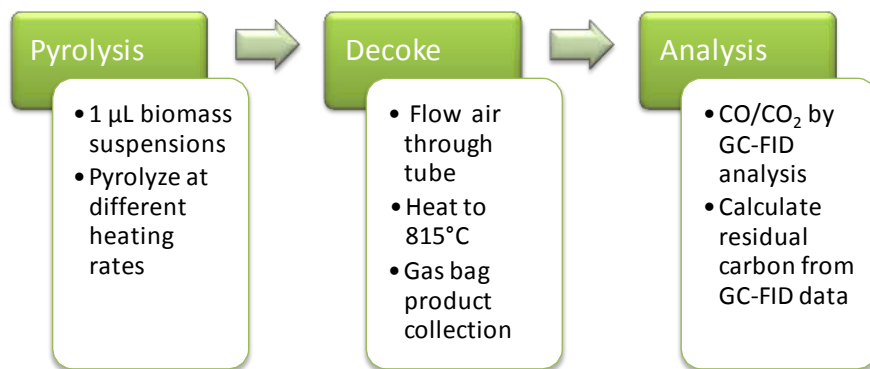


Figure 1.2: Experimental method to quantify cellulose char formation on pyroprobe.

The char deposited on the Pt filament was removed by flowing air across the filament and heating the pyroprobe to 815 °C to form CO and CO₂. In order to accurately determine the absolute amount of char present, it was necessary to collect the entire off-gas during this decoking step. To facilitate this process, firstly, a steady-state air flow rate to the vent was established by using a gas mass flow controller. Then, a solenoid valve was energized to direct the airflow from the vent to the pyroprobe. The solenoid was connected to a time-delay relay that de-energized the valve after a specified period of time and re-directed air flow from the pyroprobe back to the vent. Thus, a fixed volume of air was passed across the pyroprobe and all of the combustion products were collected in a downstream gas-sampling bag.

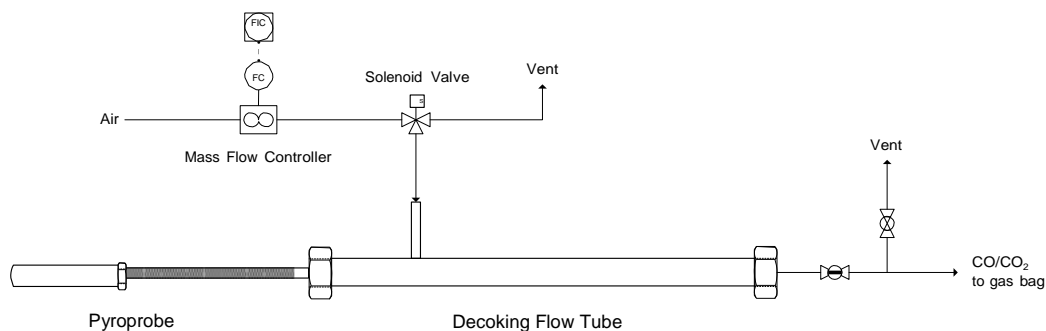


Figure 1.3: Flow diagram of test unit to quantify post-pyrolysis char from pyroprobe.

The final step was to analyze the combustion products by gas chromatography. Based on the known gas sample volume and composition of combustion products, the amount of carbon present was determined and a relationship was developed for the mass of char deposited on the platinum filament at a given pyrolysis heating rate.

1.1.2 Results and Discussion

The approximate amount and type of char formed at a given heating rate were similar at different pressures of the gas environment (1 bar and 30 bar). Heating the cellulose at 15 °C min⁻¹ resulted in a significant amount of char formation, as shown in Figure 1.4. Similar amounts of char formed after pyrolysis in atmospheric pressure helium and hydrogen at the same heating rate. The following hypothesis is consistent with the results. At a low heating rate, cellulose slowly decomposes on the surface and forms amorphous carbon structures with a high C:H ratio rather than forming lower molecular weight vapor and gaseous products. While some lighter compounds are inevitably formed, a large proportion of the original sample remains on the surface in the form of char.

Cellulose has a very ordered and regular structure, consisting of thousands of dehydrated glucose building blocks linked into long chains with little or no branching. In real biomass, however, cellulose corresponds to only around one-third of the mass, with the rest made up by hemicellulose (essentially a branched and lower molecular weight polymer made up of a variety of sugar monomers) and lignin, an amorphous, cross-linked set of molecules so random in its size and structure that no accurate model has been developed. If such a low heating rate causes the simplest of compounds found in plants to extensively char, then surely the yields of vapor products from real biomass would be unacceptable.

An interesting result was obtained by heating the cellulose at a rate of 200 °C s⁻¹ in that the char formed droplets, which left “char rings” on the surface, as shown in Figure 1.5. This observation is consistent with and confirms the phenomenon reported previously^[1.1], which showed cellulose liquefying and bubbling off the surface during pyrolysis. This heating rate, then, corresponds to a transition zone for this particle size where the heating is fast enough to allow sufficient heat transfer throughout the particle to liquefy the sample. However, the heating is still not fast enough to completely volatilize all the cellulose, resulting in the ring of char. This heating rate can be regarded as the minimum order of magnitude required for an ablative reactor to efficiently pyrolyze cellulose, since the liquefied cellulose will “stick” to the surface upon contact, and can spread out on the hot surface, resulting in a larger contact area and smaller thermal lag through the sample. A reactor operating at lower heating rates relies on the contact of an irregularly-shaped solid particle with a hot surface, which would lead to less efficient heat transfer.

A heating rate of $20,000\text{ }^{\circ}\text{C s}^{-1}$, two orders of magnitude greater than the previous one, is fast enough to cause essentially complete vaporization of the samples. Consequently, the experiments at this heating rate resulted in virtually no char being formed, Figure 1.6. While this heating rate may be difficult to obtain in a large-scale reactor, it shows that it is possible to eliminate the formation of char for simple model biomass systems.

In order to check if a heating rate in the intermediate range could eliminate char formation, experiments were conducted at $1,000\text{ }^{\circ}\text{C s}^{-1}$. It was observed that these heating rates were sufficient to eliminate the formation of char from cellulose (Figure 1.7).

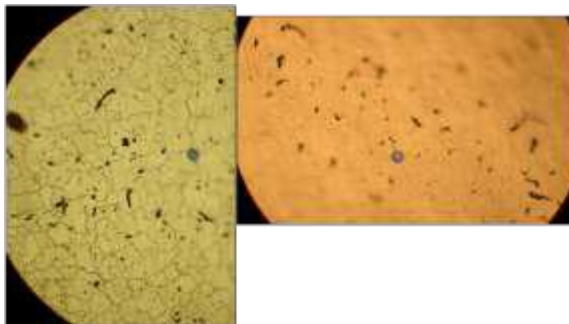


Figure 1.4: Char formed after $50\text{ }\mu\text{m}$ cellulose particles were pyrolyzed in 1 bar H_2 (left) and 1 bar He (right) at a heating rate of $15\text{ }^{\circ}\text{C min}^{-1}$. 20x magnification. The blue circles outline the same position on the platinum ribbon.



Figure 1.5: $50\text{ }\mu\text{m}$ cellulose before reaction (left) and after pyrolysis in 1 bar He at a rate of $200\text{ }^{\circ}\text{C s}^{-1}$ (right). 20x magnification. The blue circle outlines the same position on the ribbon.

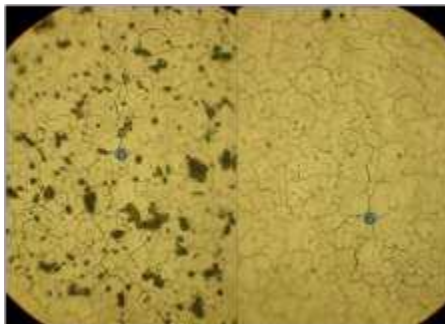


Figure 1.6: $50\text{ }\mu\text{m}$ cellulose particles on the surface of platinum ribbon (left). Char formed after pyrolysis in 1 bar H_2 at a heating rate of $20,000\text{ }^{\circ}\text{C s}^{-1}$ (right). 20x magnification. The blue circle outlines the same position on the platinum ribbon.

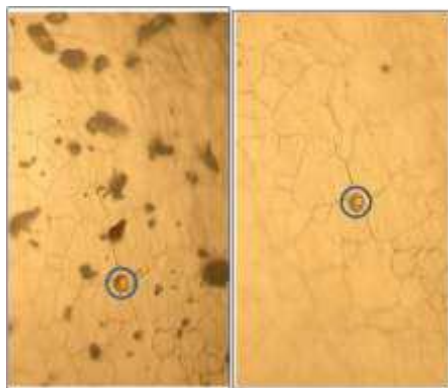


Figure 1.7: 50 μm cellulose particles on the surface of platinum ribbon (left). Char formed after pyrolysis in 1 bar He at a heating rate of $1,000\text{ }^{\circ}\text{C s}^{-1}$ (right). 20x magnification. The blue circle outlines the same position on the platinum ribbon.

In Year Three, after the construction of the test apparatus (Figure 1.3) to quantitatively study the effects of different pyrolysis heating rates and final temperatures on char formation from cellulose in $\text{H}_2/\text{CO}/\text{CO}_2$ mixtures, char formation studies were started by pyrolyzing 50 μm cellulose particles at $15\text{ }^{\circ}\text{C s}^{-1}$ in the pyroprobe in the presence of helium. The purpose of testing at this low heating rate was to form char on the platinum filament deliberately in order to determine if it can be completely removed and collected in a gasbag following an air burn. Figure 1.8 compares microscope images of the platinum filament before pyrolysis, after pyrolysis, and after decoking.

To quantify char formation, a method was developed to deposit measurable quantities of cellulose on the platinum filament of the pyroprobe and generate GC calibration curves to determine the absolute concentrations of CO and CO_2 in the decoking gas sample. Samples were deposited on the pyroprobe by preparing a suspension of cellulose particles in deionized water, adding droplets of this suspension onto the platinum filament, and drying the filament to remove the water to yield a known starting mass of cellulose. After pyrolyzing the cellulose particles at $15\text{ }^{\circ}\text{C s}^{-1}$ to a final temperature of 600°C in helium flow, the pyroprobe was cooled and transferred to the decoking apparatus. Then, the residual carbon (char) by-product was removed from the platinum filament by flowing a fixed volume of purified air across the pyroprobe and heating to $815\text{ }^{\circ}\text{C}$ at $1,000\text{ }^{\circ}\text{C s}^{-1}$. The final temperature was held for 5 minutes to ensure complete decoking. The CO and CO_2 in the decoking product gas mixture were converted to CH_4 before analysis in the FID of the GC in order to make the CO and CO_2 susceptible to the high sensitivity of FID. Microscopic inspection of the platinum filament after decoking confirmed that the char was removed. These experiments were repeated for 20 μg and 60 μg of starting mass of cellulose.

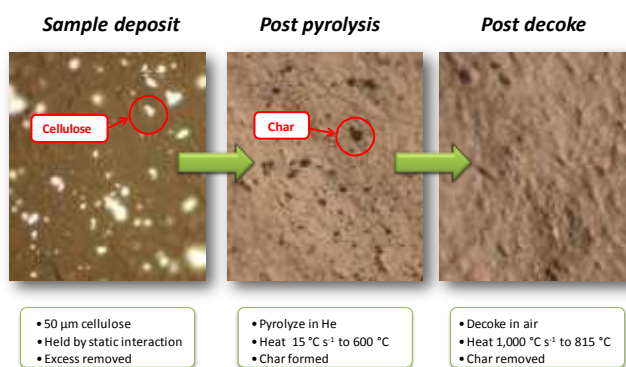


Figure 1.8: Microscope images of the platinum filament to compare the presence of cellulose, formation of char, and removal by decoking.

Table 1.1 shows the char yield, defined as the mass of char produced per mass of starting cellulose, from pyrolysis of 20 μg and 60 μg of cellulose in helium at three different heating rates of 15, 100 and $250\text{ }^{\circ}\text{C s}^{-1}$. Since the purified

air used for decoking contained trace amounts of CO and CO₂, this baseline quantity of 3.5 μg carbon was subtracted from the amount of carbon in the gas bag samples to determine the mass of char on the platinum filament. Figure 1.9 shows the variation of the char yield as a function of the heating rate for the two different starting masses of cellulose. As a general trend for the 60 μg samples, a decrease in char yield was observed from 52% to 15% as the pyrolysis heating rate was increased from 15 $^{\circ}\text{C/s}$ to 250 $^{\circ}\text{C/s}$. With the 20 μg samples the overall trend of decrease of char yield with increasing pyrolysis heating rate seemed to hold except for 100 $^{\circ}\text{C/s}$. The discrepancy was caused by clumping of the cellulose particles because they were deposited as a single droplet (5 μL) of the suspension for the 20 μg starting mass. Deposition of the 60 μg mass of cellulose in several small droplets resulted in a more even distribution of particles on the platinum filament and led to more uniform heat transfer to all the particles. Hence, the overall char formation trends validated the hypothesis that the char yield from cellulose decreases with increasing pyrolysis heating rate. Time limitations prevented further studies at higher pyrolysis heating rates, higher pressures and in presence of H₂/CO/CO₂ mixtures.

Table 1.1: Char formation from pyrolysis of cellulose in helium atmosphere.

Sample material	Starting mass* / μg	Pyrolysis rate / $^{\circ}\text{C s}^{-1}$	Total Carbon**/ μg	Residual carbon (char) / μg	Char yield / %
Purified air	-	-	3.5***	-	-
50 μm cellulose	20	15	7.0	3.4	17.2
		100	9.3	5.8	29.0
		250	6.1	2.6	13.0
	60	15	34.1	30.6	51.6
		100	22.9	19.4	32.4
		250	12.3	8.7	14.6
*Estimate based on concentration of cellulose in suspension of 4 g L ⁻¹ (4 $\mu\text{g } \mu\text{L}^{-1}$) **Total carbon as measured by GC-FID analysis (including the air impurity) *** Background caused by CO/CO ₂ impurity in the purified air					

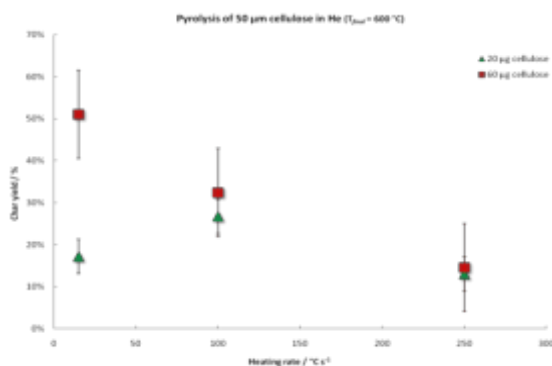


Figure 1.9: Variation of char yields as a function of heating rate for two different starting masses of cellulose.

1.1.3 Conclusions

The microscope visualization experiments that were conducted indicated the values of some of the critical parameters needed for design of a large-scale pyrolysis reactor. It was observed that for cellulose, heating rates on the order of 1,000 $^{\circ}\text{C s}^{-1}$ were sufficient to eliminate the formation of char, regardless of reactive gas atmosphere.

Furthermore, the experiments determined that a heating rate in the 200-500 °C s⁻¹ regimes may be sufficient for an ablative reactor to function, as this is the required rate to liquefy cellulose particles.

A three- step experimental method was developed and a special test apparatus was constructed for systematically quantifying the char formation as a function of the pyrolysis heating rate of cellulose in the pyroprobe. The char formation studies of cellulose pyrolysis in helium atmosphere at different heating rates of 15, 100 and 250 °C s⁻¹ validated the hypothesis that char yield decreases with increasing heating rate of the cellulose particles. The knowledge gained from these char formation studies were useful for selection of optimum process conditions for pyrolysis in the micro-scale batch FHP and the continuous FHP reactors, which are discussed in the subsequent sections.

1.2 Micro-Scale Batch Fast-Hydropyrolysis Reactor

The micro-scale, batch fast-hydropyrolysis reactor is based primarily on the pyroprobe (Pyroprobe 5200, CDS Analytical, Oxford, PA) which utilizes a resistively-heated platinum filament to heat biomass samples at a maximum possible rate of 20,000 °C s⁻¹. A basic schematic of the pyroprobe reactor system is shown in Figure 1.10 and Figure 1.11. The Pt filament which is attached to the pyroprobe housing, was then inserted into the temperature controlled zone which can be pressurized up to 34 bar with He/H₂/CO/CO₂. The downstream portion of the pyroprobe enabled product analysis via a GC/MS. As part of the Year Three research, a fixed-bed catalytic reactor, located downstream of the pyrolysis region between the pyroprobe and valve box, was designed and developed to enable us to perform HDO/WGS reactions after the pyrolysis stage. During the loading phase of the experiment the reactant gas did not flow through the pyroprobe housing (Figure 1.10), which prevented the catalyst from being exposed to air. The 8-port valve was switched during reactor operation and the pyrolysis vapors passed through the fixed-bed reactor and adsorbed on the trap (Figure 1.11). The trap was then heated to 300 °C and the desorbed products were analyzed via a GC/MS.

The purpose of the downstream catalytic reactor was to efficiently upgrade pyrolysis vapors to products suitable as liquid fuels. Prior experiments had shown that the pyrolysis vapors were comprised of compounds which needed to be deoxygenated while at the same time keeping the carbon-carbon bonds intact to maximize the yield and energy content of the liquid products. Two catalytic reactors, a micro-capillary reactor and a fixed-bed reactor, were designed, built and tested to enable the study of different catalysts for HDO of pyrolysis vapor compounds.

A micro-capillary HDO reactor was designed and placed downstream of the micro-scale batch FHP reactor. A detailed description of this reactor is provided in the following experimental description section. The micro-capillary HDO reactor had milligram quantities of a catalyst deposited on the walls of a capillary and the loading of the catalyst could be controlled by varying the length of the capillary coated. However, this reactor could not be operated at high pressure (>6 bar) and the fragile capillary tubes posed several challenges during the design and operation of this reactor. Also, the capillaries could not be exposed to a temperature greater than 350 °C, thereby limiting higher temperature studies over the catalysts. To overcome these limitations, a fixed bed reactor was designed and placed downstream of the pyrolysis zone, as shown in Figure 1.10. The fixed bed reactor could be operated in the temperature range 200 °C – 500 °C and pressure range 1 – 35 bar. As an example of a supported metal catalyst, a 2% Pt/ Al₂O₃ catalyst, from our water-gas-shift (WGS) catalyst inventory, was tested in the fixed bed HDO reactor for catalytic activity on pyrolysis vapor compounds in the presence of hydrogen. Based on the assumption that only H₂ could be utilized in catalytic deoxygenation reactions, CO present in the gas stream generated from the coal gasifier should be shifted to H₂ via WGS. Thus, this WGS catalyst, in addition to being the HDO catalyst, could also shift CO to H₂ using water generated in the FHP reactor. One of the planned tasks in this work was also to determine if CO could be directly involved in deoxygenation during fast-hydropyrolysis of cellulose and subsequent HDO.

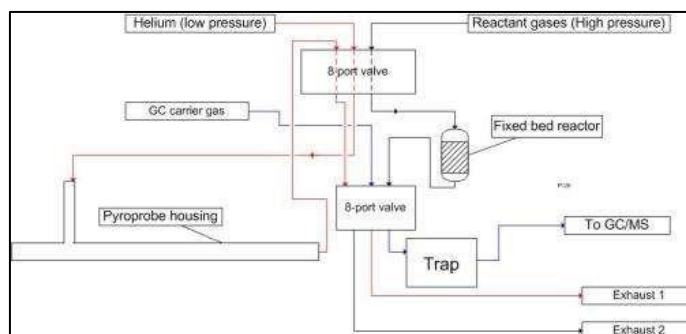


Figure 1.10: Schematic of the micro-scale batch FHP and fixed-bed catalytic reactor arrangement during loading phase.

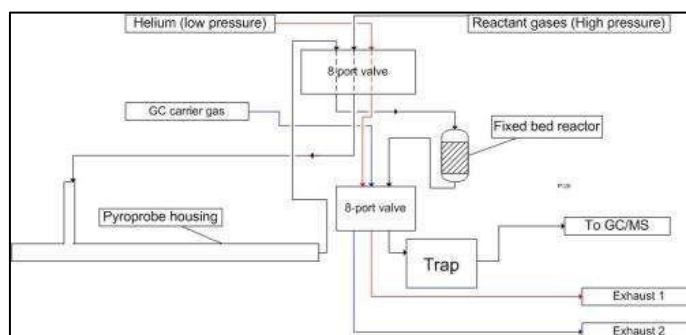


Figure 1.11: Schematic of the micro-scale batch FHP and fixed-bed catalytic reactor arrangement during reactor operation.

1.2.1 Experimental Description

A micro-capillary HDO reactor was designed and prepared in accordance with the procedure mentioned by Bravo et al.^[1,2], who were able to coat cylindrical non-porous channels, having diameters as low as 250 μm with a supported catalyst. The procedure for making the reactor is described in detail and some preliminary results using well-known probe reactions to test the reactor performance are discussed in the following section.

The experimental procedure^[1,2] for coating of a fused silica capillary with the catalyst can be broadly classified into 3 steps –

1. Pre-treatment of the capillary
2. Slurry preparation
3. Gas assisted fluid displacement

The 1st step was performed to pre-treat the inner surface of the capillary to make the surface conducive for adhesion of the deposited catalyst coat. Pretreatment involved exposing the inner surface of the capillary with a Piranha etch solution for 30 min at 100 °C. The Piranha etch solution contained a mixture of sulfuric acid and a solid oxidizer (Nochromix® from Godax Laboratories, Inc) which oxidized impurities present on the inner surface. The inner surface was then rinsed with DI water, followed by ethanol. The capillaries were dried in an oven at a temperature greater than 80 °C prior to deposition of the slurry. Slurries were prepared with composition similar to that given by Bravo et al.^[1,2]. The slurry consisted of a binder, Boehmite (Catapal B from Sasol) which aided in the formation of a viscous slurry and increased the adhesion of the coated layer. The catalyst was milled to a mean particle size of 10 μm in a ball mill before addition to the slurry. The capillary was filled with the slurry and it was forced out using an inert gas under pressure. A thin liquid film was deposited on the surface of the capillary, which was then dried in an oven. A capillary having a uniformly coated inner surface was obtained using this gas-assisted fluid displacement technique (Figure 1.12).



Figure 1.12: Diagram depicting the gas-assisted fluid displacement technique.

To quantify the amount of slurry deposited, the capillary was weighed before and after each of the deposition steps. To maximize the fraction of the slurry coated (ratio of the coated mass of the slurry to the total amount of slurry in the capillary before deposition) in order to increase the amount of catalyst deposited per unit length of the capillary, the effect of the pressure of the inert gas, length of filled capillary, and viscosity of the slurry were studied and optimized. To increase the coating thickness, multiple coats were administered on the previously formed coats. This significantly increased the amount of catalyst deposited per unit length of the capillary. The thickness of the catalyst coat formed was analyzed by using an optical microscope with 100X magnification capability. It was observed that the thickness of the coated layer was uniform along the cross-section of the capillary, however, the thickness varied along the length of the capillary, in agreement with the observations in the literature^[1,3]. Figure 1.13 shows the coated layer, having a thickness of 8.8 μm , on the inner surface of the capillary.

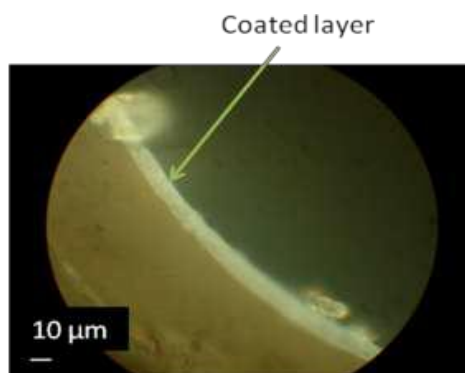


Figure 1.13: Microscope images of the cross-section of the capillary tube showing deposition of coat of catalyst on the inner wall under 100X magnification.

To overcome the shortcomings of low pressure operation and fragility of the micro-capillary reactor, a fixed-bed catalytic reactor was designed which could be placed downstream of the pyroprobe as shown in Figure 1.14. The reactor could be heated to 300 $^{\circ}\text{C}$ by an electric heating jacket which covers the entire valve box. A separate heater for the reactor was added to increase its maximum working temperature to 500 $^{\circ}\text{C}$. This reactor could be operated at pressures up to 34 bar, and hence it gave us the flexibility to test the stability and activity of WGS and HDO catalysts under a wide variety of conditions. For example, WGS and HDO catalysts could be exposed to FHP vapors at 250-350 $^{\circ}\text{C}$ to simulate conditions found in the secondary catalytic upgrading reactor and at 450-500 $^{\circ}\text{C}$ to simulate the harsher conditions found in a FHP reactor.

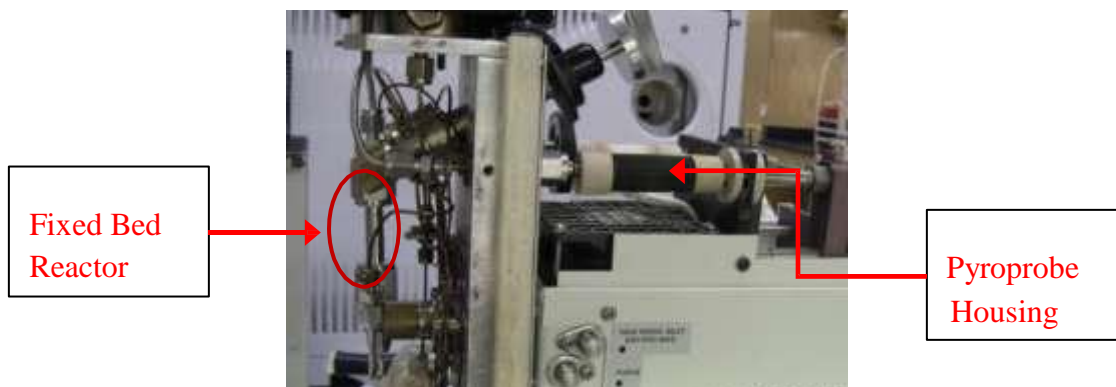


Figure 1.14: Picture showing the fixed-bed reactor installed downstream of the micro-scale, batch FHP reactor (Pyroprobe).

1.2.2 Results and Discussion

To test the feasibility of the coated capillary as a potential reactor, hydrogenation of ethylene over a Pt catalyst was chosen as a probe reaction. A 2 wt% Pt/Al₂O₃ catalyst was prepared using the incipient wetness method and was ball milled to reduce the particle size to that adequate for deposition. A slurry containing this catalyst was prepared and then deposited on the capillary wall. Chemisorption experiments were carried out on the 2% Pt/Al₂O₃ catalyst and the catalyst in the dried slurry to determine possible deactivation of catalyst during the coating procedure. The results, not shown, showed negligible deactivation of the active catalyst. The ethylene hydrogenation probe reaction was carried out in the micro-capillary reactor (530μm ID) under the conditions shown in Table 1.2. Ethylene hydrogenation turnover rates (TOR) and activation energy were obtained and compared to the typical results found in literature^[1,4]. The activation energy and TOR, Figure 1.15 and Table 1.3 respectively, were in good agreement with those reported in the literature^[1,4].

Table 1.2: Conditions for ethylene hydrogenation reaction

Capillary Length / cm	15.9
Deposition in Capillary / g	0.01
Helium Flow Rate / sccm	50
Ethylene Flow Rate / sccm	10
Hydrogen Flow Rate / sccm	10
Pressure / barg	0.35
Temperature Range / K	268 - 298

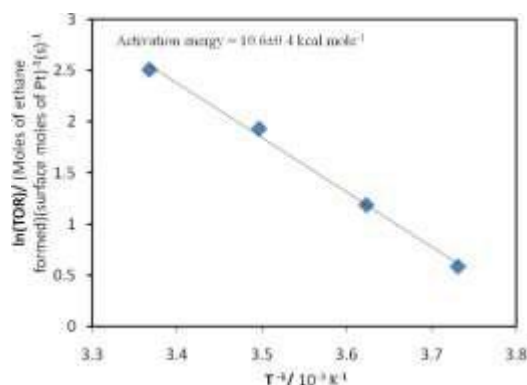


Figure 1.15: Arrhenius plot for ethylene hydrogenation on 2% Pt/Al₂O₃ catalyst.

Table 1.3: Comparison of experimental results with those from literature.

	Experimental	From literature ^{1,4}
TOR / (Moles of ethane formed) (surface moles of Pt) ⁻¹ (s) ⁻¹	12.3	12.4 ⁺
Activation energy / kcal mol ⁻¹	10.6±0.4	9.1±0.5 ⁺

+Results from literature^[1,4] extrapolated to our experimental conditions

After successful testing of a probe reaction, the micro-capillary reactor coated with a 2% Pt/Al₂O₃ catalyst was tested using isopropyl alcohol (IPA) as a model FHP compound to simulate effluent from a hydropyrolysis reactor. The main products observed were acetone and propane/propene. Acetone was a dehydrogenation product, while propene was a product of dehydration of IPA. The relative abundance of these products was found to be a function of the temperature of operation. At 200 °C, acetone was the major product, while propane/propene were minor products. At 300 °C, propane/propene was the major product while acetone was the minor product. The results are summarized in Table 1.4.

Table 1.4: Conversion and selectivity for the reaction of isopropyl alcohol over a 2% Pt/Al₂O₃ catalyst as a function of temperature .

Reaction Environment	Temperature °C	Conversion IPA / %	Selectivity and/or Propene / %	Propane Selectivity Acetone / %
Helium	300	97	78	18
Hydrogen	300	98	74	23
Helium	200	7	8	91
Hydrogen	200	30	4	95

Total gas flow rate = 15 sccm, [IPA] = 4 mol %, 10 mg catalyst

At the higher temperature, IPA was converted to propane/propene over the 2% Pt/Al₂O₃ catalyst with high selectivity. These results indicated pronounced acidic behavior of the alumina support at this temperature, as signified by the dominance of the dehydration pathway. Overall, these results demonstrated the successful operation of the micro-capillary reactor under HDO conditions. But, the limitations of the micro-capillary reactor, including its fragility, inability to be operated at high pressure (> 6 bar), the elaborate procedure needed for its preparation and design considerations during integration with the pyroprobe led us to choose the fixed-bed reactor for continued experiments.

After the design of the fixed-bed catalytic reactor was finalized, fast-hydropyrolysis experiments were carried out in the micro-scale batch FHP reactor and the integrated fixed-bed HDO reactor under high-pressure hydrogen atmosphere. These experiments were aimed at understanding the effect of hydrogen during fast-hydropyrolysis of cellulose and were a pre-requisite to the proposed FHP experiments under simulated H₂/CO/CO₂ atmosphere. Fast-hydropyrolysis experiments were carried out under H₂ partial pressures of 10 bar to 25 bar with cellulose and levoglucosan in the micro-scale batch reactor (pyroprobe). Levoglucosan was the major product of cellulose pyrolysis and was used as a simpler substitute for cellulose to get a better understanding of the effect of HDO catalysts. In this reactor system, the reaction products were analyzed with a GC/MS downstream of the pyroprobe, but due to equipment limitations, products with a molecular weight higher than levoglucosan (C₆H₁₀O₅) could not be detected.

Cellulose particles with a mean diameter of 50 µm were loaded onto the surface of the Pt filament of the pyroprobe, following which it was flushed with inert to remove air from the system. The particles were held in place by electrostatic interactions with the surface in a way that prevents agglomeration or vertical stacking of particles. The Pt filament was then heated to 600 °C at 1,000 °C s⁻¹. When cellulose pyrolysis experiments were carried out in the presence of inert atmosphere alone, levoglucosan was observed as the major product. However, significant deoxygenation, to yield hexane as the major product, was observed during cellulose fast-hydropyrolysis. This effect could be attributed to the presence of H₂ and the platinum filament at 600 °C, which caused the platinum metal to act as a HDO catalyst. For similar pyrolysis experiments with levoglucosan, the sample loading procedure was different from that described for cellulose. Levoglucosan was deposited as a solution in water on the platinum filament and the solvent was allowed to evaporate leaving behind a uniform deposition of levoglucosan. Deoxygenated products observed during fast-hydropyrolysis of levoglucosan were similar to those observed during fast-hydropyrolysis of cellulose. Table 1.5 lists the top six products based on GC peak area for fast-hydropyrolysis of levoglucosan with Pt filament.

Table 1.5: Major products of levoglucosan fast-hydropyrolysis at H₂ partial pressures of 10 bar – 25 bar (ranked on the basis of peak area in GC spectrum) with Pt filament as catalyst in the fast-hydropyrolysis region.

	Compound	Molecular formula
1	n-Hexane	C ₆ H ₁₄
2	n-Pentane	C ₅ H ₁₂
3	3-Hexanone	C ₆ H ₁₂ O
4	n-Butane	C ₄ H ₁₀
5	Methylcyclopentane	C ₆ H ₁₂
6	1-Hexanol	C ₆ H ₁₄ O

Shifting the focus to decoupling the effect of H₂ versus that of platinum during fast-hydropyrolysis of cellulose, the heating source was changed from the Pt filament to a Pt coil. The Pt coil had the advantage that the sample could be placed inside a hollow quartz tube around which the coil was wrapped. Thus, the sample was indirectly heated and the pyrolysis vapors never came in contact with the heated Pt coil in the presence of hydrogen.

High-pressure hydropyrolysis of cellulose was carried out in this modified micro-scale, batch reactor and the products were analyzed using a GC/MS. The product composition did not vary significantly from that of pyrolysis of cellulose under inert conditions. Table 1.6 lists the top six products based on GC peak area for fast-hydropyrolysis of cellulose. Qualitatively, there was no difference in the compounds observed with a GC/MS for fast-hydropyrolysis and fast-pyrolysis of cellulose. From this result, it could be inferred that the deoxygenation effect was predominantly due to hot Pt metal in contact with cellulose and the pyrolysis vapors in a high-pressure hydrogen atmosphere. Although the modification of the reactor ensured that interference due to Pt metal did not disrupt the results of pyrolysis, the indirect heating in the quartz tube reduced the heating rate to approximately 200

C s⁻¹. Fast-hydropyrolysis of cellulose was also carried out in presence of H₂/CO/CO₂ (3.5:1.5:1 mole ratio) mixture in the quartz tube to eliminate the catalytic effect of Pt metal in presence of hydrogen. The major products of pyrolysis were qualitatively similar to the products obtained by fast-hydropyrolysis (pure hydrogen atmosphere) of cellulose (listed in Table 1.6). It was concluded that presence of a H₂/CO/CO₂ mixture did not affect the primary products of cellulose pyrolysis, qualitatively, when analyzed using a GC/MS.

Table 1.6: Major products of cellulose fast-hydropyrolysis at H₂ partial pressures of 10 bar – 25 bar. Cellulose was loaded in quartz tube, which was heated externally by Pt coil (ranked on the basis of peak area in GC spectrum)

	Compound	Molecular formula
1	Levogluconan	C ₆ H ₁₀ O ₅
2	Acetaldehyde, hydroxy-	C ₂ H ₄ O ₂
3	2-Propanone, 1-hydroxy-	C ₃ H ₆ O ₂
4	Furfural	C ₅ H ₄ O ₂
5	2-Cyclopenten-1-one, 2-hydroxy-	C ₅ H ₆ O ₂
6	Levogluconone	C ₆ H ₆ O ₃

Following up on the conclusion that Pt metal was active for hydrodeoxygenation, experiments were conducted for catalytic hydrodeoxygenation (HDO) of pyrolysis vapors in presence of a 2% Pt/Al₂O₃ catalyst. The 2% Pt/Al₂O₃ catalyst was also a good WGS catalyst, based on our earlier studies. The catalyst was loaded in the fixed-bed HDO reactor downstream of the pyrolysis stage. An excess amount of this catalyst was loaded so products after complete conversion could be observed. Levoglucosan was pyrolyzed in presence of hydrogen, in the hollow quartz tube with wrapped Pt coil, and the vapors were passed over the catalyst. The major products observed are summarized in the table below.

Table 1.7: Major products of levoglucosan fast-hydropyrolysis and 2% Pt/Al₂O₃ downstream HDO catalyst at H₂ partial pressures of 10 bar – 25 bar (on basis of peak area in the GC spectrum)

	Compound	Molecular formula
1	Hexane	C ₆ H ₁₄
2	Methyl Cyclopentane	C ₆ H ₁₂
3	Cyclohexane	C ₆ H ₁₂
4	Pentane	C ₅ H ₁₂
5	Ethyl Cyclohexane	C ₈ H ₁₆

These results indicated that the WGS catalyst is active for HDO as well. However, due to the limitations of the equipment it was not possible to estimate the percentage conversion of levoglucosan. It was, however, concluded that, in the presence of the excess amount of HDO catalyst, the pyrolysis vapor products underwent numerous secondary reactions giving completely deoxygenated products.

Coking was observed over the used catalyst which was recovered from the HDO reactor set-up. This led us to investigate the effect of the support (alumina) during the hydrodeoxygenation reaction, but the estimation of the amount of coking on the used catalyst was difficult because micro-gram quantities of reactants were used as feed during a single experiment. Alumina (Al_2O_3) was loaded in the fixed-bed reactor and pyrolysis vapors were passed over it before analysis using the GC/MS. On comparing the signal intensity with that of the calibrated spectrum, it was observed that almost all of the levoglucosan coked over the alumina. Dehydration products like furfural and 2-cyclopentene-1-one were observed, however they were in negligible quantities with respect to the amount of feed. These results indicated that significant dehydration and coking occurs on pure alumina support in a hydrogen atmosphere. In this reactor, coking was accentuated because microgram quantities of levoglucosan were being used as the feed material and the amount of catalyst was in excess with respect to the feed. Significant challenges in quantification of the products of pyrolysis and subsequent HDO reaction limited the understanding of hydrodeoxygenation reactions on the catalyst.

1.2.3 Conclusions

Two different designs for the downstream HDO reactor for the micro-scale batch reactor were tested and a fixed-bed reactor was chosen as the more feasible reactor design. In the absence of a catalyst, the products of cellulose fast-hydropyrolysis were qualitatively similar to the products of cellulose pyrolysis in an inert atmosphere. Similarly, the presence of a $\text{H}_2/\text{CO}/\text{CO}_2$ mixture in the pyrolysis region did not qualitatively affect the primary products of cellulose pyrolysis. In the presence of hydrogen, platinum metal was found to be active for hydrodeoxygenation. A WGS catalyst, 2% Pt/ Al_2O_3 , was successfully tested in the fixed-bed HDO reactor.

1.3 Continuous High-Pressure Fast-Hydropyrolysis Reactor

In Year One and Year Two of the project, the fundamentals of pyrolysis of cellulose particles were studied using an optically-accessible, atmospheric-pressure quartz reactor and the pyroprobe. It was found that rapid heating rates were needed to eliminate the formation of char from cellulose pyrolysis and solid-solid heat transfer to the biomass particles could be enhanced by impinging the particles on a hot conductive surface at high velocities.

Based on the fundamental lessons learned, several prototype, fast-pyrolysis reactors were built and tested to explore different reactor and inlet configurations. A prototype cyclone design was found to be robust and best suited for continuous operation of fast-hydropyrolysis reactor. The cyclone design prevented clogging of the inlet, which had hampered the operation of the former reactors. High heat transfer rates to the biomass, low char yield and low residence time were crucial in adopting this design for the continuous FHP reactor.

In Year Three, the results from the prototype cyclone reactor and fundamental insights gained from the micro-scale batch reactor were used to design and build the new continuous, high-pressure, cyclone-type, FHP reactor safe for use with hazardous gases like H_2 and CO. A downstream high-pressure, fixed-bed hydrodeoxygenation (HDO) reactor was also designed and built. After initial shakedown tests of this combined reactor system with high-pressure inert atmosphere, high-pressure fast-hydropyrolysis experiments were started. Experiments at high H_2 partial pressures were performed to understand the effect of hydrogen on the liquid product and the product distribution. Then, fast-hydropyrolysis experiments were done with downstream HDO/WGS catalysts that were identified from the micro-scale batch experiments. The experiments were systematically designed so that the effect of $\text{H}_2/\text{CO}/\text{CO}_2$ mixtures, resulting from the fast-hydropyrolysis, on the HDO/WGS catalysts could be understood. The effect of the catalyst support on the liquid products and the product distribution was also investigated. In all the experiments, cellulose, of mean particle size of 50 μm , was used as a model biomass feedstock to simplify the products and gain a more fundamental understanding of the different effects. In the following sections, the reactor setup is discussed and the important results from the different experiments performed are highlighted.

1.3.1 Experimental Description

Figure 1.16 shows a picture of the cyclone-type fast-hydropyrolysis reactor along with the fixed-bed catalytic HDO/WGS reactor. Figure 1.17 shows the process flow diagram for the reactor system. The new reactor system was designed for use at high temperature (up to 650 °C for FHP and up to 500 °C for HDO/WGS reactor) and high-pressure (up to 100 bar). Model biomass feed stock, such as cellulose, is fed to the system using a high-pressure biomass screw feeder capable of feeding at the rates of 0.1-10 g min⁻¹. The cellulose is entrained with hydrogen and inert gases and pyrolyzed in the cyclone FHP reactor. The char is collected below the reactor in the char collector, and the vapors exit from the top of the FHP reactor. The vapors then move through a transfer section to the fixed-bed catalytic HDO/WGS reactor where they get upgraded. The upgraded vapor products are condensed with a concentric tube heat exchanger and collected in two stages. The first stage is comprised of a coalescing filter and the second stage is comprised of a cold finger trap cooled with a mixture of ice and water, and both these fractions are mixed together before analysis of the liquid product. After liquid product separation and collection, the remaining permanent gases are analyzed using an on-stream gas chromatograph (GC). The reactor system is monitored and controlled by a custom built Labview system. The reactor system is heated using a combination of custom-made heating jackets and heating tapes, which are again controlled by Labview.

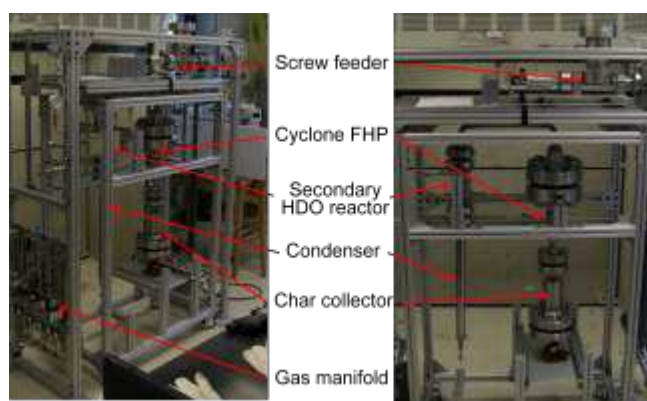


Figure 1.16: Pictures showing the high-pressure, cyclone-type, fast-hydropyrolysis reactor.

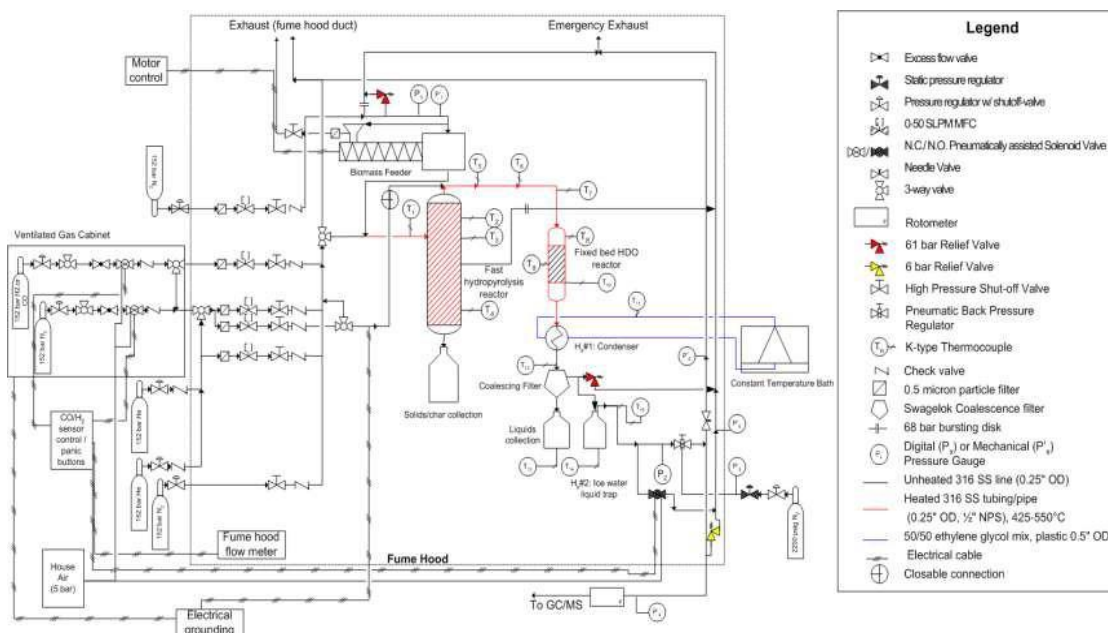


Figure 1.17: Process flow diagram of the high-pressure FHP and HDO/WGS reactor system.

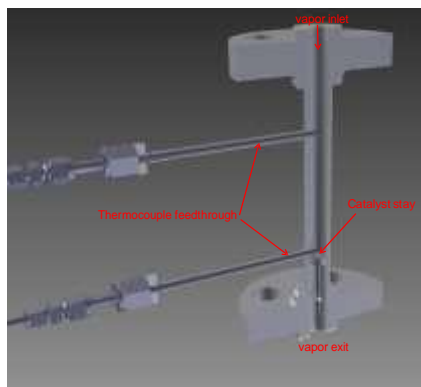


Figure 1.18: Partial half-section view of the fixed-bed, catalytic reactor designed, built and used for HDO/WGS studies

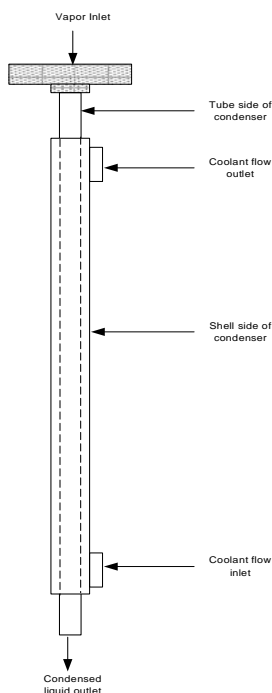


Figure 1.19: Schematic of the concentric tube heat exchanger designed, constructed and successfully used for rapid quenching of vapor stream.

Figure 1.18 shows a half section view of the fixed-bed, catalytic reactor with the catalyst cartridge stay which supported the catalyst particles or pellets in the reactor. The thermocouple feedthroughs are used to measure temperatures of inlet gas stream and the catalyst bed. The reactor has been designed for high temperature (up to 500 °C) and high pressure (up to 100 bar) operation.

Figure 1.19 shows a schematic of the high performance quenching system based on a concentric tube heat exchanger, which was developed for the continuous flow reactor. This quenching system had to be specially designed and constructed for use in high-pressure applications and to aid in the rapid quenching of the hydropyrolysis vapor stream which is dilute because of the high carrier gas flow rates required in the reactor to control vapor residence times at high-pressure operation. This quenching system was operated successfully with a

mixture of ethylene-glycol and water as the coolant on the shell-side of the heat exchanger in all the experiments that are reported in the subsequent sections.

1.3.2 Results and Discussion

After construction of the continuous FHP reactor, initial shakedown experiments in high-pressure inert atmosphere were started. Table 1.8 shows the experimental summaries for two shakedown experiments. In Run 2, the char yield was less, indicating that more cellulose was converted to liquids and gases. This result is likely due to higher average reactor temperatures which resulted in incrementally higher cellulose heating rates. Further, the decrease in solids concentration in the inert carrier gas in Run 2 is likely to have reduced the clumping of cellulose particles, thus improving the heat transfer to them. These experiments are further proof for the hypothesis from the char formation studies that the char yield decreases with increasing heating rate to the cellulose particles. The error in the overall mass balance was attributed mainly to inaccurate measurement of the gas yield due to sampling rate limitations inherent in the gas chromatograph which prevented the gas production from being accurately integrated. Another smaller source of error was the estimation of system holdup by rinsing the reactor system with a solvent and evaporating it to calculate the liquids held up in the reactor.

The initial shakedown experiments were successful and showed that the new reactor system was capable of pyrolyzing cellulose at high pressure with an acceptable liquid yield. These experiments were also used to refine standard operating procedures and safety features of the reactor for use with high-pressure H₂ and CO. Based on these experiments, the downtube inside the cyclone FHP reactor was removed to improve the time-on-stream. After a final safety review, fast-hydrolysis experiments of cellulose were started. Initially, there were some challenges in heating the reactor at high hydrogen flow rates, but the heating system was successfully modified by combining a high temperature ceramic heater and flexible laboratory heating tapes which were able to input more heat to the reactor. Table 9 shows the experimental summary for one of the fast-hydrolysis experiments. The product yields in the fast-hydrolysis experiments were similar to the corresponding experiments in an inert atmosphere (fast-pyrolysis). On analysis of the liquid products by direct liquid injection into a GC/MS, the top compounds (shown in Table 1.10) present in the liquid products from fast-pyrolysis and fast-hydrolysis of cellulose were similar on a qualitative basis. This suggested that in the absence of a catalyst, the hydrogen atmosphere did not change the liquid product composition (qualitatively) from pyrolysis of cellulose, which is consistent with the results from the micro-scale batch reactor.

Table 1.8: Experimental summary for initial shakedown fast-pyrolysis experiments with cellulose.

	Run 1	Run 2
Feedstock	50 μ m cellulose	50 μ m cellulose
Feed rate / g min ⁻¹	1.0	0.7
Run time / min	60	89
Total mass fed / g	60.0	59.5
Inert gas flow rate / (std) L min ⁻¹	39.3	39.3
Pressure / bar	49.7	49.5
Average pyrolysis temperature / °C	460 \pm 10	500 \pm 21
Feedstock conversion	~100%	~100%
Liquid yield / wt %	68.0	69.1
Char yield / wt %	13.2	10.9
Gas yield / wt %	8.4	8.6

Table 1.9: Summary of the overall mass balance for a cellulose fast-hydrolysis experiment at a H₂ partial pressure of 25 bar.

Mass Flow Rate / g min ⁻¹	0.9	Total Solids Fed / g	41
Total Pressure / bar	27	Liquids / wt %	67
Hydrogen Flow Rate / L min ⁻¹ *	35	Solids (Char) / wt %	8

Nitrogen Flow Rate / L min ⁻¹ *	3	Gases / wt %	6
		CO / ppm in gas phase	411
Hydrogen Partial Pressure / bar	25	CO ₂ / ppm in gas phase	386
Reactor Inner Wall Temperature / °C	477	CH ₄ / ppm in gas phase	64

* Calculated at standard conditions (STP)

Table 1.10: Comparison of top compounds, based on peak area, in the liquid products from the different experiments on analysis with a GC/MS.

Cellulose Fast-Pyrolysis	Cellulose Fast-Hydropyrolysis
Levogluconan	Levogluconan
Furfural	Hydroxymethylfurfural
Hydroxymethylfurfural	Furfural
2-Propanone, 1-hydroxy-	2-Propanone, 1-hydroxy-
1,4:3,6-Dianhydro- α -d-glucopyranose	2-Cyclopenten-1-one, 2-hydroxy-
2-Cyclopenten-1-one, 2-hydroxy-	1,4:3,6-Dianhydro- α -d-glucopyranose

After investigating the effect of hydrogen on pyrolysis alone, experiments of continuous cellulose fast-hydropyrolysis in a high-pressure hydrogen atmosphere with a WGS catalyst, 2% Pt/Al₂O₃, in the downstream fixed-bed catalytic HDO reactor were completed. Table 1.11 shows the experimental summary for one of the experiments. As compared to cellulose fast-hydropyrolysis experiments without a HDO catalyst, the gas phase production of carbon monoxide was much higher in presence of the Pt-based HDO catalyst. This suggested that this catalyst favored the decarbonylation reaction pathway at these reaction conditions. The liquid product was visibly less viscous compared to that from the fast-hydropyrolysis experiments without the HDO catalyst, which indicated higher water content due to some degree of catalytic hydrodeoxygenation. On analysis of the liquid product by direct liquid injection into a GC/MS, the top compounds (shown in Table 1.13) were partially deoxygenated compounds like cyclopentanone, 2-butanone etc. This suggested that the WGS catalyst 2% Pt/Al₂O₃ was active for HDO as well.

Table 1.11: Summary of the overall mass balance for an experiment of cellulose fast-hydropyrolysis and 2% Pt/Alumina as the downstream HDO catalyst.

Catalyst	2% Pt on Alumina	Feed Mass Flow Rate / g min ⁻¹	0.8
Amount of Catalyst / g	5	Total Solids Fed / g	49
Total Pressure / bar	27	Liquids / wt %	40
Hydrogen Partial Pressure / bar	9.2	Gases / wt %	32
Hydrogen Flow Rate / L min ⁻¹ *	9.5	CO / ppm in gas phase	5667
Helium Flow Rate / L min ⁻¹ *	15.7	CO ₂ / ppm in gas phase	542
Nitrogen Flow Rate / L min ⁻¹ *	3.0	CH ₄ / ppm in gas phase	741
Reactor Inner Wall Temperature / °C	548	Ethylene / ppm in gas phase	298
Catalyst Bed Temperature / °C	372	Solids (char) / wt %	6

*Calculated at standard conditions (STP)

After the continuous high-pressure fast-hydropyrolysis experiments with the 2% Pt/Al₂O₃ catalyst in the downstream fixed-bed catalytic HDO reactor, some coking was observed over the used catalyst even in these continuous grams-scale experiments, similar to the batch micro-scale experiments. So, it was decided to further investigate the effect of alumina (Al₂O₃) by carrying out experiments with 50 μ m cellulose as a model feedstock and pure alumina in the downstream fixed-bed catalytic HDO reactor. Table 1.12 shows the experimental summary for one of the experiments. The product yields of liquids and gases from this experiment were similar to yields from fast-hydropyrolysis experiments without HDO catalyst. The gas phase product composition of CO, CO₂ and CH₄ in this experiment was also comparable to that for the fast-hydropyrolysis experiments without HDO catalyst. Similar to the micro-scale batch experiments, significant coking was noticed on the pure alumina. In the continuous grams-

scale experiments, however, significant amounts of dehydrated products were observed in the liquid phase. On analysis with direct liquid injection into a GC/MS, a significant percentage of dehydration products (shown in Table 1.13) like furfural, levoglucosenone etc were observed. A lower viscosity of the liquid product as compared to fast-hydropyrolysis experiment without HDO catalyst was noticed, which could signify higher water content. Therefore, in this continuous grams-scale reactor coking was observed on the pure alumina support in high-pressure hydrogen environment, but a significant increase in the dehydrated products was noted which signified HDO activity of the alumina.

Table 1.12: Summary of the overall mass balance for one of the experiments of cellulose fast-hydropyrolysis and pure alumina as the downstream HDO catalyst.

Catalyst	Pure Alumina	Feed Mass Flow Rate / g min ⁻¹	0.7
Amount of Catalyst / g	5	Total Solids Fed / g	45
Total Pressure / bar	27	Liquids / wt %	64
Hydrogen Partial Pressure / bar	9.2	Gases / wt %	13
Hydrogen Flow Rate / L min ⁻¹ *	9.5	CO / ppm in gas phase	1577
Helium Flow Rate / L min ⁻¹ *	15.7	CO ₂ / ppm in gas phase	694
Nitrogen Flow Rate / L min ⁻¹ *	3.0	CH ₄ / ppm in gas phase	167
Reactor Inner Wall Temperature / °C	549	Ethylene / ppm in gas phase	35
Catalyst Bed Temperature / °C	376	Solids (char) / wt %	13

*Calculated at standard conditions (STP)

Table 1.13: Comparison of top compounds, based on peak area, in the liquid products from the different experiment on analysis with a GC/MS.

Cellulose Fast-Hydropyrolysis and HDO on 2% Pt/Al ₂ O ₃	Cellulose Fast-Hydropyrolysis and HDO on pure Al ₂ O ₃
Levoglucosan	Furfural
Cyclopentanone	Levoglucosenone
Methanol	5-Methyl furfural
Cyclopentanone, 2-methyl	2-Cyclopenten-1-one, 2-hydroxy-
2-Butanone	Levoglucosan
2-Propanone, 1-hydroxy-	2-Cyclopenten-1-one, 2-hydroxy-3-methyl-

1.3.3 Conclusions

A novel continuous high-pressure fast-hydropyrolysis reactor and a downstream fixed-bed catalytic reactor have been designed, built and successfully tested in high-pressure hydrogen atmosphere. From cellulose fast-pyrolysis and fast-hydropyrolysis experiments it was seen that in the absence of catalyst, hydrogen did not change the liquid product compositions on a qualitative basis. So, a HDO catalyst was the key for deoxygenation of hydropyrolysis vapors to produce a liquid product suitable of upgrading or directly usable as jet fuel. A WGS catalyst, 2% Pt/Al₂O₃, was found to be active for HDO in the presence of H₂/CO/CO₂ mixtures resulting from fast-hydropyrolysis of cellulose. Comparison of the product distributions for HDO over 2%Pt/Al₂O₃ versus Al₂O₃ suggests that optimal catalysts will need a balance of dehydration (acid) and hydrogenation (metal) sites.

1.4 References

- [1.1] P. J. Dauenhauer, J. L. Colby, C. M. Balonek, W. J. Suszynski, L. D. Schmidt, *Green Chemistry* 11 (2009) 1555-1561.

[1.2] J. Bravo, A. Karim, T. Conant, G. P. Lopez, A. Datye, *Chemical Engineering Journal*, 101 (2004), 113–121.

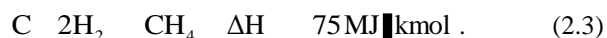
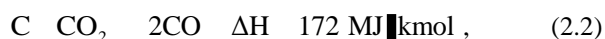
[1.3] A. Polynkin, J. F. T. Pittman, J. Sienz, *Chemical Engineering Science*, 59 (2004), 2969 – 2982.

[1.4] J. C. Schlatter, M. Boudart, *Journal of Catalysis*, 24 (1972), 482–492.

2.0 Investigation of Coal and Biomass Gasification using *In-situ* Diagnostics

2.1 Introduction

Coal/biomass gasification can be considered as a three step process: (1) volatile, low molecular weight hydrocarbons are released as the feedstock particles are heated; (2) volatiles combust in the presence of an oxidant; and (3) the remaining char is gasified via heterogeneous reactions. For char consisting mostly of carbon, the following reactions are active^[2.1].



These heterogeneous char gasification reactions proceed at a slower rate than the devolatilization or the homogeneous gas-phase reactions. Therefore, characterization of the kinetics of the heterogeneous char gasification reactions is vital for the design of coal to liquid fuel systems, and is an important goal of this project.

Most fundamental studies on gasification kinetics that are reported in the literature have been conducted in small-scale batch-reactor or bed-reactor configurations^[2.2, 2.3]. However, the most common gasifier-type used within the industry is the entrained-flow type. The choice for using entrained-flow reactors is based upon the advantages of the entrained-flow reactor arrangement that have been summarized by Hotchkiss^[2.4]. Some of the major advantages include high-throughput of fuel, large conversion efficiencies and the ability to inject dry and wet feed fuels^[2.5, 2.6]. Therefore, there is considerable controversy within the field on the use of the fundamental kinetic rates derived from small-scale batch-type of bed-type reactors for the development of entrained-flow reactor systems.

Furthermore, most fundamental studies on coal/biomass gasification separately study the devolatilization and gasification processes. In commercial designs, the two processes are not conducted in separate systems but occur simultaneously and are dependent on the reactor heating rates and pressures. Therefore, the use of devolatilization kinetics and gasification kinetics separately in devising large-scale industrial gasifiers may not be optimum. It is necessary to study the kinetics and the evolution of the major species of interest by studying the devolatilization and gasification reactions simultaneously. In addition, a large number of studies that have been reviewed typically depend on indirect measurements such as the rate of solid mass decrease or final-equilibrium product analyses to derive the kinetic rates. These measurement techniques are preferred because tracking the detailed gasification kinetics is difficult under the high temperature and high pressure conditions inherent to most gasifiers. The indirect analysis techniques neglect the details of the major gaseous species, such as CO, CO₂, CH₄, and H₂, which are formed (or consumed) during the gasification process. Optimization of the major species chemical kinetic rates will help development of efficient gasifier arrangements.

A novel approach for in situ measurements of gas composition and temperature was used with the Tunable Diode Laser Absorption Spectroscopy (TDLAS). One of the primary objectives of the gasification experiments was to determine evolution of concentration of the CO and H₂O species via real time measurements using TDLAS. Two reactor configurations were developed for this study: (i) continuous-flow-system (CFS) and (ii) fixed-bed-system (FBS). The continuous-flow-system was built to emulate the large-scale gasifiers and was provided with an optical access at various axial locations for in-situ measurements. The fixed-bed-system was developed for understanding the gasification behavior of different types of feedstock in presence of a multi-component gasification environment.

at different operating conditions. Both the systems were equipped with pressure and temperature measurement devices located at suitable positions. A secondary objective was to determine the impact of the continuous flow and fixed bed arrangements on the gasification kinetics. Year 1 of this work was used to perform an extensive review of gasification literature. The team visited various gasification plants in the US to determine the relevant operating parameters for system design. A computation model was created based on chemical kinetic data available in the literature^[2.10]. The results of the computational study were used to fix the operating parameters for the continuous-flow gasifier arrangement described in this report.

Year 2 of this work was used to design and assemble the continuous-flow gasifier arrangement. The gasifier arrangement consisted of the optically-accessible reactor vessel, a steam generator, a powder feeder, a heater system, gas sampling and exhaust system, and instrumentation. The high-pressure and high-temperature conditions of this study led to significant challenges during system integration. Results demonstrating the system performance are presented in this report. In addition, preliminary experiments using laser-absorption-spectroscopy were performed.

Year 3 of this work was directed towards fixed bed studies to isolate the experimental challenges associated with the particle and steam feeder systems and their integration. A fixed-bed reactor system capable of yielding fundamental gasification and pyrolysis kinetics data was developed. The fixed-bed system incorporated an optically-accessible section for diode-laser-absorption-spectroscopy and the capability for operation at high-pressures. Repeatable gasification experiments have been conducted using CO₂ as the gasification medium and a low-ash pinewood biomass as the fuel. Laser-absorption-spectroscopy has been used to track the concentration of CO species that was generated through the gasification reaction. Results from these experiments are reported.

The next section describes the design and development of the reactor systems. The theory behind the TDLAS technique is elaborated on in a later section and the development of optical access is described. Results from the continuous flow and the fixed bed experiments are presented.

The main objectives of the experimental investigation of gasification include:

1. Study the gasification behavior of different feedstock (bituminous coal, pine wood saw dust) in presence of single and multi-component gas mixture (CO₂, H₂O, H₂O+H₂)
 - a. Assess the effect of external H₂ addition on CO₂ emissions
 - b. Assess the effect of external H₂ addition on steam gasification
2. In-situ measurement of H₂O and CO using TDLAS technique

2.2 Continuous-Flow Experimental Arrangement

The continuous flow reactor has been described in relevant conferences^[2.7-2.10]. The 2 m long gasifier with an inner diameter of 7.62 cm operates at temperatures up to 1100 K and pressures up to 10 bar^[2.7,2.8]. In this apparatus, superheated steam is used as the oxidizer for heating and for gasification of carbonaceous material. Steam gasification offers the advantage of reduced CO₂ emissions by avoiding conventional auto-thermal operation^[2.11]. Superheated steam is produced using a novel H₂-O₂ chemical steam generator^{2.9} and is injected into the top of the gasifier. Simultaneous injection of pulverized coal or biomass is enabled through a high-pressure auger-driven feeder which is also located at the top of the gasifier. The reactant flow rates can be controlled to study the effects of equivalence ratio and particle loading. Excess hydrogen is added to the steam flow to investigate its effects on the gas product composition^[2.12, 2.13]. Solid particles, dispersed in the steam flow, travel down the length of the gasifier, which is heated externally to maintain nearly isothermal conditions. At the exit of the gasifier, effluent gases and solid byproducts are separated and collected for post experiment analysis. The effluent gas compositions are analyzed using gas chromatography (GC) and an FTIR based multi-gas analyzer to quantify CO₂, CO, CH₄, H₂, O₂, N₂, NO₂, NO, and SO₂ in the product stream. The solid byproducts are analyzed using scanning electron microscopy (SEM) and their structure is compared to un-reacted particles to better understand the differences in size, shape, porosity and morphology. In addition to these measurements, the gasifier is equipped with an optically-accessible window section that can be placed at multiple axial locations. This permits TDLAS measurements of

temperature and water vapor mole fractions at select axial locations. It is expected that the water vapor concentrations will decrease along the length of the gasifier as the reaction progresses. Therefore, these measurements will provide quantification of the global reaction progress. One of the major challenges in gasifier design is the lack of experimental data from arrangements that are scalable with the industrial apparatus. Availability of detailed real-time experimental data that can be applied to the design of large-scale industrial gasifiers is of current need.

The operating conditions for the gasifier system were determined from the literature ^[2.11, 2.12]. The gasifier was designed to operate at a maximum temperature of 1200 K and a pressure of 1.3 MPa. The reaction temperature was maintained using electrical heating that is rated for 15 kW. This value was chosen based on commercially available electrical heaters. The steam flow rates and coal flow rates were determined from the work by Sane et al ^[2.12]. A summary of the operating conditions is presented in Table 2.1.

Table 2.1: Operating parameters for the continuous-flow gasifier arrangement.

Operating Parameter	Value
Pressure	1 – 1.3 MPa
Temperature	1100 – 1400 K
Coal flow rate	0.4 to 0.6 g/s
Steam flow rate	1.2 to 1.8 g/s
External Heating Power	15 kW

The gasification arrangement consisted of six subsystems – an optically accessible entrained-flow gasification reactor, a hydrogen-oxygen steam generator producing high pressure and temperature steam, a high-pressure coal/biomass-feeder, an external heater system, an inline gas-sample collector, and a multi-channel data acquisition and remote-control system. The complete system is represented by the plumbing and instrumentation diagram in Figure 2.1.

A schematic outlining the operation of the gasifier arrangement is shown in Figure 2.2. Steam and pulverized coal/biomass were injected into the optically-accessible reactor as simultaneous top-down flows. Energy for the endothermic gasification reactions (Eq. (2.1) and (2.2)) was provided by the high temperature steam and sustained by additional electrical heaters along the length of the reactor. Laser diagnostics in the form of tunable-diode-laser-absorption-spectroscopy was utilized to probe major gas-phase species and temperatures at multiple axial locations along the gasification reactor. Partially gasified coal/biomass particles were contained in an ash collection system at the reactor base. Gas products including synthesis gas exited the system via the exhaust line. A control valve on the exhaust line maintained a constant pressure within the gasification reactor. Finally, a multi-sample gas collection system was installed at the end of the exhaust tube. The collected gas samples were analyzed using gas chromatography for species concentrations and were compared with the tunable diode laser-based absorption spectroscopy data.

Pressure transducers and thermocouples connecting to a multichannel data acquisition system continuously monitored the conditions of all systems and flows. The multi-channel data-acquisition and control system enabled remote operation from an adjacent control room. Figure 2.3 displays the gasifier reactor, the hydrogen-oxygen steam generator and the coal/biomass feeder in a test-ready arrangement, and Figure 2.4 displays the control room containing the data acquisition and control systems. In the sections that follow, further details are given for each of the sub-systems.

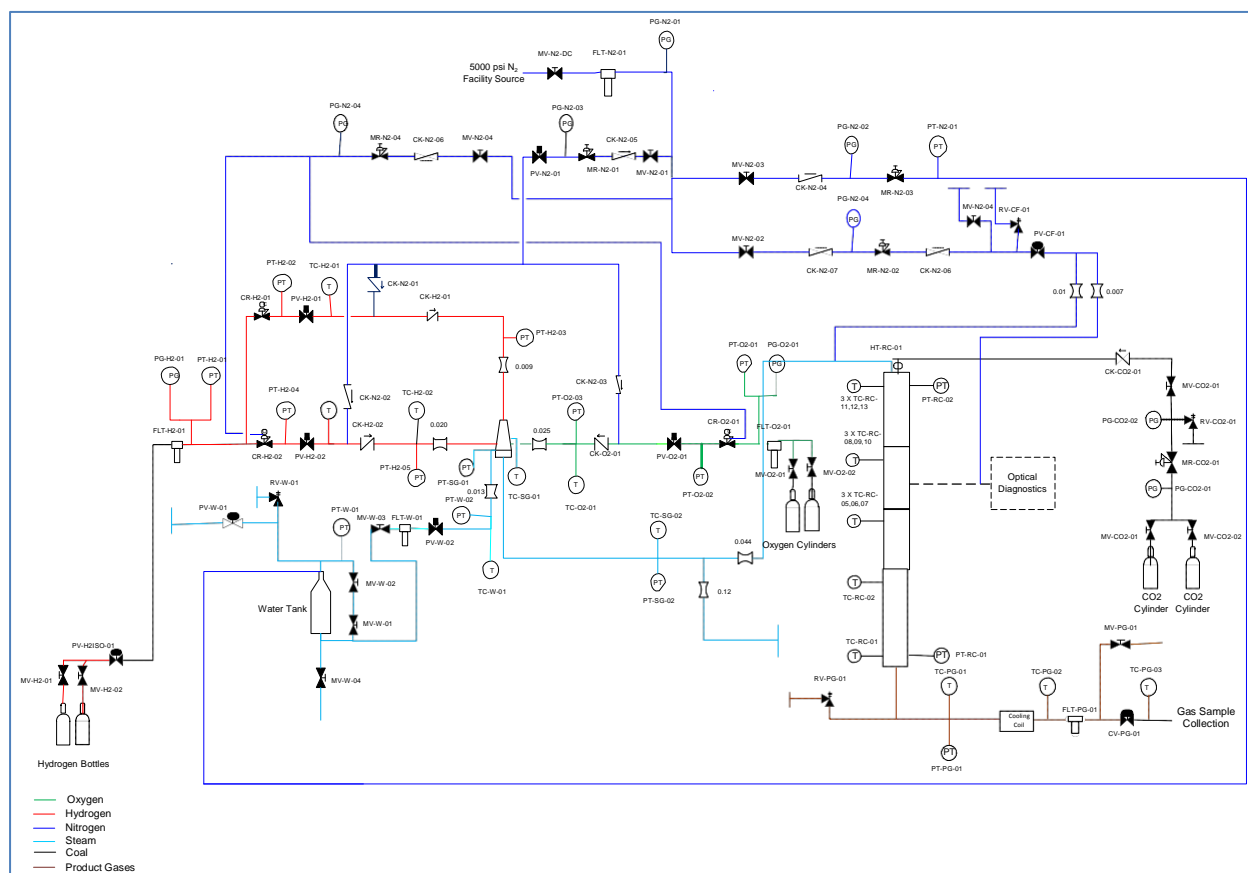


Figure 2.1: Plumbing and instrumentation diagram for the continuous-flow reactor arrangement.

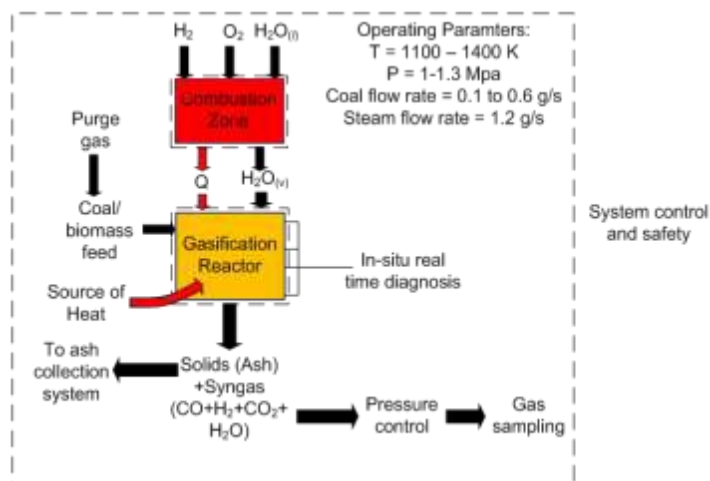


Figure 2.2: Schematic of the continuous-flow arrangement.



Figure 2.3: Gasifier reactor, hydrogen-oxygen steam generator and coal/biomass feeder in the test cell.



Figure 2.4: Nitrogen purge control panel, data acquisition and remote monitoring systems in control room.

2.2.1 Gasification Reactor Sub-assembly

The gasification reactor is constructed of stainless-steel 316 and has a height of 2.5 meters. The reactor consists of four interchangeable spool pieces each with an inner-diameter of 7.2 cm and wall-thickness of 2.54 cm. Figure 2.5 displays the physical reactor and its schematic. The reactor expands by approximately 6 cm when heated to 1100 K.

During operation, high-pressure and temperature steam and coal/biomass are injected in the top-most spool piece. Mixing between the coal/biomass and steam is enhanced by a swirl-flow generated by tangential injection of the steam into the reactor. Radiant heaters surround the spool pieces to provide 15kW of heat and sustain the endothermic gasification reactions. The large flanged-section at the bottom of the gasification reactor contains a dome for collection of ash and partially gasified particles. These particles are subsequently characterized using scanning electron microscopy (SEM). The system contains two pressure transducers and 20 thermocouples for temperature measurements.

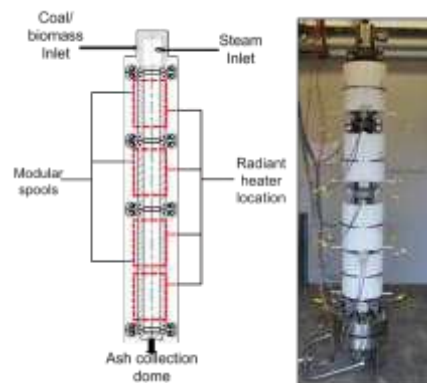


Figure 2.5: Gasification reactor schematic (left) and actual reactor (right).

Heating tests were performed to check the operability of the heater system and detect any high-temperature related defects with the gasifier. Figure 2.6 displays the temperature measurements at four axial locations along the length of the reactor vessel. An approximately constant temperature (1130+/-20K or isothermal within 2%) is measured for the upper two-thirds of the reactor enabling fundamental gasification experiments.

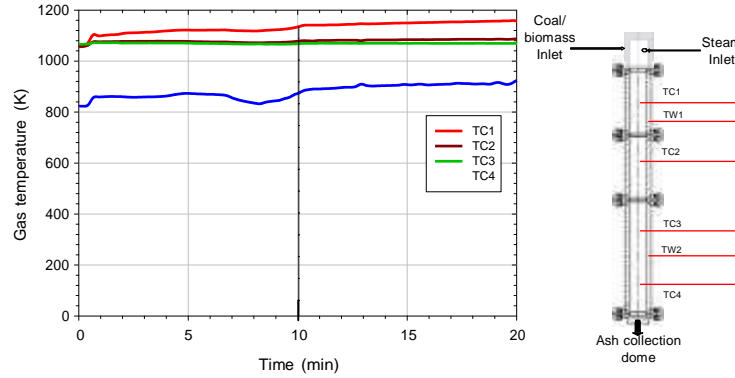


Figure 2.6: Isothermal operation of the heater is verified by heating experiments.

2.2.2 Diode laser absorption spectroscopy and application to a environment

Tunable-diode-laser-absorption-spectroscopy (TDLAS) is used for *in-situ* diagnostics of the gas phase temperature and species concentrations at multiple locations along the length of the entrained flow reactor. Line-of-sight optical access for the TDLAS measurements is achieved using the optically accessible window section shown in Figure 2.12. Fused silica windows are assembled onto a spool-piece, which can be interchanged with those shown in Figure 2.5. This allows for TDLAS measurements and flow characterization at four axial locations along the reactor, providing information on the evolution of the major gas-phase species and reaction temperatures during the gasification progress.

2.2.2.1 Theory of Laser Absorption Spectroscopy

In direct absorption spectroscopy (DAS) measurements, a collimated laser beam with an intensity of I_i is shone through the sample gas, and the transmitted laser intensity I_t is measured with a detector. When the laser frequency ν [cm^{-1}] is resonant with the frequency of a transition for the absorbing species in the gas, the laser energy will be absorbed. The attenuation of the laser intensity along a differential path length of dx can be predicted as follows by the Einstein theory of radiation,

$$\frac{dI}{I} = -P X_{abs} S_i(T(x)) dx$$

Where P is the pressure, X_{abs} mole fraction of the absorbing species, S_i is the line strength the line strength of the transition i , T is the temperature and d is the line shape function such that $\int d = 1$. The line strength is a function of temperature.

When the gas medium is uniform (i.e. uniform temperature and species distribution), the distribution reduces to the Beer-Lambert's law,

$$\frac{I_t}{I_0} = \exp(-PX_{abs}S_i(T)L)$$

where T is the fractional transmission, I_0 is the incident intensity of laser and L is the total path length.

The spectral absorbance is given by,

$$PX_{abs}S_i(T)L$$

And the total absorbance is calculated by integration over all wavelengths and is given by,

$$A = \int PX_{abs}S_i(T)L d\lambda$$

The line shape function $S_i(T)$ of a particular absorption transition, which represents the relative variation in the spectral absorbance with frequency, is determined by the physical mechanisms that perturb the energy levels of the transition or the way in which the absorbing molecules interact with the laser beam. The line shape function is affected by the Doppler broadening and collisional broadening. Doppler broadening is due to the random thermal motion of the absorbing molecules. As the molecules are moving towards or against the laser propagation, the frequency at which the radiation is absorbed will change. Since the random thermal motion of the molecules is governed by a Gaussian function, the Doppler broadening D can be expressed as,

$$D = \frac{2}{D} \sqrt{\ln 2} \exp\left(-\frac{4 \ln 2}{D^2} \left(\frac{c}{\lambda} - \frac{c}{\lambda_0}\right)^2\right)$$

The Doppler full-width at half maximum (FWHM) D is given by,

$$D = 0.716 \sqrt{\frac{8k_B T \ln 2}{mc^2}}$$

Pressure broadening and shifting of spectral lines are caused by the perturbation of the energy levels due to molecular collisions. The collisions are assumed to be binary and the duration of collisions is negligibly short. In the impact theory, the pressure-broadened line shape takes a Lorentzian profile, which is symmetric about the pressure-shifted line center $\lambda_0 + \Delta\lambda_s$

$$L = \frac{1}{\pi} \frac{\frac{c}{\lambda_0 + \Delta\lambda_s}}{\left(\frac{c}{\lambda} - \frac{c}{\lambda_0 + \Delta\lambda_s}\right)^2 + \left(\frac{c}{2\Delta\lambda_s}\right)^2}$$

Doppler broadening dominates at low pressure whereas collisional broadening dominates at high pressure. The actual line shape function is calculated by convoluting the Gaussian and Lorentzian shape functions that result in a Voigt profile,

$$V(a_V, w) = \frac{1}{\sqrt{\pi}} \int_{-\infty}^{\infty} \exp\left(-\frac{u^2}{2}\right) \exp\left(-\frac{(u - a_V)^2}{w^2}\right) du$$

The normalized Voigt function $V(a_V, w)$ is characterized by two non-dimensional parameters that characterize the relative effects of Doppler broadening and collisional broadening, and the distance from the pressure shifted line center:

$$a_V = \frac{\sqrt{\ln 2}}{D} \frac{c}{\lambda_0} \Delta \lambda_D$$

$$w = \frac{2\sqrt{\ln 2}}{D} \frac{c}{\lambda_0} \Delta \lambda_C$$

The Voigt profile, which has been the basis for most quantitative absorption spectroscopy does not have a simple analytical form. It is either approximated by complex functions or most often calculated numerically^[2,14,2,15]. For very small or very large values of a_V , the Voigt profile reduces to the Doppler or Lorentzian lineshape respectively.

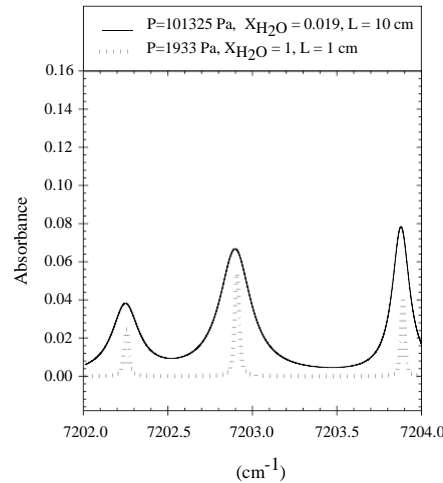


Figure 2.7: Effect of pressure broadening and shifting (T=296 K)

As an example, the integrated absorbance A , the pressure-induced frequency shift $\Delta \lambda_s$, as well as the overall linewidth which includes contributions from both the Doppler FWHM $\Delta \lambda_D$ and collisional FWHM $\Delta \lambda_C$ are illustrated in Figure 2.7 on the line shapes of H_2O transitions at a water vapor mole fraction of 0.019 with/without a buffer gas of dry air.

2.2.2.2 Design of the proposed TDLAS system

Tunable Diode Laser Absorption Spectroscopy (TDLAS) offers a non-intrusive method of measuring species concentration and temperature inside a multiphase reactive environment. It produces path averaged measurement of gas concentration and temperature. With advent of diode laser technology especially for the telecommunication purposes, the lasers can be tuned to a very narrowband of wavelength and can be scanned over the entire absorption feature. With this tunable feature non-resonant noises can be easily taken care of. A recent review by Hanson et al.^[2,16] gives a detailed description of the technique and its applications. TDLAS has been used for measuring the gas concentration inside an industrial coal fired power plant^[2,17]. Simultaneous measurements of CO (near 1.65 μm),

H₂O (near 1.4 μ m), O₂ (near 760 nm) and temperature measurements were made in a 500 MW coal-fired boiler. The CO data was corrected for H₂O interference, similar to the CO measurements in a German coal-fired plant. The temperature was determined by a fit to multiple water vapor absorption values. CO concentration was monitored for detecting the slagging conditions of the burner. Although absorption spectroscopy sensors for power plants are in their infancy, this pioneering work reveals excellent potential for real-time burner optimization accounting for changes in the heating value of the input coal. In another study by Lackner et al. ^[2.18, 2.19], the pyrolysis, devolatilization and char combustion of bituminous coal and bio mass (beechwood, firwood) were investigated in a laboratory-scale fluidized bed combustor by TDLAS.

The design of the TDLAS system is based on measurements within high temperature and high pressure reacting environments that have been reported in the literature. Nagali et al. ^[2.20] have reported measurements of temperature and water vapor concentration in a high-pressure shock tube using a 1388-nm diode laser at a temperature range between 400-1100 K. Li et al. ^[2.21] have used 1340-nm and 1393-nm diode lasers to determine water vapor concentration and temperature measurements within a high-pressure chamber. Upschulte et al. ^[2.22] have reported measurements of CO and CO₂ concentrations in room temperature gas-mixture and in the exhaust gases of CH₄-air flame using a 1570-nm diode laser. It was noted that the CO concentrations must be relatively high to be measurable at this wavelength. Wang et al. ^[2.23] measured CO concentrations in the exhaust and post-flame regions of an ethylene-air flat flame by using a 2300-nm diode laser. Tunable diode lasers around 1388 nm, 2300 nm, and 1570 nm wavelengths enable the measurement of the H₂O, CO₂ and CO species concentrations respectively.

2.2.2.3 TDLAS measurements in the entrained flow gasifier

The design of the optical access spool assembly is described in next part. One of the spool sections of the continuous flow reactor has been modified to hold the optical access. The system is designed for temperatures up to 1300 K at a pressure of 1.3 MPa. Optical access is available from opposite sides of the spool, allowing transmission and collection of a laser beam. The windows (fused silica) are 2.54 cm in diameter and 1-cm thick to meet the pressure and temperature requirements. Nitrogen purge is used for cooling and preventing the deposition of coal particles on the window surfaces. Graphoil seals have been used to secure the access against pressure leaks at high temperature.

The present experimental arrangement is shown in Figure 2.8. Telecommunication type diode lasers (NLK1XXGAAA from NTT Electronics Corp.) have been used for the absorption measurement. The lasers are mounted on mounts (LDM-4980 from ILX Lightwave Corp.) that receive control signals from the laser controller. The laser diode is controlled through two control signals (i) temperature control and (ii) current control provided by an ILX Lightwave laser controller (model LDC 3714B). A ramp voltage signal is provided to the laser controller using a function generator (model 625 from Berkeley Nucleonics). The ramp signal cycles the output current from the laser controller that in turn cycles the laser output wavelength at a known frequency. Using these control signals the laser diode is detuned from its centerline frequency to capture various transitions of interest for the absorbing molecule. Through the fine detuning provided by current control, the entire absorption feature can be captured. The laser is pre-calibrated for the wavelength output using a wave-meter. The ramp signal and wavelength calibration as a function of laser current for the 1388 nm laser is shown in Figure 2.9. The laser beam is collimated and then split into a reference leg and a measurement leg using a beam splitter. The reference leg is further split into two signals with one going to an etalon and the other to a photo detector (model DET50B from Thorlabs Inc.). Real time wavelength measurement is provided by the signal presented to the etalon. The reference signal I_0 is provided by the reference photo-diode. The reference signal could also be obtained by fitting a baseline curve using the wings of the absorption feature. The measurement signal passes through the optical access into the probe volume and is collected by another photo-diode on the other side. Focusing lenses are used because of the long optical access (~ 53 cm). The signal from the measurement photo-diode and the reference photo-diode is collected by the data acquisition system. The signals are further processed to calculate the fractional transmission and the absorbance. The measured absorbance profiles are compared with the simulated absorbance profiles, shown in Figure 2.11, (using HITRAN database) to calculate the species concentration.

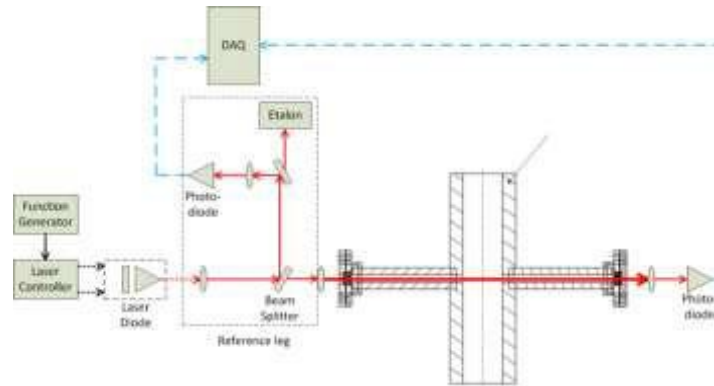


Figure 2.8: Experimental arrangement for absorption measurement on entrained flow

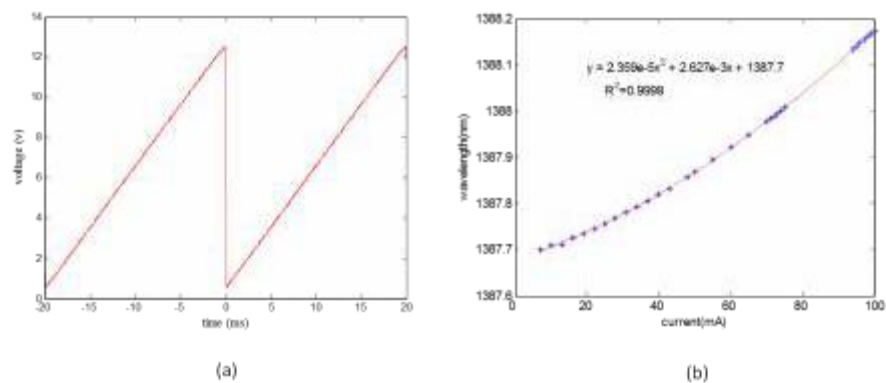


Figure 2.9: Laser characteristics (a) ramp voltage provided by the function generator (b) wavelength output of the laser.

A photograph of the laser system mounted on the reactor is shown in Figure 2.10.

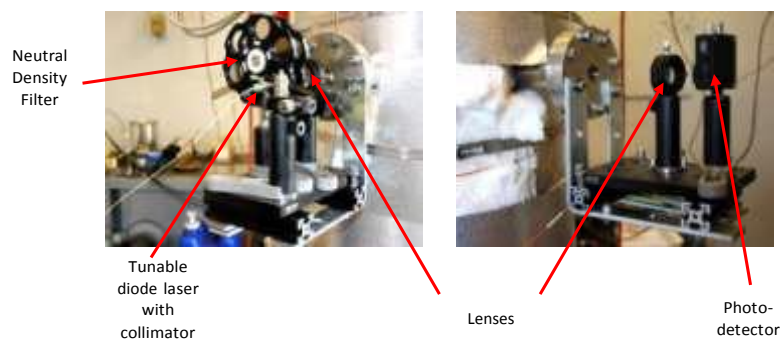


Figure 2.10: Photograph of the TDLAS system mounted on the entrained flow system.

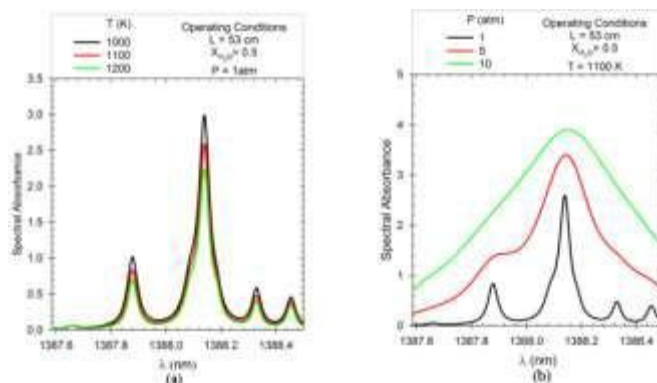


Figure 2.11: Spectral absorbance for H₂O near 1388.2 nm.

The optical ports are sealed using grafoil gaskets and flanged connections. To prevent accumulation of solid particles on the window surfaces, the system includes a manifold which maintains a continuous nitrogen purge across the optical windows. A schematic and a photograph of the optically accessible spool piece are shown in Figure 2.12.

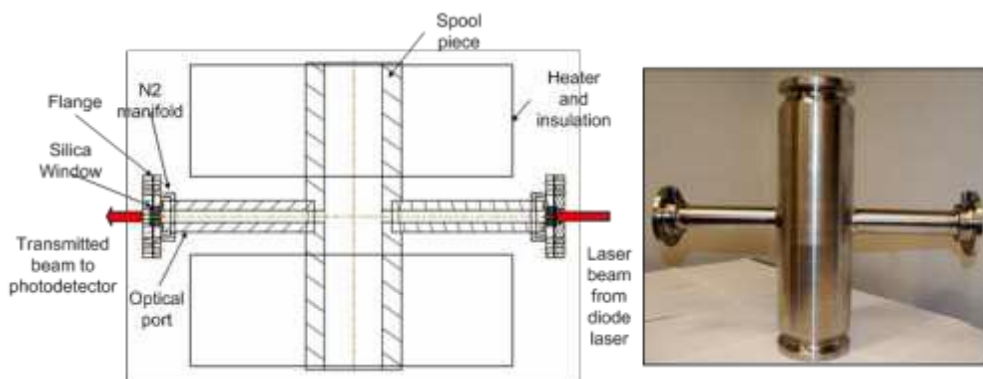


Figure 2.12: Schematic of the optical spool piece (left) and the actual hardware (right).

2.2.3 Hydrogen-Oxygen Steam Generator

The hydrogen-oxygen steam generator was developed from concepts based on rocket combustors and is displayed with all reactant and product flows in Figure 2.13^[2.24-2.26].

Superheated steam (1100 to 1400 K) at high pressure (1.0 to 1.2 MPa) is produced inside the steam generator by quenching the products of a H₂-O₂ flame. Hydrogen and oxygen inlets are located on the main casing and their mass flow-rates are controlled using sonic venturis. The entire oxygen flow and a portion of the hydrogen flow, termed core flow, are directed along the inside of the insert plug through a manifold. A fuel-lean pilot flame is formed inside the insert plug. Initial ignition is provided by a spark plug situated at the top of the main casing. Typical equivalence ratios inside the insert plug range from 0.22 – 0.26. The remaining portion of the hydrogen flow, termed sleeve flow, is diverted through the annulus surrounding the insert plug. The sleeve flow surrounds the outer wall of the insert and provides cooling. At the end of the insert, the sleeve flow mixes with the pilot flame and forms the main H₂-O₂ diffusion flame. The global equivalence ratios for the main flame can be varied from 1.0 - 2.0 by adjusting the sleeve mass flow rate; thus the steam generator can be operated under fuel rich conditions with excess H₂ concentrations.

Atomized liquid water sprays quench the main diffusion flame downstream of the main casing. The cooling water is injected into the main combustion chamber through micron-size orifices. The quenched flame passes through the interface piece that enhances mixing between the cooling water and flame. The connecting tube transports the steam

from the interface piece to the gasification reactor. Finally, a sonic venturi located at the end of the connecting tube controls the steam flow-rate. The pressure inside the steam generator is maintained to ensure that the sonic venturi remains choked.

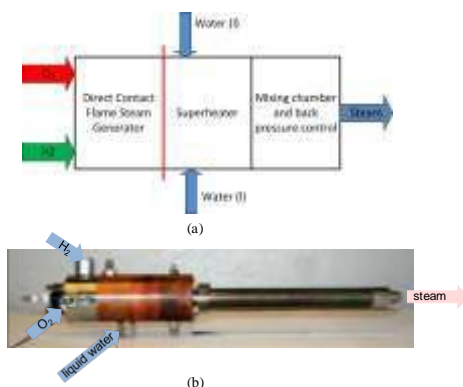


Figure 2.13: The schematic (a) and the actual (b) hydrogen-oxygen steam generator.

Prior to installation in the gasifier, experimental investigations were conducted to verify hardware reliability and assess the capability to meet the operating parameters shown in Table 2.1. Figure 2.14 shows the steam generator chamber pressure and steam temperature time history for the first 4 minutes of operation at stoichiometric operating conditions. Steady state conditions inside the steam generator were achieved after approximately 120 seconds. The initial spike in the steam generator temperature corresponds to the operation of the spark.

Figure 2.15 also shows a comparison between calculated and measured thermodynamic properties (pressure and temperature). The thermodynamic properties were calculated iteratively. The chamber pressure was calculated by starting with an initial guess of temperature for sonic condition at the throat. The calculated pressure was then used to update the temperature based on adiabatic chemical composition. The iterations were continued until an error criterion was met ($\text{error} < 10^{-9}$). For these calculations complete evaporation of liquid cooling water was assumed. The calculated temperature was assumed to be the stagnation temperature at the exit of the sonic nozzle.

The measured chamber pressures are in good agreement with calculated values. The chamber pressure is found to increase with increasing equivalence ratios. This increase is attributed to the increased mass flow rates inside the chamber due to greater hydrogen mass flow rates. The steam temperature was measured using a thermocouple located at the end of the connecting tube at atmospheric pressure. This measured temperature shows a good agreement with the calculated temperature at the throat of the sonic venturi.

These results verify operation of the steam generator meeting the design conditions outlined in Table 2.1. Following these experiments, the steam generator was installed onto the reactor vessel as shown in Figure 2.3 and has been operated without incident for multiple long duration experiments (30 min).

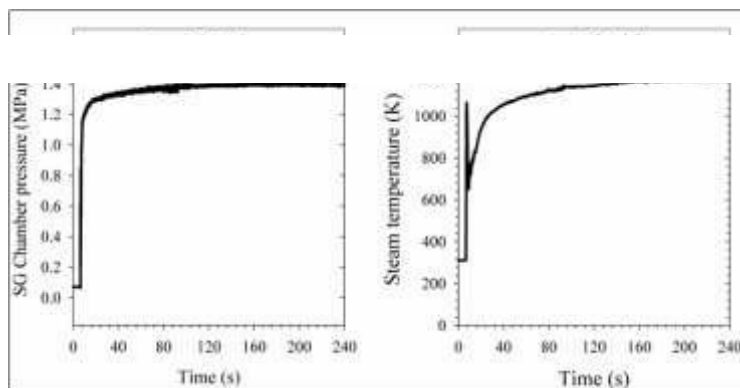


Figure 2.14: Steam generator chamber pressure (left) and steam temperature (right) time history for stoichiometric operation.

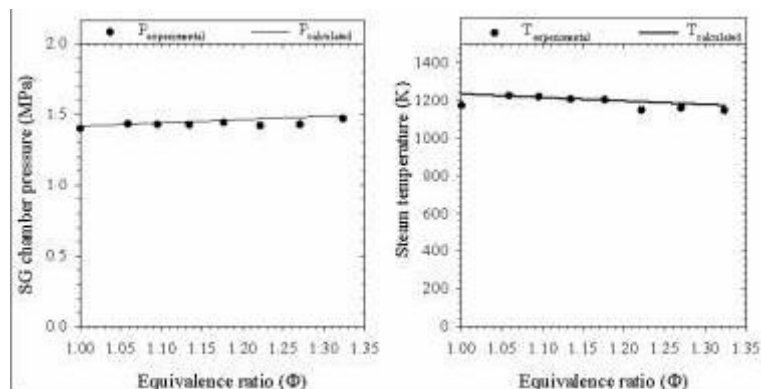


Figure 2.15: Comparison of theoretical and experimental steam generator chamber pressure (left) and steam temperature (right) for varying equivalence ratio.

2.2.4 High-Pressure Coal/Biomass Feeder

A high-pressure powder-feeder system shown in Figure 2.16 is used to displace coal into the gasifier. The system consists of a stainless steel auger (helical screw), a servo motor, a pressurized hopper, a water cooling jacket, and a reactor interface tube. The hopper holds pulverized feedstock ($\sim 50 \mu\text{m}$ avg. dia.) that falls into the auger tube. The rotating auger displaces a metered quantity of feedstock into the feed tube. The feed tube is pressurized with nitrogen that reduces the penetration of steam into the feeder and pushes the coal from the tip of the tube into the reactor. A nitrogen feedback line is connected between the feed tube and the hopper to achieve a minimum pressure gradient across the positive feed system. This makes the flow rate of the coal feed and its measurement independent of the downstream reactor pressure. Farias et al.^[2,27] used a similar feeder design for operation at high pressure.

The coal feeder is designed for operation at 2 MPa while maintaining a temperature of 300 K. The water cooling jacket helps to maintain this temperature by removing heat conducted from the reactor along the tubing. Dynamic sealing between the slowly rotating auger shaft and the auger tube is achieved through two Viton O-rings placed inside the auger tube. The feeder interfaces with the reactor through a high-pressure and high temperature coupling. The feeder is supported from a pulley and is counterbalanced using a balancing weight, allowing it to move freely as the reactor vessel expands and contracts vertically. This motion eliminates bending moments and stresses on the feeder tube and auger.

Operation of a pressurized screw feeder was demonstrated at atmospheric and high pressure conditions. Experimental arrangement and procedures for calibration of the feeder were developed and demonstrated using anthracite and bituminous coal and coconut char. Good repeatability in measurements was obtained for coconut char calibration at both atmospheric and high pressure. The experimental results were compared with theoretical

calculations and were in close agreement with each other. An optically-accessible flange was incorporated in the feeder design to monitor the experiment. These observations were used to improve the feeder performance by making changes to the vibrator parameters on the hopper and the test procedures. The effect of moisture on the flowability of coal and biomass was studied and it was concluded that dry feedstock is essential for proper flow from the feeder. This was accomplished by baking of feedstock before experiment and storage in an inert environment.

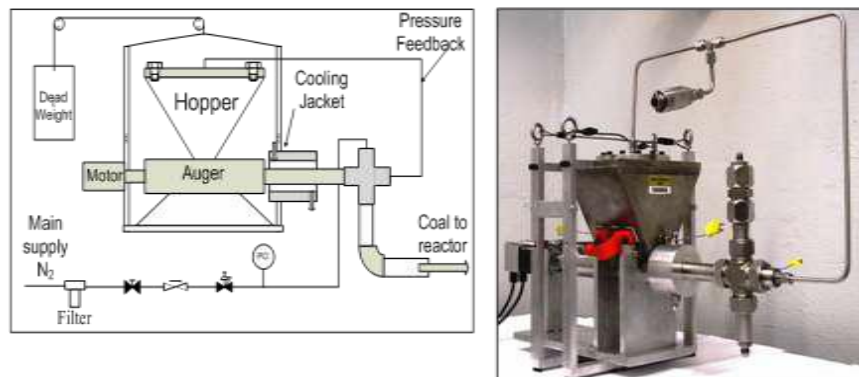


Figure 2.16: Schematic (left) and image (right) of the coal/biomass feeder.

Figure 2.17 displays the mass flow-rate calibration curve as a function of the motor speed for Anthracite type coal and coconut char. The coals and biomass are typically ground to approximately 50-micron particle sizes. Slurry rheologies and granular-flow phenomenon determines the shapes of the curves. Calculations based on the work by Sander and Schonert were performed and are presented with the experimental curves. Parameters for the calculation are summarized in the Appendix.

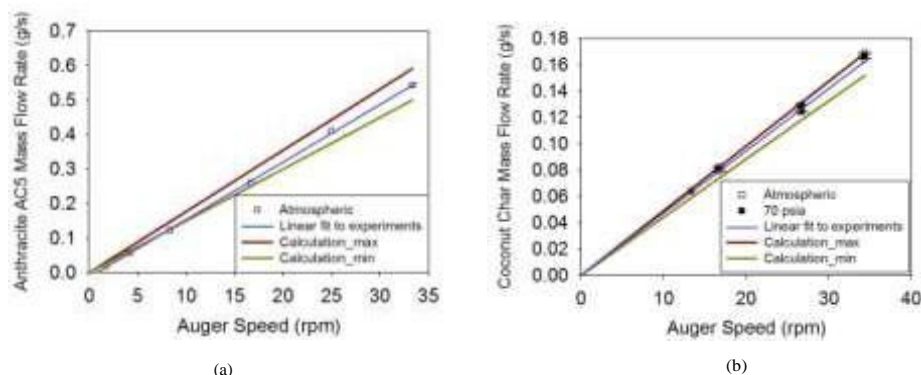


Figure 2.17: Anthracite coal (left) and coconut char (right) flow-rate trend with motor speed.

2.2.5 Gas Sampling and Collection

Figure 2.18 displays a schematic of the gas sampling and collection system. This system contains a filter to remove solid particulates, a condenser and liquid-gas separator to remove water, and a line for capturing gas samples into sample bags for analysis using a gas chromatograph. Initially, the sampling bags are evacuated using a vacuum pump. A sample is collected by directing the exhaust gases into the sampling bag. Once filled, the sampling bag is sealed and the gases are directed to the exhaust again. The manual sampling system enables sampling at approximately 1 minute intervals.

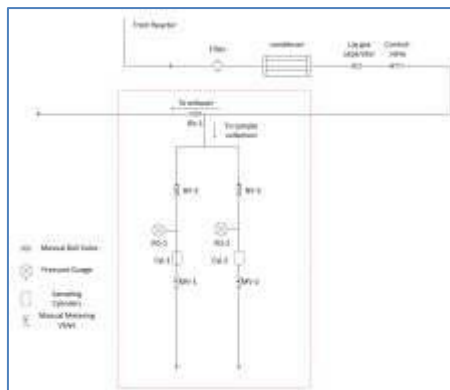


Figure 2.18: Schematic of the gas sampling and collection system.

2.2.6 Continuous Flow System Results and Discussion

Following design, construction, and calibration of all of the sub-components, the entire system was integrated for preliminary gasification experiments. At the start of such an experiment, the reactor was heated to the desired temperature using the radiant heaters. During the heat-up, the reactor is continuously purged with nitrogen. The outer-wall temperatures of each spool piece as well as the gas-phase temperature within the reactor are continuously monitored using shielded thermocouples. Once the reactor temperatures reach the desired temperature, a gasification experiment is initiated. The heating period can require up to 6 hours.

The gasification experiment begins by ignition of the hydrogen-oxygen steam generator. This results in a rise in pressure and temperature within the steam generator as shown in Figure 2.14. Within a few minutes, the steam generator achieves steady state operation. At this point, coal is injected using the coal feeder. Release of volatiles and gasification of the char causes an increase in the total system pressure. Finally, the system pressure is slowly brought to the desired operating conditions by adjusting the pressure drop across a computer-regulated needle valve located in the exhaust stream. Once the system reaches steady-state operation, gas samples are collected using the sampling system.

A number of system-integration experiments have been performed. Product gas analysis of the collected gas samples has indicated the presence of carbon containing species including CO, CH₄, and CO₂. This is strong evidence of successful gasification.

The objectives of this experiment included:

1. Demonstrate the operation of the continuous-flow gasifier arrangement through the gasification of coconut char particles in a steam environment.
2. Perform preliminary TDLAS measurements to demonstrate TDLAS operation.

Table 2.2 lists the operating parameters of the gasifier integration tests. The number of operating parameters conveys the complexity associated with the operation of the continuous-flow gasifier arrangement.

Table 2.2: Operating parameters for the biomass gasification experiment.

Operation Parameter	Unit	Value
Total hydrogen mass flow rate	g/s	0.51
Oxygen mass flow rate	g/s	2.66
Cooling water mass flow rate	g/s	6.57
Steam flow rate to gasifier	g/s	1.2
Steam flow rate to vent	g/s	8.6

Total steam flow rate	g/s	9.8
Steam generator equivalence ratio	g/g	1.5
Feedstock		Coconut char 5562
Average particle size	micron	50
Feedstock preparation	Baked at 100 °C for 12 hours and stored in an inert glove-box prior to gasification.	
Feedstock flow rate	g/s	0.12
Nitrogen flow rate for optical window purge	g/s	0.04
Nitrogen flow rate through coal feeder	g/s	0.09
Total nitrogen flow rate	g/s	0.13
Heater set point temperature	K	1100
Reactor pressure	MPa	1
Diagnostics	TDLAS, high-speed imaging, pressure and temperature measurement, product gas characterization using Multi Gas Analyzer.	

Multiple gas samples were collected during the experiments. The first sample was collected before the start of the powder feeder. This sample can be used to quantify the products of combustion from the H₂-O₂ steam generator and to determine gas-phase carbon containing species that may be present due to gasification of small amounts of residual coal and char within the gasifier. Table 2.3 presents a summary of events during the experiment.

Table 2.3: Summary of experimental operation.

Event	Time from start of steam generator
Steam generator started	0
Background sample (Sample 1) collected at gasifier pressure 72 psia	8 min 45 s
Coal feeder started	10 min 40 s
Sample 2 collection started at gasifier pressure 145 psia	16 min 10 s
Sample 3 collection started at gasifier pressure 140 psia	20 min 10 s
Coal feeder stopped	27 min 30 s
Sample 4 collection started at gasifier pressure 137 psia	30 min
Steam generator stopped	30 min
Total test duration	30 min
Coal feed duration	17 min 40 s

Figure 2.20 shows the experimental reactor pressures verified with three independent pressure transducers. Following the start of the steam generator and closure of the control valve, the reactor pressure raised to 0.50 MPa at which point the first gas sample was obtained. Following this, the reactor pressure was allowed to continue increasing until it stabilized at approximately 0.76 MPa. At that point, the feeder was started to inject biomass into

the reactor. Entrained flow was verified using high-speed imaging through the optical access for entrained biomass particles. Following biomass injection, the pressure within the gasifier rose, possibly due to gasification. As the pressure approached approximately 1 MPa, the control valve was manipulated to maintain an approximately constant pressure. Five minutes and thirty seconds after the start of the biomass feed the second gas sample was obtained. A third and fourth sample was obtained at 9 min 30 s and 19 min 20 s after the start of the feeder respectively.

High speed visible imaging was used to visualize a coal particle laden steam flow through the optically accessible gasification chamber at a pressure of 1 MPa and a temperature of 1100K. A high-speed camera (Vision Research Phantom v7) with a 105 mm lens was mounted perpendicular to gasification chamber and focused on the chamber centerline. A 1000 W arc lamp and diffuser plate were positioned on the opposite side of the chamber to provide adequate backlighting conditions. The spatial resolution was approximately 80 μm for each pixel at the center of the chamber. The camera integration time (20 μs) and aperture size were adjusted to optimize the camera sensitivity. Data was collected at a nominal sampling frequency of 10 kHz resulting in 100 μs between consecutive images.

Figure 2.19 (a) - (f) show six representative visible images of the coal particles flowing through the gasification chamber. The field of view is approximately 24 mm square, and the flow direction is from top to bottom in the same direction as gravity. Well-established correlation-based tracking techniques, developed and utilized within the particle image velocimetry community, were applied to these path-integrated measurements. The average velocity of the particles is estimated to be 0.6 m/s resulting in an expected residence time of 2.5 s based on the 1.5 m length of uniformly heated gasification chamber. The large range of individual particle sizes apparent in the images leads to a range of particle velocities. Additional analysis will estimate a probability density function of the velocity distribution.

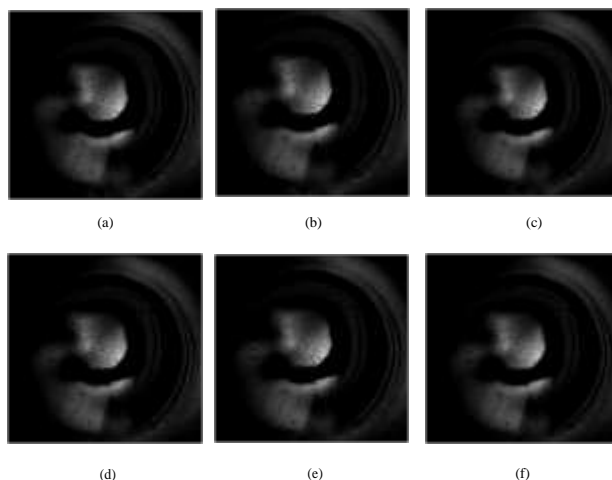


Figure 2.19: High speed visible images of a coal laden particle flow through a gasification chamber at a pressure of 1 MPa and temperature of 1100 K.

Near the conclusion of the gasification experiment, the biomass feeder stalled. This indicated a possible clogging of the feeder. At that point, nitrogen was rapidly injected into the feeder using a line installed prior to experiment for this specific purpose. This nitrogen injection resulted in the pressure and temperature variations seen in Figure 2.20 and Figure 2.21. After this injection, the feeder was started again, but became clogged shortly thereafter. At that point, the experiment was stopped to diagnose the feeder issues.

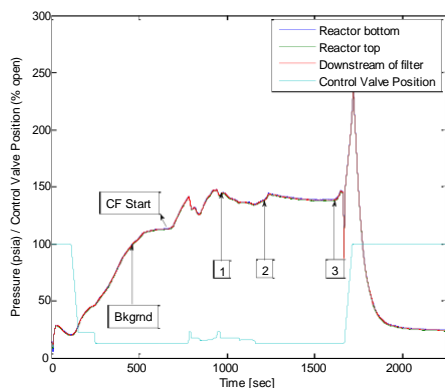


Figure 2.20: Pressure in the reactor vessel during the gasification experiment.

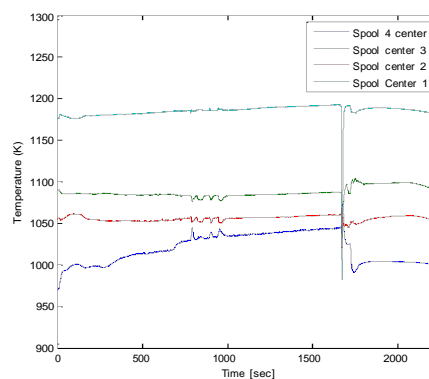


Figure 2.21: Gas-phase temperatures at the center of the reactor.

Four gas samples were collected during the gasification experiment. The collection times for the samples are given in Table 2.3. The MGA is capable of detecting CO_2 , CO , CH_4 , NO , NH_3 , C_2H_6 , C_2H_4 , O_2 , C_2H_2 , H_2O , SO_2 , NO_2 , C_3H_6 and C_3H_8 . However, only the major constituents of interest are reported here.

Table 2.4: Gas composition as measured with the MGA.

Species	CO (%)	CO_2 (%)	O_2 (%)	CH_4 (%)
Sample 1	0.21	1.64	0.7	0.14
Sample 2	0.64	1.15	0.9	0.14
Sample 3	0.38	1.00	0.6	0.13
Sample 4	0.15	0.80	0.6	0.09

The presence of carbon-containing gas-phase species verified that gasification reactions had occurred. Further integration experiments were required to attain full operability of the system. However, time and man-power constraints forced the group to pursue testing on a smaller and simpler fixed-bed, which will be described in the next section.

Identical experiments were conducted using an anthracite coal as the feedstock. In this experiment, ten samples were collected using gas sampling bags as opposed to cylinders. The temperature and pressure history during the gasification experiment are presented in Figure 2.22 and Figure 2.23 respectively. Figure 2.23 also shows the instance of product gas collection during the gasification experiment.

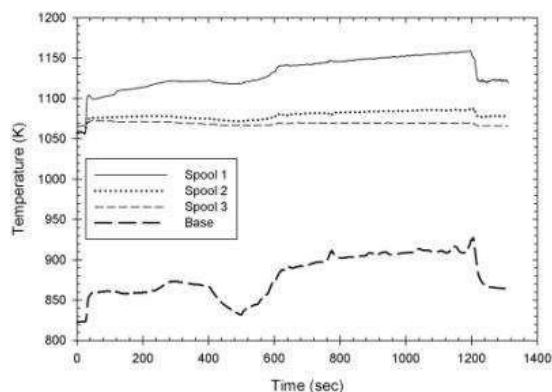


Figure 2.22: Temperature history for the reactor during the anthracite gasification experiment.

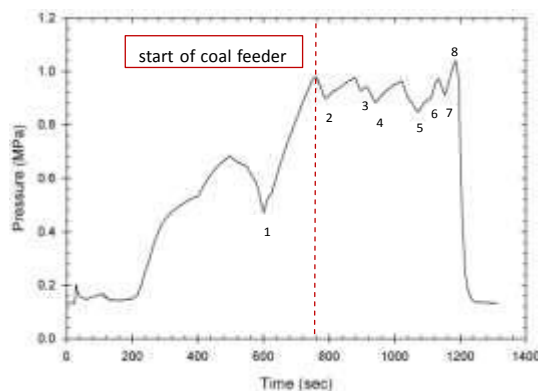


Figure 2.23: Pressure history for the reactor during the anthracite gasification experiment. Instance of sample collection are indicated by numbers.

Product gas composition showed the presence of carbon-containing gas-phase species. The dry gas composition demonstrates the onset of gasification and is presented in Figure 2.24.

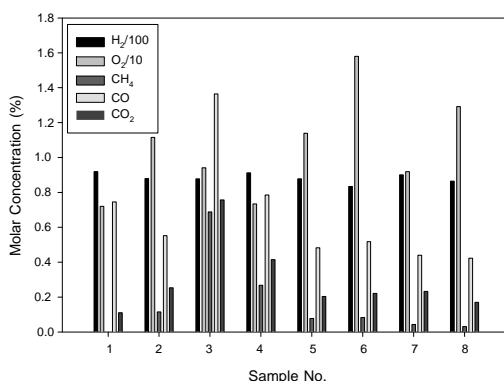


Figure 2.24: Dry product gas composition.

These experiments have been repeated using coconut char based biomass and anthracite coal. The experiments demonstrate that gasification is occurring within the continuous-flow system. Future work on the gasifier will include TDLAS measurements for water-vapour and CO composition and gas-phase temperatures. The objective of the studies will be to develop in-situ measurement techniques for monitoring gasifier operation and determine chemical reaction rate constants. Due to the significant human and time needed to operate the system for a single test, studies were shifted to a smaller and more fundamental fixed-bed configuration that will be discussed next.

2.3 Fixed Bed System

2.3.1.1 Design of the Fixed Bed System

The fixed bed reactor system is built to supplement the continuous flow reactor experimentation. The main objectives for the fixed bed reactor system include:

1. Study the gasification behavior of different carbonaceous feed-stocks (bituminous coal and pine wood saw dust) in presence of single and multi-component gasification environment at different operating parameters
2. Assess the effect of excess H₂ addition to the steam gasification reaction and subsequent CO₂ production
3. In situ real time measurement of H₂O and CO concentration just downstream of (~ 2 cm) the porous bed
4. In situ gas measurement very near to the fuel particle

Figure 2.25 shows the experimental arrangement for the fixed bed experiment. The optical spool section described in the previous section forms the main reactor. A shorter spool section that houses the inlets for reactant gases and pressure measurement device is attached to the optically accessible section with the use of special Grayloc® connectors and seals. These seals are designed for high temperature (~1200 K) and high pressure (~ 1.1 MPa) operation. A similar but smaller spool section that houses the exit port of the reactor is attached to the lower part of the optical piece with similar connections. A stainless steel pipe with OD of 7.3 cm is placed inside the reactor resting on the bottom most flat surface. This pipe supports a porous bed made out of stainless steel 316 sieves. The pipe is not be subject to any pressure loading as it sits inside the pressure vessel. Coal/biomass particles are loaded on a fixed porous bed. The reactant gases enter from the top of the reactor and flow over the fixed bed after passing through a flow straightener. The product gases are formed near the bed and exit the reactor at the bottom. The flow is driven by pressure that is controlled by a control valve downstream of the exit of reactor. The pressure inside the reactor can be controlled at any value between 0.1 to 1.1 MPa by tuning the control valve downstream of the exit of the reactor to an appropriate value. The maximum allowed temperature in the reactor is ~ 1300K but operating temperature depends on the severity of corrosive environments induced by the reactant gases. The reactor

assembly is surrounded by two sets of radiant heaters as shown in Figure 2.25. Radiant heaters provide isothermal environment for the gasification reactions.

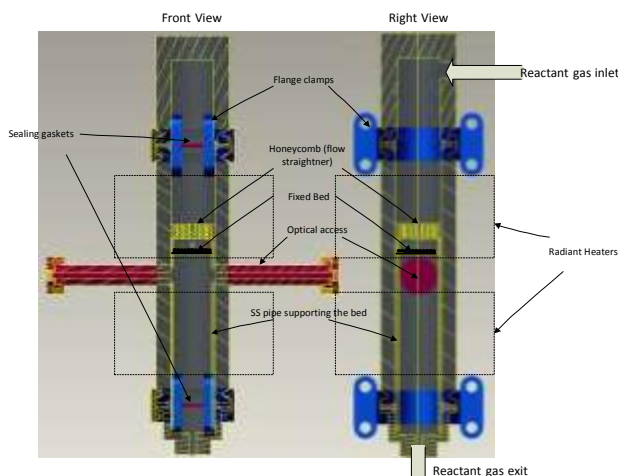


Figure 2.25: Fixed bed reactor arrangement.

2.3.1.2 CO measurement using TDLAS on fixed bed reactor

The survey spectra for CO and CO₂ between 1 and 5 micron are shown in Figure 2.26 (a). The transition of interest for CO lies in the first overtone band (2ν) which is shown in Figure 2.26 (b). The combined survey spectra show negligible interference due to CO₂. The experimental arrangement for CO measurements is shown in Figure 2.27. The arrangement is similar to the arrangement for H₂O detection that has been described above. Hence all the details are not provided. The laser used for the experiment was a high powered DFB diode laser (Sacher Lasertechnik Group) tuned at central wavelength of 2337.4 nm. The effect of temperature and pressure on spectral absorbance of CO is shown in Figure 2.28. The absorbance is found to decrease with increase in temperature and increase with increase in pressure. The behavior is expected.

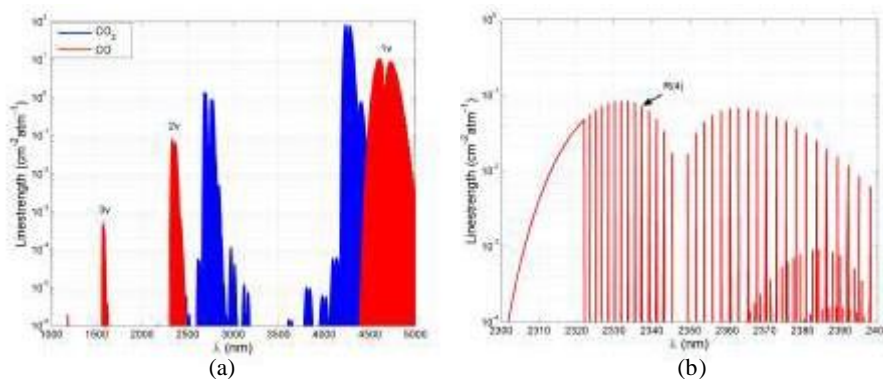


Figure 2.26: Survey spectra at 298 K using (HITRAN 2008) (a) for CO and CO₂ (b) transition of interest for CO.

The spectral absorption curves for CO near this wavelength simulated using HITRAN are shown in Figure 2.28.

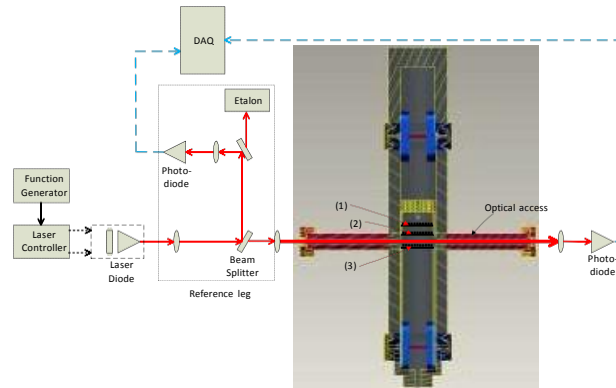


Figure 2.27: TDLAS arrangement for CO detection in the fixed bed.

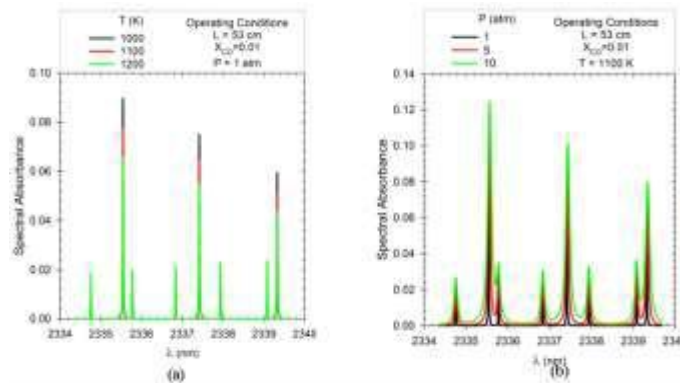


Figure 2.28: Spectral absorbance for CO in the vicinity of 2337.4 nm.

The calibration of laser was done using a pressure cell with fused silica windows. This method was chosen because the available wave-meter could not measure the wavelength in the desired range. Laser scans were taken for reference gas (Air) and a CO + Argon gas mixture (1% CO). The laser scans are shown in Figure 2.29 (a) with y-axis showing the detector output and x-axis showing the laser current. Transmission as a function of current was obtained from CO and Air scans as shown in Figure 2.29 (b).

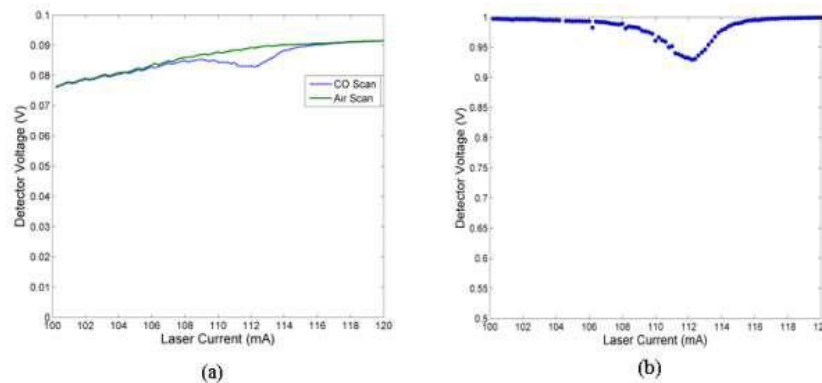


Figure 2.29: Laser scans for wavelength vs. current calibration.

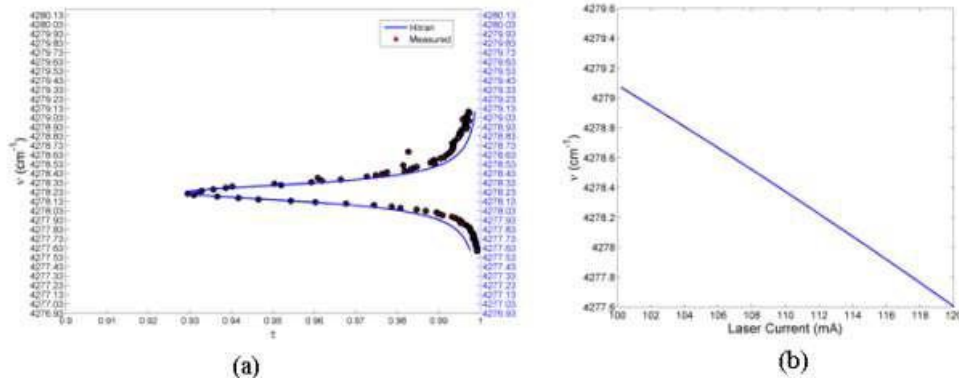


Figure 2.30: Calibration of laser (a) data fit with HITRAN simulation (b) wavenumber as a function of laser current.

The experimental scan was compared with the HITRAN simulation of transmission vs. wave-number for given conditions of pressure (1.8 atm), temperature (298 K) and mole fraction of CO (1%). A data fit for laser temperature of 40 C is shown in Figure 2.30 (a). Wavelength vs. current correlation was obtained from this data fit as shown in Figure 2.30 (b).

CO was detected by probing the R(4) line in a CO+CO₂+Air mixture. The mixture was used because similar reaction environment is expected during gasification. The laser scans are shown in Figure 2.31.

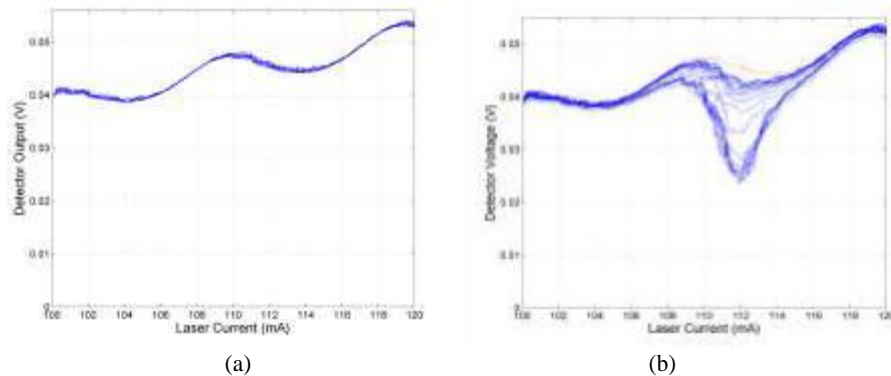


Figure 2.31: Laser scans (a) in N₂ (b) in CO+CO₂+Air mixture.

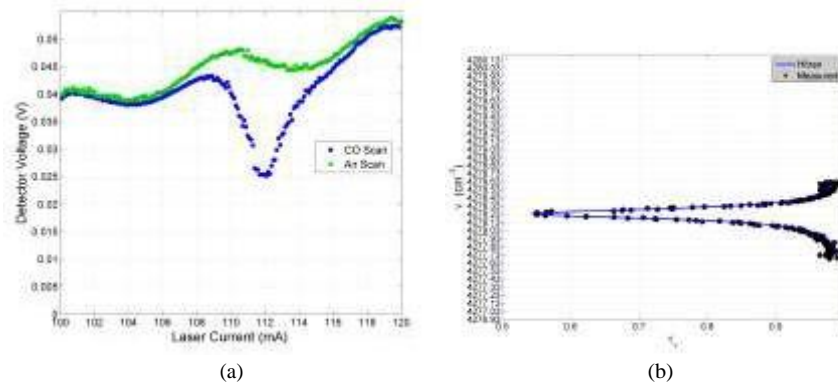


Figure 2.32: Transmission comparison (at T = 301 K and P = 1 atm) (a) data for transmission calculation (b) data fit with simulation.

Reference signal along with the CO scan signal is shown in Figure 2.32 (a). The measured transmission along with the data fit from simulation is shown in Figure 2.32 (b). A data fitting code based on the differential evolution algorithm was developed to fit the simulated transmission to the measured transmission. Mole fraction was varied as a parameter to obtain best fit with the experimental data. For the case shown, the best fit revealed CO mole fraction of 0.03173.

2.3.2 Fixed Bed System Experimental Results

The current section describes the preliminary experimental results from the fixed bed apparatus. Two sets of experiments have been performed so far (i) Biomass (pine wood saw dust) pyrolysis and (ii) Biomass (pine wood saw dust) gasification in presence of CO₂.

2.3.2.1 Biomass Pyrolysis

The test objectives for the biomass pyrolysis included:

1. Investigate the high-temperature degradation properties of pine-wood saw dust in an inert environment
2. Determine the effect of a high-temperature cycle on the fixed bed and honeycomb flow straightener/heater

Table 2.5 shows the operating parameters for the biomass pyrolysis experiment.

Table 2.5: Operating parameters for the biomass pyrolysis experiment.

Operating Parameter	Unit	Value
Nitrogen flow rate	g/s	0.32
Heater set point temperature	K	1173
Reactor pressure	psia	37 psia (minimum pressure attained with control valve fully open)
Mass of biomass loaded	g	4.2828 ± 0.0001
Diagnostics	Gas Sampling and SEM	

The reactant gases consisted only of N₂ to provide the inert environment for pyrolysis. The highest temperature for the experiment was set to be at 1173 K and the reactor pressure was maintained at 0.25 MPa. The initial mass of biomass was ~ 4.28 gm. Gas analysis was done using Multi-Gas Analyzer (MGA) and Scanning Electron Microscopy (SEM).

The experimental conditions are shown in Figure 2.33. The pressure inside the reactor was approximately 0.25 MPa (37 psia). The spikes in pressure indicate the collection of gas samples. Since the sampling cylinders have a large volume (~ 1 L) it creates significant back pressure on the reactor. The temperature trace with time is shown in on the right figure of Figure 2.33. The test continued for approximately 3.25 hrs with maximum temperature of 1173 K.

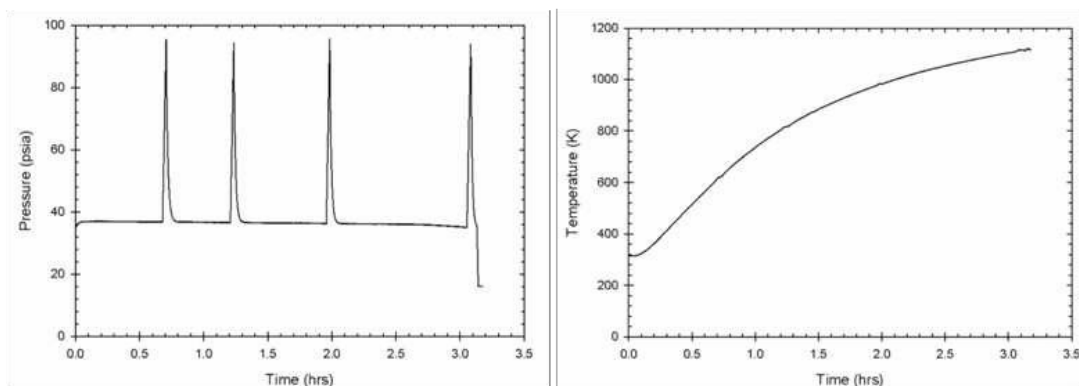


Figure 2.33: Pressure (left) and temperature (right) of the bed during inert heating.



Figure 2.34: Pre and post experiment images of the bed.

The pre and post test images of the biomass in the porous bed are shown in Figure 2.34. As shown in the figure, the biomass shows a significant structural change along with substantial solid mass loss. The mass loss was measured to be 84.1% with uncertainty of 1%. The biomass appears to be shrunk due to pyrolysis. The volatile release from biomass lies in the reported range of 70 to 90% that is typical for pine wood saw dust biomass^[2,28].

The results of gas analysis are shown in Table 2.6. The samples were collected at bed temperature of 573, 773, 973 and 1100 K respectively. The analysis shows that water vapor concentration decreases with increase in temperature. CO and CO₂ are found to be highest in sample 1 indicating highest degree of pyrolysis. Presence of aldehydes is observed in the products which is a typical observation for woody biomass.

Table 2.6: Product gas composition for the pyrolysis experiment.

	H ₂ O (%)	CH ₄ (ppm)	CO (ppm)	CO ₂ (ppm)	Acetaldehyde (ppm)	O ₂ (%)
Sample 1	0.44	121.56	373.69	625.63	96.13	0.47
Sample 2	0.40	568.09	74.13	29.84	0.00	1.13
Sample 3	0.26	60.46	20.86	0.00	0.00	1.05
Sample 4	0.25	35.72	3.20	0.00	63.87	0.87

The biomass pyrolysis experiment showed the successful operation of the fixed bed reactor. The values obtained for the mass loss during pyrolysis are found to be in good agreement with the reported values.

2.3.2.2 Biomass Gasification with CO₂

Five experiments were conducted to investigate the gasification behavior of pinewood in the presence of CO₂. The objective of the experiments was to: 1) investigate the high-temperature gasification of biomass in presence of CO₂ and 2) demonstrate the use of TDLAS for gas-phase specie measurements in a gasifier.

Table 2.7: Operating conditions for the gasification experiment.

Operating Parameter	Unit	Tests 1 & 2	Test 3 & 4	Test 5
Nitrogen flow rate	g/s	0.05	0.050	0.05
CO ₂ flow rate	g/s	0.15	0.150	0.074
Bed temperature	K	1100	1100	1150
Reactor pressure	MPa	0.1 (atmospheric)	0.1 (atmospheric)	0.1 (atmospheric)
Mass of biomass loaded	g	6.5		
Diagnostics		Gas sampling, SEM, EDS	Gas sampling, SEM, EDS	Gas sampling, TDLAS
Test duration	minutes	30	60	60

The operating conditions for all experiments are shown in Table 2.7. Pyrolysis formed the first step of the experiment. The biomass sample was heated to the set bed temperature in an inert environment consisting of N₂. After that, the flow was switched to CO₂ with N₂ flowing as a tracer gas. The reactor pressure was maintained at nearly atmospheric condition. The initial solid mass loading was kept constant at approximate 6.5 grams. Gas chromatography was used to determine the product gas composition and SEM was used to analyze the structure of the biomass particles. TDLAS was utilized in the third experiment for tracking the concentration of CO from the gasification reaction.

The experimental conditions of pressure and temperature during Tests 1 and 2 are shown in Figure 2.35. The temperature graph plot represents the entire experiment thus the time scale ranges for 3.5 hrs. The pressure in the reactor during the gasification experiment is maintained at nearly atmospheric conditions as shown. The negative spikes indicate the operation of the vacuum pump just before collecting each sample. The temperature of the bed is maintained around 1100 K for the gasification experiment as shown in Figure 2.36. Tests 3 and 4 were conducted at similar conditions for sixty minute duration.

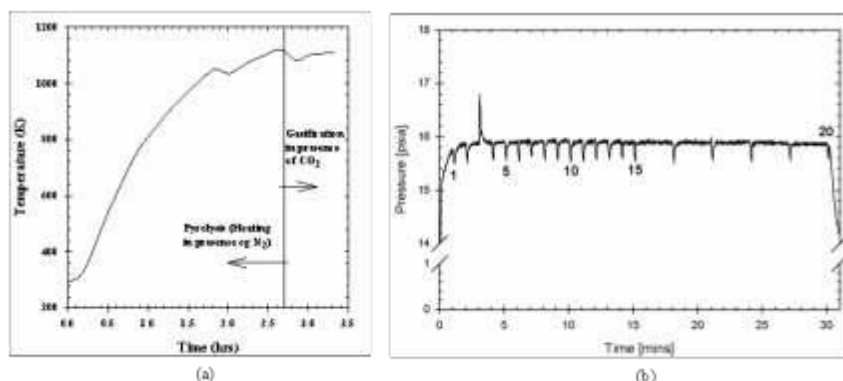


Figure 2.35: Experimental conditions for biomass gasification during Test 1. Temperature (left) and pressure (right) for the complete experiment - inert heating and gasification - are shown.

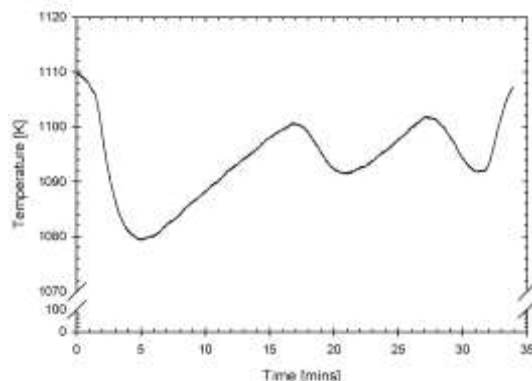


Figure 2.36: A close-up of the bed temperature during the gasification stage.

Figure 2.37 shows the image of the biomass contained in the bed after the experiment. The mass loss during the experiment was $\sim 95\%$ of the original mass of the biomass with uncertainty of 1%. Formation of ash was visible on some particle indicating that the gasification was initiated during the experiment.

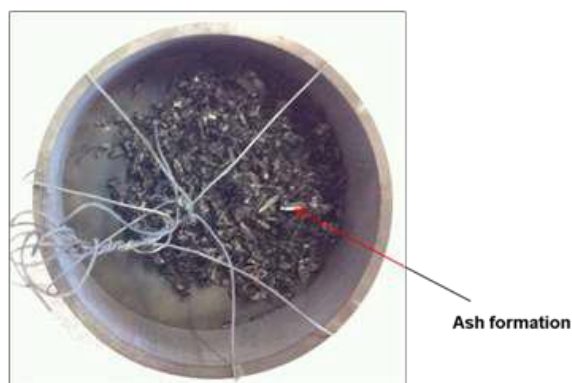


Figure 2.37: Pinewood sampled retrieved after the gasification experiment.

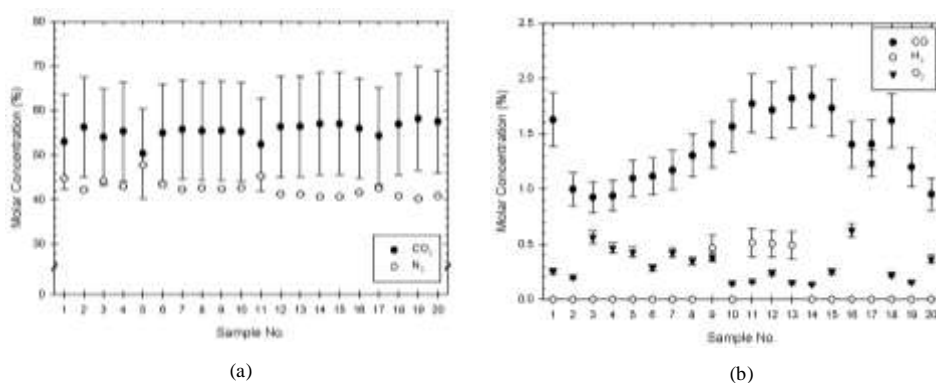


Figure 2.38: Product gas analysis post gasification test (a) major species and (b) minor species.

The product gas analysis from Test 1 is depicted in Figure 2.38. CO_2 was used as the main gasifying agent and N_2 as the main tracer gas. These two gases constitute the major species in the products, as shown in Figure 2.38 (a). The minor species are shown in Figure 2.38 (b). A similar minor species product gas composition for Test 2 is shown in Figure 2.39. CO concentration is highest at the in the initial stages of gasification in both experiments. Thereafter, the CO concentration decreases and gradually increases with sample number (also corresponding to increase in time) with a second peak around sample number 10 to 13 (~ 10 to 13 min). After that it is found to tail off with increased

sample number. CO is the main marker for CO₂ gasification and its increased concentration confirms inception of gasification. Similar analysis was conducted for Tests 3 and 4.

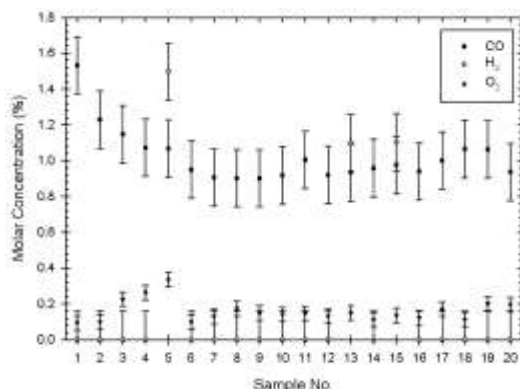


Figure 2.39: Product gas composition data showing the minor species for Test 2.

The mass flow rate of CO is calculated based on the molar concentration and the known mass flow rate of N₂. The CO mass flow rate is correlated to the carbon conversion rate through the stoichiometry of the CO₂ gasification reaction. Therefore, carbon conversion rate is calculated based on the CO flow rate measurement. The carbon conversion rate is assumed to be constant through the previous sampling interval. Assuming ~ 85% solid mass loss during pyrolysis the amount of fixed carbon available for gasification is calculated. Based on the available value of fixed carbon and carbon conversion rate, the conversion history with time (sample number) is obtained. As shown in Figure 2.40, the carbon conversion rate is found to increase with time and then tail off. The carbon conversion plot shows the inception of the gasification reaction followed by an increase in the conversion rate. The curve flattens towards the end of the experiment. This behavior is typical for conversion of any carbonaceous material. The increase in conversion is associated with the increased surface area of the sample^[2,29].

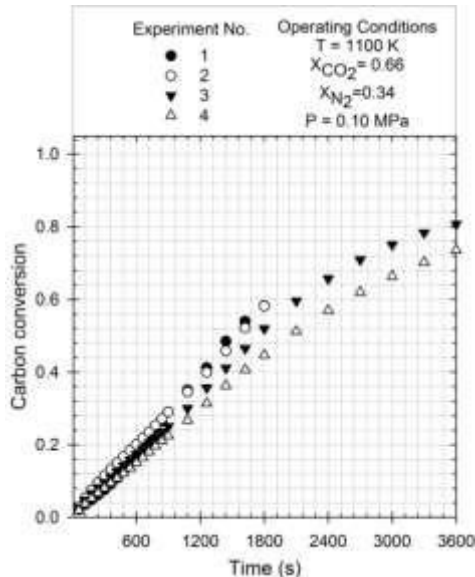


Figure 2.40: Carbon conversion history during biomass gasification experiments for Tests 1 - 4.

The maximum carbon conversion rate is found in the range of 20 to 60 % total conversion. Carbon conversion was measured by comparing the mass of the sample before and after gasification. Alternatively, the carbon conversion was also equated based on the CO flow-rates. The error between the two values differed by less than 10% and verified the onset of gasification during the experiment. Tests 1 and 2 converted approximately 60% of the total carbon in the thirty-minute test duration. The sixty minute experiments in Tests 3 and 4 resulted in approximately

80% carbon conversion. The remaining mass consists of carbon and ash. The resilient carbon is thought to be a byproduct of long-duration and high-temperature annealing^[2,30]. Future work to investigate the characteristics of the resilient carbon is planned utilizing the x-ray diffraction technique (XRD).

Scanning electron microscopy was used to acquire and compare micrographs of the original sawdust and post-experiment biomass from the CO₂ gasification experiment. A sample of representative images from Tests 1 and 2 are presented in this report. Images of gold-coated specimen were acquired at magnifications from 65X to 250X at an electron beam acceleration voltage of 10kV. The images in this report have been resized and do not retain their original magnifications. Additional imaging parameters included a working distance of approximately 10 mm and a beam spot size of 4.

Figure 2.41 shows two images (a,b) of the sawdust used for the gasification experiment. Each sawdust strand was several millimeters in length and approximately 5 millimeters in width. Therefore, a group of sawdust could not be imaged even at the lowest magnification (20X) via the SEM. Images 'a' and 'b' represent the biomass surface at 65 and 250X respectively.

A fibrous material covers the biomass surface in image 'a'. The material appears soft and leafy at 65X. The material crisscrosses across the surface and covers the biomass surface in multiple layers, as that within an onion. Image 'b', acquired at 250X, shows that the fibrous material is composed of parallel wall-like structures that give the sawdust and other woody material their strength and shape. In addition, large pores and crevices are visible throughout the surface of the sawdust at both magnifications. Large divisions between layers enable fluids to penetrate into the strands thus enhancing the apparent reactivity of biomass samples reported in the literature. The resolutions for the unedited images 'a' and 'b' are 1.28 μm and 0.33 μm respectively.

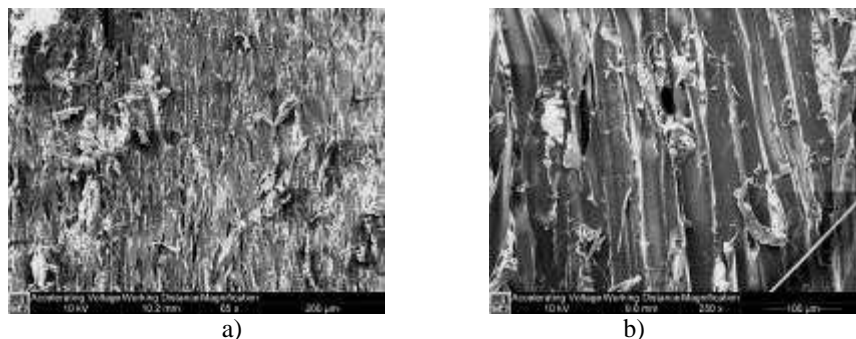


Figure 2.41: Images of non-gasified sawdust particles.

Figure 2.42 shows five images (a-e) of the post-experiment biomass residue. Images 'a' and 'b', acquired at 65X and 250X respectively, show a coarse biomass surface texture in comparison to the original feedstock. The images show large divisions between parallel fiber strands and transverse fractures across groups of parallel strands. Image 'c', acquired at 1000X, shows that the multilayered structure of the biomass (Figure 1.36) has deteriorated; the outer walls of the biomass fibers have been consumed thus revealing skeleton-like interior features. The remaining structures appear stiff, coarse, hollow, thin-walled and tubular. The structure in image 'c' evokes characteristics of dry bamboo or tree bark. Macro pore formation is evident in all three images discussed.

Images 'd' and 'e' have been acquired at 2000X and 12000X respectively. The objective of these images is to determine the extent of pore formation within the biomass. Image 'd' shows enhanced macro pore propagation across the biomass particle. The literature discusses the importance of the micro pore formation in the overall pore development mechanism that occurs during pyrolysis and the onset of gasification; however, the multiple-scale pore structures are seldom shown in a single image, as in image 'e'. Image 'e' shows the complexities presented by the multi-scale pore dimensions towards mathematical representation. Furthermore, images 'd' and 'e' also show that micropores dominate the biomass surface structure and cannot be overlooked in modeling of gasification reactions. The resolutions of the unedited images 'a-d' are 1.28 μm , 0.33 μm , 83.2 nm and 41.6 nm and 6.93 nm respectively.

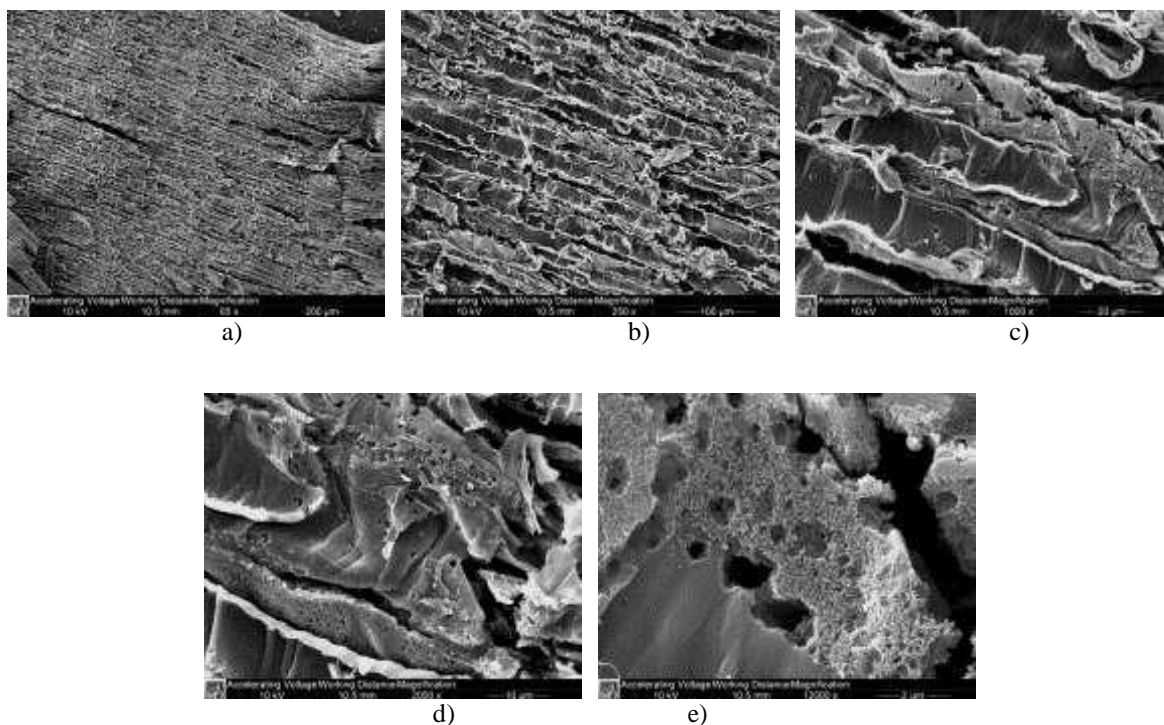


Figure 2.42: Images of post-experiment biomass remains.

The EDS (energy-dispersive-spectroscopy) technique was used to compare the gravimetric elemental compositions of the original pinewood sawdust and the post-gasification residue. The EDS system is coupled to the XL40 FESEM that was used for the SEM analysis. The specimen is deposited onto a resin and then mounted onto a stub using carbon tape. The stub is then placed into the SEM analysis chamber. The sample preparation method is important to note for the EDS analysis since contaminant species from the carbon tape and the mounting resin may appear in the analysis and produce uncertainties. Changes in the analysis parameters also introduce uncertainty in a comparison between two spectra. Similar analysis parameters were maintained for acquiring the EDS spectra for the pinewood sawdust and the post-gasified residue, when permissible. ZAF correction was applied to the data to correct for atomic number, absorption and secondary fluorescence effects. Hydrogen is not detected via the EDS technique.

Figure 2.43 shows the average energy dispersive spectra from Tests 1 and 2 for the original pinewood sawdust and the post-gasified char. Table 2.8 presents the gravimetric elemental composition for the pinewood sawdust and the average elemental composition from Tests 1 and 2 from the post-gasified char for comparison. Elemental composition for pinewood sawdust presented by Bridgewater and Boocock^[2,31] is included for reference. Bridgewater and Boocock^[2,31] also state 6.0% hydrogen content for pinewood sawdust. Some species could not be resolved in both spectra and are denoted by ‘-’.

There is reasonable agreement between the EDS analysis of the pinewood sawdust and the literature analysis considering uncertainties regarding the origin of the biomass and specimen handling. The comparison of the carbon and oxygen content between the original and post-gasified samples reveals proof of gasification, identified by the decrease in the volatile composition and a large increase in the carbon composition. The large carbon content in the post-gasification sample supports the gas composition analysis that longer reaction duration is needed to attain 100% carbon conversion.

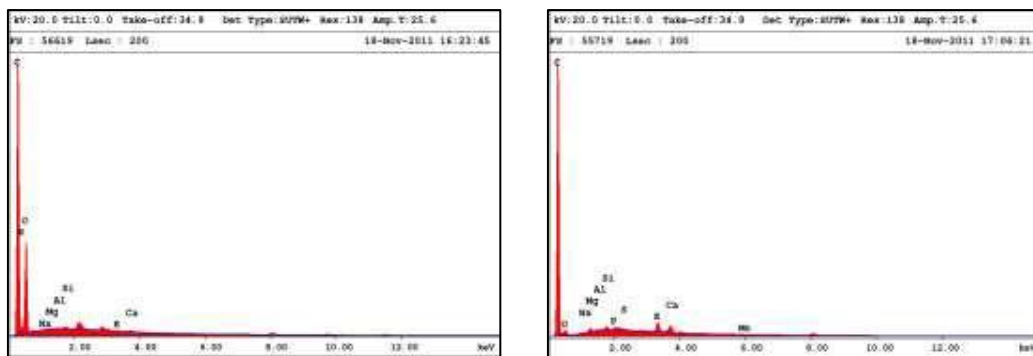


Figure 2.43: Energy dispersive spectra from pinewood sawdust before (left) and after (right) gasification.

Table 2.8: EDS composition analysis for pinewood sawdust and the post-gasified material. Comparison values are shown from the measurements of Bridgewater and Boocock^[2,31].

Sample	Element (weight %)											
	C	N	O	Na	Mg	Al	Si	P	S	K	Ca	Mn
Original	62.65	6.64	30.27	0.02	0.04	0.07	0.11	-	-	0.06	0.14	-
Bridgewater and Boocock ^[2,31]	51.0	0.1	42.8	0.1								
Post-gasified	91.69	-	3.82	-	0.39	0.09	0.36	0.39	0.23	1.61	1.25	0.15

CO detection inside the gasifier using TDLAS

Laser diagnostics was utilized in Test Number 5 to probe the region directly underneath the bed for CO. The bed temperature and the reactor pressure are shown in Figure 2.44. The bed temperature was controlled near 1500 K, which is shown by the red line on the figure. The fluctuations of the bed temperature can be associated to the combined effects of the heterogeneous reactions, the gas-phase reactions and the compensating actions of the heater controller. The reactor pressure was maintained at atmospheric conditions. Spikes on the pressure trace correspond to the instance of product gas collection, resulting in momentary pressure increases. A total of 26 product gas samples were collected. The first 15 were collected at 1 minute intervals, the second 5 were collected at 3 minute intervals and the last 6 were collected at 5 minute intervals. The gasification experiment duration lasted a total of 60 minutes.

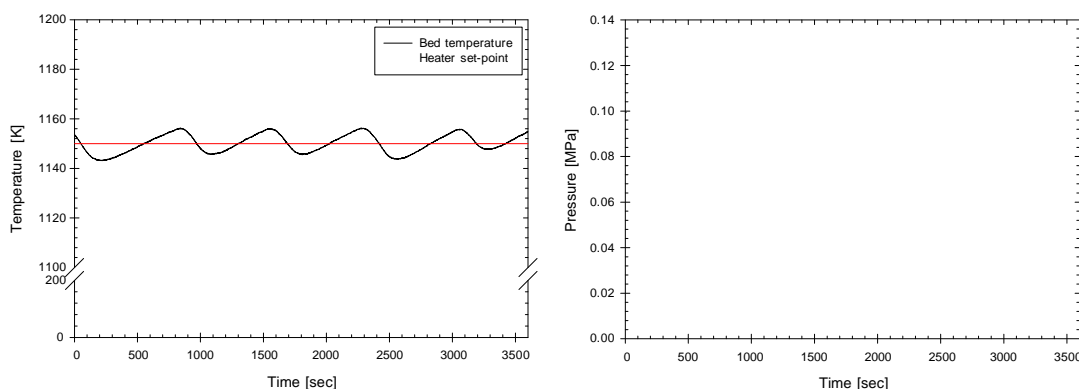


Figure 2.44: Bed temperature and heater set-point temperature (left) and reactor pressure (right) are shown. The spikes on the reactor pressure correspond to instances of product gas collection.

Includes 6.0% hydrogen.

CO was detected by probing the R(4) inside the gasifier during a gasification experiment. Reference signal was collected during the heating period in presence of N_2 and after the steady gasification temperature was reached. The reference signal is shown in Figure 2.45 (a). The gasifier was probed using TDLAS for CO produced during gasification. The CO scan signal is shown in Figure 2.45 (b).

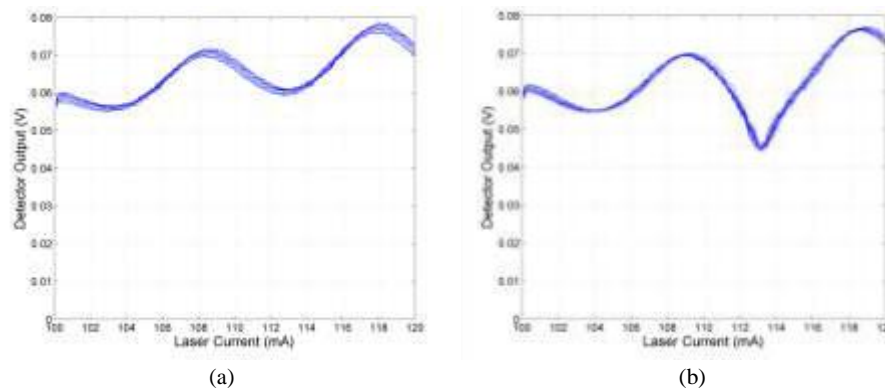


Figure 2.45: Output signal (a) reference signal (b) signal after the CO_2 flow was started.

The transmission of laser radiation during gasification was calculated the CO signal with the reference. The experimental transmission was compared with simulation to calculate the mole fraction of CO inside the gasifier. The data fit for one of the scans is shown in Figure 2.46.

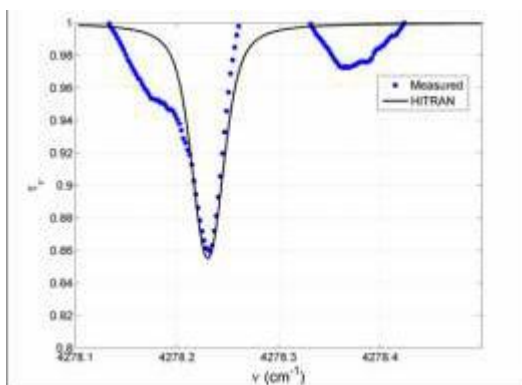


Figure 2.46: Simulation using HITRAN fitted to the measured transmission signal.

A data fitting code based on the differential evolution algorithm was developed to fit the simulated transmission to the measured transmission. Mole fraction was varied as a parameter to obtain best fit with the experimental data. For the case shown, the best fit revealed CO mole fraction of 0.02670. Multiple scans were taken to study the evolution of CO with time. Similar fitting was done for other scans. The evolution of CO as a function of time is shown in Figure 2.47.

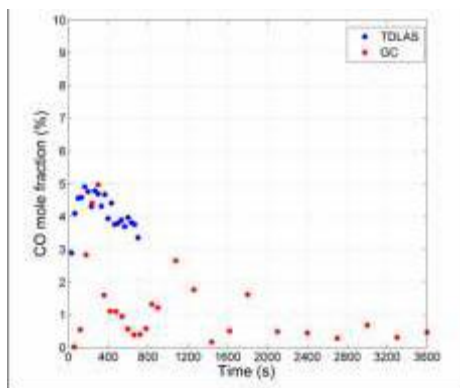


Figure 2.47: Evolution of CO inside the gasifier as a function of time ($T = 1150$ K and $P = 101325$ Pa).

During the initial transience the concentrations predicted by TDLAS show a fair agreement with the GC measurements. However, TDLAS predicts higher concentration of CO in the later part. Absence of window purge (to reduce the noise) during the test might have caused the CO to stagnate near the windows resulting in increased prediction by TDLAS.

2.4 Mathematical Modeling of Coal Gasification

Gasification processes occur at multiple length scales that are characterized by endothermic solid-gas reactions that occur at the solid particle scale (~ 500 μm) coupled with gas phase reactions that span the reactor scale (~ 10 m). Heat and mass exchange between the two phases plays an important role in determining the overall gasification rate. The processes at the particle scale are governed by diffusion of heat and mass to and from the particle along with the solid-gas chemical reactions. The processes at the particle scale interact with the processes at the reactor scale making it a multi-phase multi-scale problem. Mathematical modeling of coal gasification at particle scale has been largely based on quasi-steady approach with co-relations and semi analytical solutions. The analytical solutions may not be valid in different scenarios such as presence of multiple gaseous species, large difference between diffusional and kinetic rates. Unsteady spatially resolved solutions to the reaction diffusion equation around a particle could provide insights related to the gasification processes at the smallest scale. Detailed gas phase chemistry solution in the region surrounding the particle could be helpful in identifying the critical gas phase reactions affecting the gasification process.

During the course of the project mathematical models were developed that addressed the unsteady behavior of gasification and the importance of gas phase chemistry. The models were to assess the possibility of excess H_2 addition to the gasification process. The models and their results are summarized in the following section.

2.4.1 Spatially resolved model for coal gasification at particle scale

Spatially resolved model for the gasification of a char particle in a multi-component gaseous environment was developed. Finite Volume Method (FVM) approach has been used to solve the unsteady reaction diffusion equations at the particle scale. The results of the model were compared with the experimental results. The effect of reaction conditions such as temperature, pressure and particle diameter on the gasification rate was characterized. Dominance of diffusive processes and chemical kinetics in determining the overall gasification rate is identified with variation in temperature. Particle heating in presence of radiative heat transfer from surroundings has been compared with the diffusive heat transfer through the boundary layer. Addition of excess H_2 to the gaseous environment and its effect on the CO_2 production are analyzed.

A coal/char particle composed of pure carbon is considered to gasify in the presence of a gaseous mixture of H_2O , CO , H_2 , CO_2 , CH_4 and N_2 . The model accommodates for three generic shapes of the char particle, i.e. a slab, a cylinder and a sphere using the same mathematical framework. In the present study spherical geometry is considered. The computational domain for a spherical particle is shown in Figure 2.48.

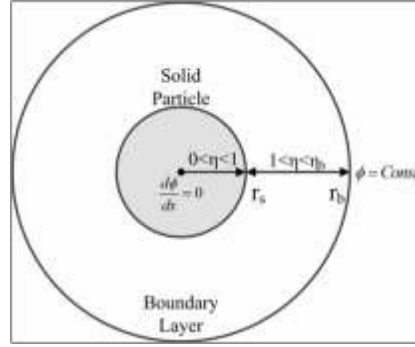
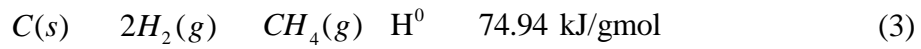
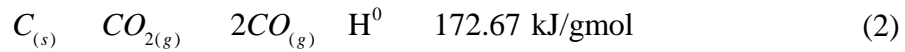
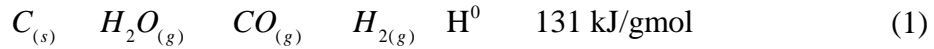
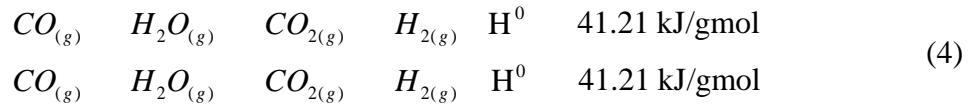


Figure 2.48: Computational domain for particle scale model.

One dimensional reaction diffusion equation is solved inside and around the gasifying particle. Diffusion of heat and mass is considered through the boundary layer and also inside the particle. Thermal conductivity of the gaseous mixture is assumed to vary with temperature however, the conductivity of the solid is assumed to be constant with temperature. The diffusivity of H_2 is assumed to be large as compared to the remaining gases following Srinivas and Amundson^[2.32]. The mixture diffusivity of gas is calculated using the Chapman-Enskog equations. The particle is assumed to be porous. The diffusivity of gases inside the particle is calculated using the porosity and the diffusivity of gases in the free space. The change in the radius of the particle is tracked with respect to time. Shrinking sphere model has been employed for capturing the change in the radius of the particle. The evolution of surface area inside the particle is calculated from a correlation by Dutta et al.^[2.33]. Three solid-gas reactions have been considered i.e. steam gasification (Eq.(1)), CO_2 gasification (Eq.(2)) and methanation reaction (Eq.(3)). The surface kinetics for the three reactions is obtained from Hedden et al.^[2.34], Dutta et al.^[2.33] and Blackwood et al.^[2.35] respectively.



Water gas shift reaction (Eq.(4)) is assumed to be the dominant gas phase reaction with finite rate chemistry and assumed to occur in the entire domain. The kinetics pertaining to coal gasification conditions for the water gas shift are obtained from Wen et al.^[2.36].



The reaction diffusion equation for a generic quantity ϕ for the above mentioned geometries can be written as,

$$\frac{1}{r^n} \frac{d}{dr} \left(r^n \frac{d\phi}{dr} \right) = S \quad (5)$$

where the exponent n takes the values of 0, 1 and 2 for a slab, a cylinder and a sphere respectively. Species conservation and energy conservation is expressed in terms of Eq. (5) with ϕ taking the values of gaseous species' mass fraction Y_i and temperature T . The source terms S account for the generation and consumption of gaseous species due to chemical reactions for species conservation and generation and absorption of heat for energy conservation. The mass of the system is conserved as given in Eq. (6)

$$\frac{d}{dt} \left(\rho_g \right) = S \quad (6)$$

Dirichlet boundary conditions have been used for the gaseous species and temperature at the edge of the boundary layer. The values of temperature and mass fraction of gaseous species are specified at the boundary layer edge and assumed to remain constant with time. Symmetry boundary conditions with zero flux are employed at the center. Radiation exchange between the surface of coal particle and the surroundings are considered with negligible absorption in the gaseous boundary layer. The temperature of the surroundings is specified and assumed to remain constant with time. Radiation is implemented as a surface boundary condition for the outer surface of the coal particle. Equations (5) and (6) are solved using the iterative finite volume approach. The conversion of the particle is tracked until 99% of the initial mass is converted into gases.

Following the treatment by Srinivas and Amundson^[2,32], the volumetric reaction rate for each of the gas-solid reaction is found out using Eq. (7),

$$r_j = r_{sj} S a_0 (1 - X) W_b \frac{kg}{m^3 s} \quad j = 1, 2 \text{ and } 3 \quad (7)$$

In this equation, r_{sj} is the surface reaction rate per unit specific surface area, S is the specific surface area, a is the structural parameter, ρ_0 is the density of coal, X is the local conversion and W_b is the initial carbon content in the coal. a is calculated following the treatment by Dutta et al.^[2,33]. The shrinking sphere model results in a moving boundary problem which is handled using a non-dimensionalization similar to Gupta et al.^[2,37]. In this transformation as shown in Figure 2.48 r_0 is the new stationary variable, r_0 is the initial radius for each domain (for the particle $r_0 = 0$ and for the boundary layer $r_0 = r_s$), δ is the thickness for each domain and Sh is the Sherwood number based on the velocity of the surrounding gases. Sherwood number can be calculated using the Ranz Marshall correlation and its value is assumed to be 2 indicating a stagnant boundary layer around the particle.

After integration over a finite size control volume^[2,38], Eq. (5) can be simplified to,

$$a_p \frac{d}{dt} \left(\rho_p \right) + a_N \frac{d}{dt} \left(\rho_N \right) + a_s \frac{d}{dt} \left(\rho_s \right) = b \quad (8)$$

In Eq. (10) ρ_p is the quantity of interest and ρ_N and ρ_s account for the effect of neighbors. The source terms are included in the term b . Source terms resulting from the non-linear kinetics of the chemical reactions have been linearized using Taylor series approximation^[2,38].

The temperature and species equations are solved iteratively for each time step until a specified convergence criterion is met. Tri-diagonal Matrix Algorithm (TDMA) is used to solve the resulting system of equations. The solution is assumed to converge when the normalized errors for each variable are $< 10^{-4}$. The conversion of the particle is tracked until 99% of the particle is gasified. Due to the implicit time marching the size of time steps do not have any influence on the solution, however, a large time step could make the source terms large resulting in an unstable solution.

Comparison of carbon conversion histories obtained from numerical computations with experimental results by Everson et al.^[2,39] is shown in Figure 2.49. The gasification experiments were conducted on South African coal with mean particle diameter of 70 μm in presence of gaseous environment containing 20% steam and 80% nitrogen. The average surface area measured was 12.1 m^2/g . The computed carbon conversion histories show a good agreement with the experimental results. The model predicts higher conversion rates (15 %) in the initial stages however the decay in the conversion rate predicted by the model is higher compared to the experimental values (10%) by Everson et al.^[2,39]. After gaining confidence from the comparison of the model results with experiments, the model

is exercised to study the effect of operating conditions (Pressure and temperature) on gasification. The gaseous mixture surrounding the particle initially contains nitrogen with nitrogen present inside the pores of the particles. Reactant mixture ($X_{H_2O} = 0.5$, $X_{CO_2} = 0.22$, $X_{CO} = 0.10$, $X_{H_2} = 0.15$, $X_{CH_4} = 0.03$) is added to the reaction at $t=0$. The composition of the reactant mixture is chosen as a representation of generic gasification composition. The results presented are based on the above mentioned reactant composition applied at the edge of the boundary layer^[2,32]. The evolution of gasification is tracked with respect to time. Figure 2.50 shows the effect of pressure on gasification. The total time required for conversion decreases with pressure as shown in Figure 2.50 (a). The effect tends to saturate at higher pressure as observed by Srinivas et al^[2,32]. Figure 2.50 (b) depicts the variation of gasification rate with carbon conversion at different pressures. The gasification rate starts with maximum value in the initial stages. The rate decreases with increase in carbon conversion and for higher conversion ($0.6 < X < 0.9$) the rate of decrease is greater than in the initial stages ($0.2 < X < 0.4$). The rapid decrease in available surface area at higher conversion ($X > 0.9$) causes a sharp decrease in the gasification rate.

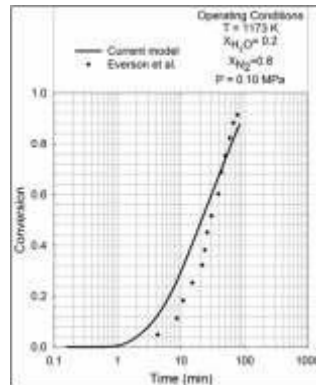


Figure 2.49: Comparison of carbon conversion histories predicted by experiment and the model.

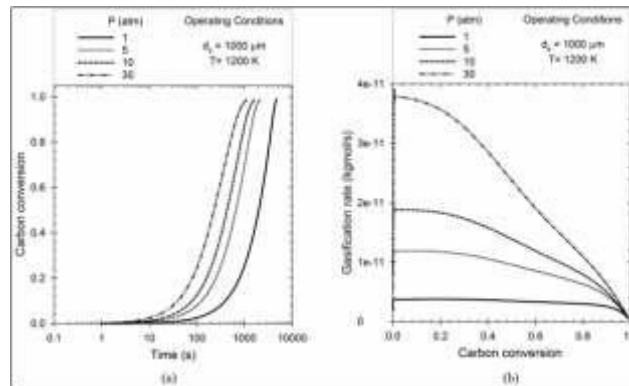


Figure 2.50: Effect of pressure on gasification.

Effect of temperature on gasification is shown in Figure 2.51 (a) and (b). The bulk gas phase temperature i.e. temperature at the edge of the boundary layer is varied to simulate gasification at different temperature. The value of this temperature is held constant for a particular simulation. Figure 2.51 (a) shows a significant decrease (~ 8 to 10 times) in total conversion time with a slight increase in the temperature (~ 200 K). At higher temperature the gasification rate is much faster due to the exponential dependence of chemical kinetics on the temperature. Figure 4b shows the change in gasification rate with carbon conversion at different temperature. For lower boundary temperature (~ 1200 K) the rate is found to decrease continuously with conversion. The gasification rate is found to decrease with reduction in surface area which indicates kinetic control of the reaction. At higher boundary temperature (~ 1400 K) the gasification rate remains almost constant for most part of the conversion ($0 < X < 0.9$) that points towards a balance between chemical kinetics rate and diffusion rate. The trend shows a rapid decrease towards the end ($0.9 < X < 1$) due to reduction in the surface area and in this regime the gasification reaction is

kinetically controlled. With increase in boundary temperature the diffusion in the boundary layer and inside the particle becomes slower as compared to the kinetics and is the rate controlling parameter. With increased boundary temperature the gasification rate is controlled by the diffusive processes rather than kinetics. With increase in conversion that is decrease in particle diameter the diffusive processes become faster resulting in increased gasification rate as shown for $(0.6 \leq X \leq 0.9)$.

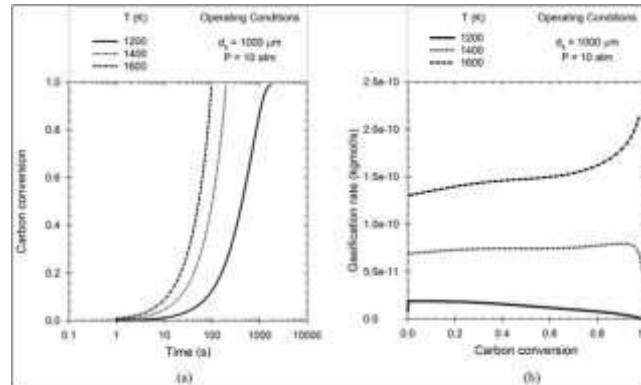


Figure 2.51: Effect of temperature on gasification.

Figure 2.52 shows distributions of temperature and species concentrations within the porous solid ($0 \leq r \leq 1$) and in the surrounding boundary layer ($1 \leq r \leq 2$) plotted as a function of the normalized radial distance. The boundary layer edge is assumed to be at $r = 2$ based on the Sherwood number with value 2. It is expected that the results will not change qualitatively for different values of Sherwood number. The values of different scalars at boundary $r = 2$ are used as Dirichlet conditions. The gradient changes in the CO , H_2O , CO_2 , H_2 and temperature profiles within the boundary layer designate the location of the gas phase reaction front driving the equilibration of the water gas shift reaction. The curvatures in the H_2O and CO profiles at the surface ($r = 1$) result from the surface gasification reactions and differences in inward and outward diffusion rates. The remarkably flat profiles of CO_2 and CH_4 result from the low surface reactivity of these species in relation to H_2O . The remarkably flat profile of H_2 in spite of production by the high reactivity of H_2O at the surface results from the high differential diffusivity of this species. Remnants of the nitrogen from the initial condition are seen in the form of the small amount of nitrogen within and near the surface of the porous particle. The differences in the curvatures of the normalized species and temperature profiles at the surface result from the strong nonlinearity of the surface reaction rates.

The distribution of carbon conversion inside the particle is shown in Figure 2.53. The local conversion distribution is depicted for a total conversion of $X = 0.25$. Uniform conversion profile inside the particle is observed at low boundary temperature ($\sim 1200 \text{ K}$). Due to low temperature chemical kinetics are slower than diffusion and gases are able to penetrate inside the particle. With increase in the temperature ($\sim 1600 \text{ K}$), the gradients inside the particle become steeper resulting in concentrated conversion near the surface of the particle. At lower temperature the kinetics are much slower as compared to the diffusion rate. At higher temperature the kinetics are comparable to the diffusion rate. Therefore, the gaseous species are consumed near the surface of the particle and are unable to penetrate.

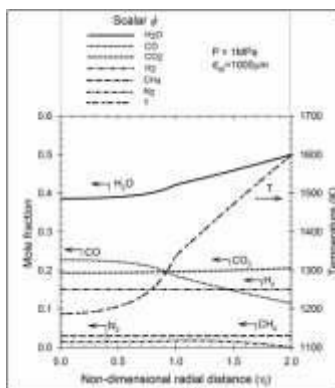


Figure 2.52: Scalar gradients inside and around the particle.

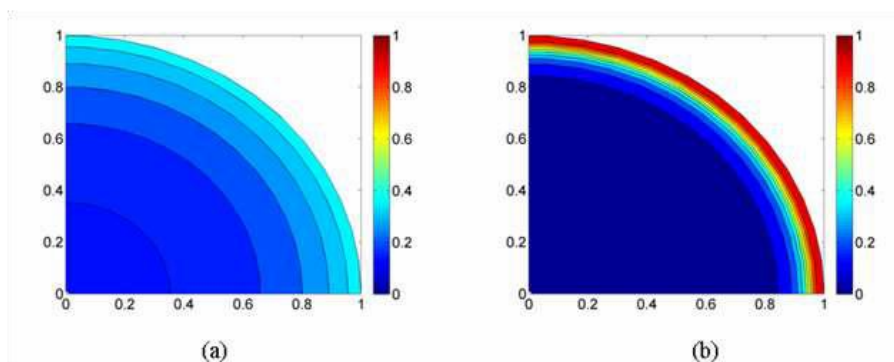


Figure 2.53: Effect of temperature on distribution of local carbon conversion.

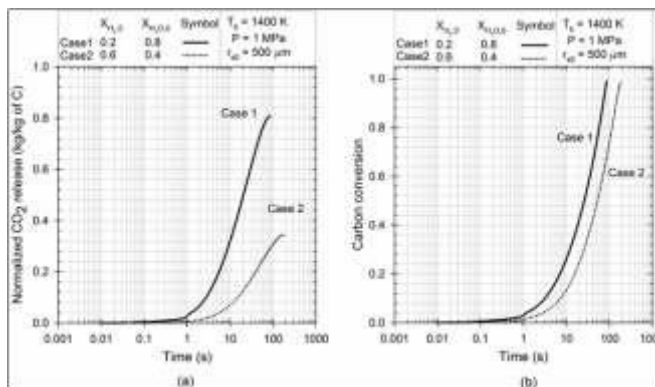


Figure 2.54: Effect of excess H₂ ($X_{H_2} = 0.2, 0.6$) on: (a) CO₂ release and (b) Carbon conversion with time.

The effects of external H₂ addition on the CO₂ production and the carbon conversion rates are shown in Figure 2.54 for a representative gasification temperature of 1400 K. The cumulative CO₂ produced per unit of C gasified decreases as the H₂ mole fraction in the gasifier is increased. Figure 7 (a) shows the mass of CO₂ produced per unit mass coal gasified as a function of time. As seen in figure, for 99% conversion with 0.2 H₂ mole fraction in steam, 0.8 units of CO₂ mass is produced from gasification of 1 unit mass of C. This is reduced by approximately 55% by increasing the mole fraction of H₂ in the gasifier from 0.2 to 0.6. Figure 7 (b) shows that the carbon conversion rate decreases and the total time for conversion increases by as much as a factor of 2 with the increased use of free stream H₂ from 0.2 to 0.6 mole fraction. Routine process engineering methods involving staging of the excess hydrogen can be used to overcome this challenge in addition to the previously recognized challenge of cost of hydrogen production using renewable energy sources.

The predictions from the particle scale model are found to be in good agreement with the experimental results of Everson et al.^[2,39]. From the parametric study it is found that gasification rate increases with increase in pressure and temperature. The gasification reaction is dominated by chemical kinetics at lower temperature and by diffusion of gaseous species at the higher temperatures. The species profiles near the particle surface and in the boundary layer emphasize the importance of steam as a gasifying medium and as an important species promoting the water gas shift reaction. The chemical reaction rates are balanced by the diffusion rates of reactant and product species. Uniform conversion profiles are observed inside the particle at lower temperature however concentrated higher conversions are observed near the particle surface with increased temperature. CO₂ emissions are found to decrease with excess H₂ addition but at the cost of decreased gasification rate.

2.4.2 Model for coal gasification processes in a well-stirred reactor with detailed gas-phase chemistry

The model has been described in great detail in Qiao et al.^[2,40]. Important findings from the paper are highlighted in the following section.

To theoretically understand the complex chemical processes in a gasifier and to identify the most influential parameters for syngas production, we developed a multiphysics model to simulate the gasification processes in a well-stirred reactor. This model is the first of its kind and considers detailed gas-phase chemistry, particle-phase reactions, radiative heat transfer, as well as full coupling between the two phases at various scales for mass, species, and energy exchange. The gas-phase reactions use the detailed chemistry GRI-Mech 1.2, including 177 elementary reactions and 31 species, as well as variable thermodynamic and transport properties. Four surface reactions were considered and the reaction rates were simulated by the diffusion-kinetics model with consideration of boundary layer diffusion. A random pore model was used to account for the evolution of the char porous structure and its impact on gasification rates. A numerical code was developed to solve the gas-phase and the particle-phase governing equations. Numerical simulations were conducted to understand the gasification process and the effects of particle size, porous structure, radiative heat transfer, pressure, O₂ concentration, and H₂ addition on gasification performance.

Carbon particles with diameter are uniformly distributed inside the reactor together with gaseous species as shown in Figure 2.55. The reactor's pressure remains constant, which means that during the gasification process the volume increases as a result of thermal expansion; thus the number density of coal particles decreases, but the total number is conserved. It is assumed that intense mixing occurs inside the reactor so that all gas-phase properties in the gas-phase bulk of the reactor, with the exception of the small boundary layers surrounding the particles, are uniform or spatially independent. As a result of this assumption, the temperature and number density of the particles can be assumed to be uniform at the bulk scale of the reactor. Mass, species, and energy exchanges between individual particles and surrounding gases cause local non-equilibrium in the boundary layers surrounding each of the particles. These interactions are modeled on the particle scale. Moreover, the model developed for a single particle represents all particles inside the reactor. For the gas-phase reactions, detailed kinetics and variable thermodynamic properties are considered. The governing equations of mass, species, and energy conservation for the gas phase and the particle phase are coupled to account for mass, species, and energy exchanges between the two phases. The transient gasification process is computed until 99% of the coal particle is gasified. Equal binary diffusion coefficients are considered applicable for multi-species diffusion and the bulk gas properties are modeled using ideal gas law.

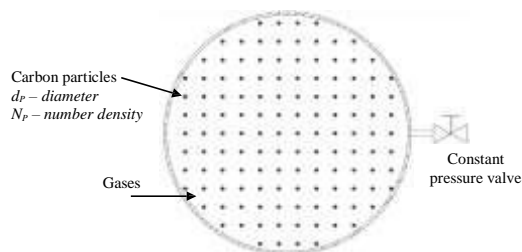


Figure 2.55: Coal gasification in a well-stirred reactor.

The present work adapted the Random Pore Model by imposing a factor into the gasification rate to capture the evolution of char pore formation during the gasification process. The governing equations are described in detail in

reference. Four heterogeneous reactions are assumed to take place on the particle surfaces. The surface reaction constants were expressed as Arrhenius rate laws. The gas-phase and particle-phase governing equations, which form a closed ODE system, were solved using FORTRAN package DASPK3.1^[2,41]. DASPK was designed to solve large-scale Differential-Algebraic Equation (DAE) systems. After the initial condition for every variable and the convergence criteria were specified, DASPK integrated the equations over time. The time step size and the order of temporal discretization were dynamically determined by the solver itself.

It was found that for steam gasification at lower temperature (~ 1200 K) in absence of oxygen, convective and radiative heat transfer plays a significant role in increasing the temperature of the particle. However, in the later stages the difference between the particle and gas temperature is negligible owing to the low rates of endothermic gasification reactions. The energy release from $\text{OH} + \text{H}_2 = \text{H} + \text{H}_2\text{O}$ reaction was found to be few magnitudes larger than that from the other 177 elementary gas phase reactions that were studied, indicating that it is the most influential elementary reaction in the gas phase. The water-gas-shift reaction ($\text{CO} + \text{H}_2\text{O} = \text{CO}_2 + \text{H}_2$) is often assumed to be at equilibrium in most modeling studies. To evaluate this assumption, we calculated the ratio $= X_{\text{CO}_2}X_{\text{H}_2}/(X_{\text{CO}}X_{\text{H}_2\text{O}})$ by using the simulation results (in equilibrium this ratio is equal to the equilibrium constant K_p), where the concentrations of H_2O , CO , H_2 , and CO_2 are obtained from the present detailed-chemistry calculations. The comparison in Figure 2.56 clearly shows that the ratio of concentrations is not equal to the K_p value over the entire time, indicating that the water-gas-shift reaction is not in equilibrium. The reason for the nonequilibrium might be the extreme temperature sensitivity of the elemental reactions at the relatively low temperatures (below 1200 K), as suggested by Gregg et al^[2,42].

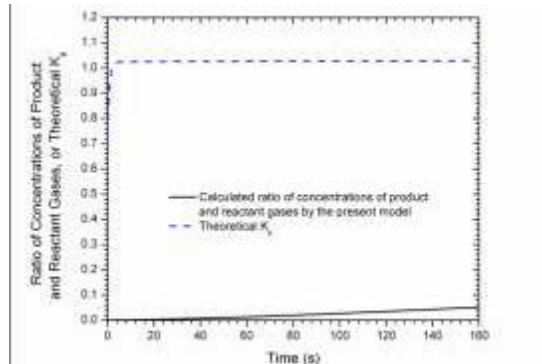


Figure 2.56: Computed ratio of concentrations of product and reactant gases and theoretical equilibrium constant of water-gas-shift reaction as a function of time for the basic case without O_2 . Computed ratios of concentrations are based on detailed chemistry calculations; theoretical K_p are calculated using the polynomial expression in Ref. [24]. Initial conditions are listed in Table 2.9.

Table 2.9: Initial conditions for a typical steam gasification process.

Initial gas temperature	$T_g = 1200 \text{ K}$	Initial particle temperature	$T_p = 1200 \text{ K}$
Wall temperature	$T_w = 1100 \text{ K}$	Density of particles	$\rho_p = 1.3 \text{ g/cm}^3$
Gas pressure	$P = 10 \text{ atm}$	Initial particle diameter	$d_p = 100 \text{ }\mu\text{m}$
Initial water concentration	$X_{\text{H}_2\text{O}} = 1.0$	Particle number density	$N_p = 896 \text{ cm}^{-3}$
Initial $\text{H}_2\text{O}/\text{C}$ molar ratio	$\text{H}_2\text{O}/\text{C} = 2.0$		

In case of gasification in presence of oxygen, it was found that the provided oxygen is consumed for the combustion of part of the carbon in the initial period. The heat energy that is released provides for the endothermic gasification reactions that ensue. The particle and gas temperatures increase rapidly to a maximum. During the initial period, particle temperature is found to be higher than the gas temperature, but is found to reduce during the rest of the gasification process. The peak temperatures occur at the instant of complete oxygen depletion. In the initial period, oxidation reactions of both the bulk gas phase and the particle surface and gas phase occur. Gas-phase oxidation

reactions mainly include the elementary steps $\text{OH} + \text{CO} = \text{H} + \text{CO}_2$, $\text{H} + \text{O}_2 + \text{H}_2\text{O} = \text{HO}_2 + \text{H}_2\text{O}$, $\text{OH} + \text{HO}_2 = \text{O}_2 + \text{H}_2\text{O}$, $\text{H} + \text{O}_2 = \text{O} + \text{OH}$, $\text{OH} + \text{H}_2 = \text{H} + \text{H}_2\text{O}$, $2\text{OH} = \text{O} + \text{H}_2\text{O}$ and $2\text{OH} + \text{M} = \text{H}_2\text{O}_2 + \text{M}$. The reaction rates of these seven steps are plotted as functions of time in Figure 2.57. The rates of the gas-phase reactions are much faster than those of the solid-gas reactions. After the oxygen is depleted, the carbon-steam reaction becomes dominant, with a rate about 10 or more times higher than the rates of $\text{C} + \text{CO}_2 \rightarrow 2\text{CO}$ and the $\text{C} + 2\text{H}_2 \rightarrow \text{CH}_4$ reactions.

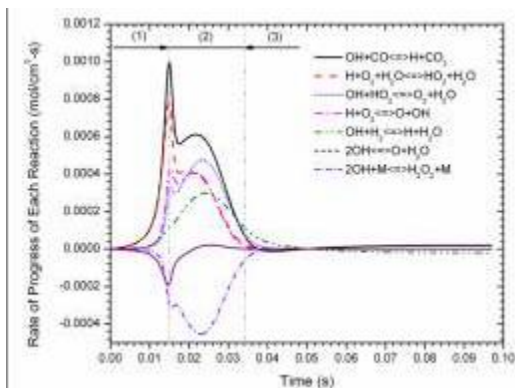


Figure 2.57: Profiles of rate of progress of main gas-phase elementary reactions for the basic case with O_2 .

Figure 2.58 shows the net production rates of five stable species as functions of time. The CO production rate from surface reactions is determined by reactions $2\text{C} + \text{O}_2 \rightarrow 2\text{CO}$, $\text{C} + \text{O}_2 \rightarrow \text{CO}_2$, $\text{C} + \text{H}_2\text{O} \rightarrow \text{CO} + \text{H}_2$, and $\text{C} + \text{CO}_2 \rightarrow 2\text{CO}$, especially the first three reactions. This explains the fact that the CO concentration versus time curve has a peak at $t = 0.025$ sec, which is between the peak of the O_2 curve ($t = 0.022$ sec) and the peak of the H_2O curve ($t = 0.028$ sec). CO_2 is first produced from the carbon oxidation reaction and then is consumed in reaction $\text{C} + \text{CO}_2 \rightarrow 2\text{CO}$ in gas-phase oxidation stage and carbon gasification stage.

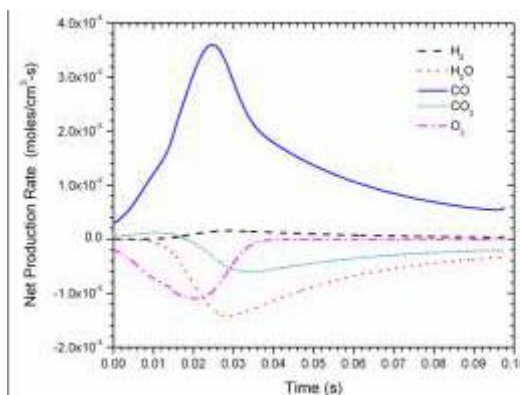


Figure 2.58: Net production rate of five species resulting from surface heterogeneous reactions for the basic case with O_2 .

The assumption of water gas shift equilibrium was evaluated for the case of gasification in presence of oxygen. The results are shown in Figure 2.59. It can be seen that the values have reasonable agreement in the later phases of the gasification process, indicating that the water-gas-shift reaction is at least near equilibrium state. This was not observed for the low temperature gasification case discussed earlier.

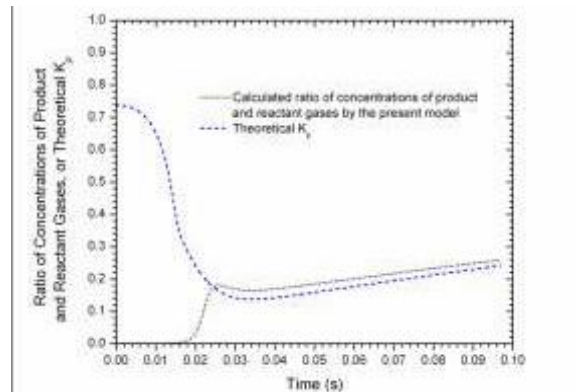


Figure 2.59: Computed ratio of concentrations of product and reactant gases and theoretical equilibrium constant of water-gas-shift reaction as a function of time for the basic case with O_2 .

Radiation was found to be an important mode of heat transfer. Similar effects of pressure and temperature were observed as discussed in the spatially resolved model. It was found that H_2 addition can increase syngas production (CO and H_2) and decrease CO_2 emissions by shifting the water gas reaction.

2.5 References

- [2.1] A. Williams, R. Backreedy, R. Habib, J. M. Jones, M. Pourkashanian., *Fuel*, 81(5) (2002) 605-618.
- [2.2] Niksa S., Liu G., Hurt R., *Progress in Energy and Combustion Science*, 30(6) (2004), 679-717.
- [2.3] Nola G. D., Jong W. de, Spliethoff, H., *Fuel Processing Technology*, 91 (2010), 103-115.
- [2.4] Hotchkiss, R., *Proceedings of the Institution of Mechanical Engineers*, 217(1) (2003), 27-33.
- [2.5] Guo X., Dai, Z, Gong X. et al., *Fuel Processing Technology*, 88(5) (2007), 451-459.
- [2.6] Minchener, A., *Fuel*, 84(17) (2005), 2222-2235.
- [2.7] Sircar, I., R. Gejji, A. Sane, D. Blunck, S. Meyer and J. P. Gore., *Proc. ASME/JSME 8th Thermal Engineering Joint Conference*, (2011), Honolulu, Hawaii.
- [2.8] Sircar, I., R. Gejji, A. Sane, D. Blunck, S. Meyer and J. P. Gore, *Proc. 49th AIAA Aerospace Sciences Meeting*, (2011), Orlando, Florida.
- [2.9] Gejji, R., A. Sane, B. Rankin, I. Sircar, S. Meyer and J. P. Gore, *Proc. 7th US National Combustion Meeting*, (2011), Atlanta, Georgia.
- [2.10] Sane, A., I. Sircar, R. Gejji, B. Rankin, D. Guildenbecher, S. Naik, R. Lucht and J. Gore, *2011 International Pittsburgh Coal Conference*, (2011), Pittsburgh, PA.
- [2.11] Zidwitz, P., Steinfeld, A., *Energy*, 28(5) (2003), 441-456.
- [2.12] Sane, A., Zheng, Y., Gore J., *Proceedings of the 6th U.S. National Combustion Meeting*, (2009), Ann Arbor, MI.
- [2.13] Qiao, L., J. Xu and J. P. Gore, *Proc. 49th AIAA Aerospace Sciences Meeting*, (2011), Orlando, Florida.

- [2.14] S. M. Abrarov, B. M. Quine, R. K. Jagpal, *Journal of Quantitative Spectroscopy and Radiative Transfer*, 111 (3) (2010), 372-375.
- [2.15] S. M. Abrarov, B. M. Quine, R. K. Jagpal, *Computer Physics Communications*, 181(5) (2010), 876-882.
- [2.16] R. K. Hanson, *Proceedings of the Combustion Institute*, 33 (1) (2011), 1-40.
- [2.17] H. Teichert, T. Fernholz, V. Ebert, *Applied Optics*, 42 (12) (2003), 2043-2051.
- [2.18] M. Lackner, G. Totschnig, G. Loeffler, H. Hofbauer, F. Winter, *Thermal Science*, 6 (2) (2002), 13-27.
- [2.19] M. Lackner, *Fuel*, 83 (10) (2004), 1289-1298.
- [2.20] V. Nagali, J. T. Herbon, D. C. Horning, D. F. Davidson, R. K. Hanson, *Appl. Opt.*, 38(33) (1999), 6942-6950.
- [2.21] H. Li, G. B. Rieker, X. Liu, J. B. Jeffries, R. K. Hanson, *Appl. Opt.*, 45(5) (2006), 1052-1061.
- [2.22] B. L. Upschulte, D. M. Sonnenfroh, M. G. Allen, *Appl. Opt.*, 38(9) (1999), 1506-1512.
- [2.23] J. Wang; M. Maiorov, D. S. Baer, D. Z. Garbuzov, J. C. Connolly, R. K. Hanson, *Appl. Opt.*, 39(30) (2000), 5579-5589.
- [2.24] G. Repas, (1994), NASA TM 106493.
- [2.25] E. Dambach, D. Helderma., A. Boopalan, T. Kite, Purdue University Internal Report, (2006), West Lafayette, IN.
- [2.26] A. Boopalan, D. Helderma, Purdue University Internal Report, (2006), West Lafayette, IN.
- [2.27] Farias L., Irons G., *Metallurgical and Materials Transactions B*, 17(1) (1986), 229-231.
- [2.28] Ragland, K. W., Aerts, D. J., *Bioresource Technology*, 37 (1991), 161-168.
- [2.29] Dutta, S., Wen, C. Y., *Ind. Eng. Chem Process Des. Dev.*, 16(1) (1977), 31-37.
- [2.30] Gupta, R., *Energy & Fuels*, 21 (2007), 451-460.
- [2.31] Bridgewater, A.V. Boocock, D.G.B. (eds). *Developments in Thermochemical biomass Conversion*. London: Chapman & Hall, 2 (1997), 830.
- [2.32] B. Srinivas, N. R. Amundson, *AIChE Journal*, 26(3) (1980), 487-496.
- [2.33] S. Dutta, C. Y. Wen, R. J. Belt, *Industrial & Engineering Chemistry Process Design and Development*, 16(1) (1977), 20-30.
- [2.34] K. Heden, A. Löwe, *Carbon*, 5(4) (1967), 339-353.
- [2.35] J. Blackwood, *Australian Journal of Chemistry*, 12(1) (1959), 14-28.
- [2.36] C. Y. Wen, T. Z. Chaung, *Industrial & Engineering Chemistry Process Design and Development*, 18(4) (1979), 684-695.
- [2.37] P. Gupta, A. K. Sadhukhan, R. K. Saha, *International Journal of Chemical Kinetics*, 39(6) (2007), 307-319.

- [2.38] S. Patankar, *Numerical fluid flow and heat transfer*, Hemisphere Publications, 1980.
- [2.39] R. C. Everson, H. W. J. P. Neomagus, H. Kasaini, D. Njapha, *Fuel*, 85(7-8) (2006), 1076-1082.
- [2.40] Qiao, L, Xu, J., Sane, A., Gore, J., *Combustion and Flame*, 159(4) (2012), 1693-1707.
- [2.41] Petzold, L. R., *A description of DASSL: A differential/algebraic system solver in scientific computing*, (1983), North-Holland, Amsterdam: Stepleman, R. S. et al. (Eds.), 65-68.
- [2.42] Gregg, D. W., W. R. Aiman, H. H. Otsuki, C. B. Thorsness, *Solar Energy*, 24(3) (1980), 313-321.

3.0 Conclusions

Biomass Fast-Hydropyrolysis

- (1) Heating rate is a very critical parameter that determines the char yield from cellulose. Increasing pyrolysis heating rate decreased the char yield. Heating rates on the order of $1,000\text{ }^{\circ}\text{C s}^{-1}$ were sufficient to eliminate the formation of char from cellulose, regardless of the gas atmosphere.
- (2) For the micro-scale batch reactor, two different designs of a downstream catalytic reactor were tested and evaluated. The design based on a fixed-bed reactor was more robust and gave us more flexibility in conducting HDO/WGS studies than a capillary reactor design.
- (3) The high-pressure continuous FHP was designed, built and successfully tested in a high-pressure hydrogen atmosphere and in the presence of candidate HDO/WGS catalysts in the downstream fixed-bed catalytic reactor.
- (4) In the absence of catalyst during pyrolysis of cellulose, hydrogen does not affect the liquid product composition on a qualitative basis.
- (5) The presence of a $\text{H}_2/\text{CO}/\text{CO}_2$ mixture in the pyrolysis region did not qualitatively affect the primary products of cellulose hydropyrolysis.
- (6) Pt metal in the hydropyrolysis region was found to be active for HDO of hydropyrolysis vapors of cellulose
- (7) A WGS catalyst, 2% Pt/ Al_2O_3 , was found to be active for HDO of hydropyrolysis vapors of cellulose in the downstream HDO conditions.
- (8) Comparison of the 2% Pt/ Al_2O_3 catalyst to pure Al_2O_3 showed that a balance between acid function on the Al_2O_3 and hydrodeoxygenation on the Pt metal function is needed to optimize dehydration, deoxygenation, and coking in the HDO reactor.

Investigation of Coal and Biomass Gasification using in-situ Diagnostics

- (1) A unique, laboratory scale, continuous-flow, high-pressure, high-temperature and optically accessible gasifier arrangement has been designed and assembled. The gasifier arrangement consists of a novel steam-generator, a high-pressure powder feeder and optical accessibility for in-situ diagnostics along the reactor length. Operation of the gasifier arrangement at the design pressure and temperature conditions has been demonstrated.
- (2) Gasification of a coconut-based char and anthracite coal has been demonstrated at a temperature of 1100 K and 1 MPa. Gas-phase carbon species (in the form of CH_4 , CO, and CO_2) have been measured using product gas sampling and analysis.
- (3) A fixed-bed gasifier has been developed, assembled and demonstrated. Optical access within the fixed-bed gasifier enables in-situ diagnostics in a highly controlled setting. Gasification of pinewood biomass in CO_2 has been successfully demonstrated and repeated. Product gas analysis and solid mass balance has indicated

up to 80% conversion of the original feedstock. The next steps include gasification in a high-pressure environment and gasification in the presence of solid catalysts.

- (4) Micro-structural analysis combined with x-ray characterization techniques have shown to provide valuable insight into the structural and chemical evolution of the feedstock during gasification. Systematic analysis into the formation of the micropores and will be conducted in subsequent studies and contribute to heterogeneous chemistry modeling.
- (5) In-situ diagnostics have been demonstrated via the use of TDLAS for the measurement of CO concentrations. Product gas sample composition and in-situ TDLAS measurements have been compared and show qualitative correlation. Future work will include the demonstration of the TDLAS method in the particle-laden continuous flow arrangement, where scattering of the signal off of particles is an additional challenge.
- (6) Mathematical modeling of the coal gasification process has shown that carbon conversion is highly sensitive to the operating temperature.
- (7) The models show that the assumption of constant diffusivity for all gas-phase species, especially when H₂ is present, tends to over-predict the carbon conversion rates. Differential diffusivity models represents the gasification process more accurately.
- (8) The addition of H₂ as a gasification reactant, via partial recirculation of the product gases, can inhibit CO₂ formation via the water-gas-shift-reaction. However, H₂ also interferes with the gasification reaction rate and reduces the rate of carbon conversion.
- (9) The water-gas-shift reaction is not in equilibrium for the steam gasification process. The water-gash-shift equilibrium assumption is more accurate for the high-temperature gasification process with the addition of O₂ as a reactant.

4.0 Participating Personnel

Biomass Fast-Hydropyrolysis: School of Chemical Engineering

1. Rakesh Agrawal, Professor, PI. Oversaw and participated in all aspects of the research related to biomass hydropyrolysis and provided the overall vision for a sustainable transportation fuel economy.
2. Fabio H. Ribeiro, Professor, participating investigator. Participated in design and oversaw construction and operation of all equipment, participated in design and interpretation of all experiments.
3. W. Nicholas Delgass, Professor, participating investigator. Participated in design of equipment and design and interpretation of all experiments.
4. Andrew Smeltz, Lead Research Engineer. Oversaw and helped design, build and operate all experimental apparatuses, responsible for compiling research reports from group members.
5. Fernando Resende, Post-Doctoral Research Associate. Helped design and operate continuous low pressure pyrolysis unit used for visualization studies.
6. Jun Wang, Post-Doctoral Research Associate. Built and operated continuous optically-accessible pyrolysis reactor used for visualization studies.
7. Dharik Mallapragada, Graduate Student. Performed overall process calculations to support the experimental studies.

8. Piotr Gawecki, Graduate Student. Designed, built, and operated micro batch pyrolysis reactor used for visualization studies.
9. Navneet Singh, Graduate Student. Performed overall process calculations that established the research direction and led to motivation for the experimental studies.
10. Harshavardhan Choudhari, Graduate Student. Helped design, build, and operate micro-scale batch fast-hydropyrolysis and fixed bed catalytic reactor and compiled data for reporting.
11. Viktor Cybulskis, Graduate Student (Summer Research). Helped design, build, and operate decoking apparatus used for char formation studies and compiled data for reporting.
12. Vinod K. Venkatakrishnan, Graduate Student. Helped design, build and operate continuous high-pressure fast-hydropyrolysis and fixed-bed catalytic reactor and compiled data for reporting.
13. Yury Zvinevich, Director of the Advanced Spectroscopic Facility. Helped design and build all apparatuses used in this study.

Investigation of Coal and Biomass Gasification using in-situ Diagnostics: School of Mechanical Engineering and School of Aeronautical and Astronautical Engineering

1. Jay Gore, Professor, Co-PI. Oversaw and participate in all aspects of the research related to the optically accessible gasifier and flame structure studies. Provided overall coordination and support across the project.
2. Robert Lucht, Professor, participating investigator. Oversaw the design, construction and operation of the counter flow burner experiment for flame structure studies. Provided expertise in design of experiment for optical diagnostics for gasifier.
3. Li Qiao, Assistant Professor, participating investigator. Oversaw the computational work related to flame structure studies. Provided her expertise related to coal gasifier modeling.
4. Scott Meyer, Operational director, Maurice J. Zucrow Laboratories. Oversaw the design and construction of the gasifier experimental apparatus and laboratory infrastructure.
5. Sameer V. Naik, Visiting Assistant Professor. Participated in design and operation of experiment for flame structure studies. Provided his expertise in design of experiment for optical diagnostics of gasifier.
6. Anup Sane, Graduate Student. Performed overall process calculations that established the research direction, led the design process of the high pressure particle feeder and optical diagnostics system, responsible for compiling research reports from group members.
7. Indraneel Sircar, Graduate Student. Led the design of the reactor vessel, support structure, and control and diagnostics systems for the gasifier arrangement, responsible for product gas analysis, post-gasified material characterization and compiling research reports from group members.
8. Jian Xu, Graduate Student. Performed the computational work on the multiphysics modeling of carbon gasification process using detailed chemistry.
9. Rohan Gejji, Graduate Student. Led the design and manufacture of the chemical steam generator and the assembly process of the optically accessible gasifier arrangement for gasifier.
10. David Blunck, Former Graduate Student (now at AFRL, Dayton, OH). Oversaw and participate in the design process of gasifier arrangement, worked as a project coordinator.
11. Aman Satija, Graduate Student. Performed experimental work for flame structure studies.

12. Deepti Singh, Graduate Student. Performed premixed flame speed measurements and computations for alternative fuels.
13. Devashish Bangar, former Undergraduate Student (now Graduate Student). Learned laboratory practices and helped with experimental arrangements.
14. Yahui Wang, Undergraduate Student (Summer-Undergraduate-Research-Foundation Fellow). Performed detailed calibration of the powder feeder with various feed-stocks at high pressure and improved the flow-ability of various feeds-tocks through design iterations on the powder feeder.
15. Hao Wu, Undergraduate Student (Summer-Undergraduate-Research-Foundation Fellow). Performed detailed plug-flow reactor simulations on Ansys Fluent to aid with the development of the experimental apparatus, aid with selection of feed-stock, and solve process problems.
16. Zexi Xu, Undergraduate Student (Summer-Undergraduate-Research-Foundation Fellow). Learned the theory behind laser-absorption-spectroscopy and helped arrange and calibrate the initial diode-laser for water-vapor measurements.
17. Sameer Patel, Visiting Assistant Scholar. Learned about coal and biomass gasification, provided help in arranging experimental apparatus, and helped with multi-specie, multi-diffusion single particle gasification modeling.
18. Christine S. LaBelle, Undergraduate Student. Provided hands-on help in the laboratory.

5.0 Publications and Presentations

5.1 Publications

Published

- [1] Agrawal, R., Singh, N. R., 2010, "Solar Energy to Biofuels," Annual Review of Chemical and Biomolecular Engineering, **1**, pp. 343-364.
- [2] Singh, N. R., Delgass, W. N., Ribeiro, F. H., Agrawal, R., 2010, "Estimation of Liquid Fuel Yields from Biomass," Environmental Science and Technology, **44**(13), pp. 5298-5305.
- [3] Qiao, L., Xu, J., Sane, A., Gore, J. P., 2012, "Multiphysics modeling of carbon gasification processes in a well-stirred reactor with detailed gas-phase chemistry," Combustion and Flame, **159**(4), pp. 1693-1707.

In Progress

- [4] Singh, N. R., Mallapragada, D. S., Agrawal, R., Tyner, W. E., "Economic Analysis of Novel Synergistic Biofuel (H₂Bioil) Processes," Submitted for publication to Biomass Conversion & Biorefinery.
- [5] Gawecki, P., Smeltz, A. D., Hurt, M. R., Borton II, D. J., Vinueza, N. R., Nugent, N. J., Agrawal, R., Delgass, W. N., Kenttämä, H. I., Anderson, W. E., Ribeiro, F. H., "Direct Production of Molecules in the Fuel Range by Selective Tailoring of Biomass Fast Pyrolysis," (In Preparation).
- [6] Sane, A., Sircar, I., Gore, J. P., "A Study of Biomass Gasification with Hot CO₂, Steam and Excess Hydrogen, Proceedings of the 34th International Symposium on Combustion, (In Review).

5.2 Conference Papers and Presentations

- [1] "Energy Solutions for a Fossil Fuel Deprived Future", Rakesh Agrawal, Andlinger Energy Lecture, Princeton University, Princeton, February 2009.
- [2] "Transportation Fuel in a Fossil Fuel Free world", Rakesh Agrawal, Renewable Energy World 2009, Las Vegas, March 2009.
- [3] "Sustainable Energy Utilization and Transformation", Rakesh Agrawal, George W. Woodruff School of Mechanical Engineering's Sustainable Energy Pathways and Solutions Workshop, Georgia Tech., Atlanta, April 2009.
- [4] "Synergistic Processes for Biofuels", Rakesh Agrawal, Purdue Biofuels Symposium, West Lafayette, In, May 2009.
- [5] "A Study of Steam Gasification of Coal with CO₂ Control using H₂", Sane, A., Zheng, Y., and Gore, J. P., Proc. 6th US National Combustion Meeting, Ann Arbor, MI, May 2009.
- [6] "Transportation Fuel in a Solar Economy", Rakesh Agrawal, Keynote Lecture, FOCAPD, Breckenridge, Co, June 2009.
- [7] "Synergistic Processes for Biofuels", Rakesh Agrawal, Plenary Lunch Lecture, BioFuels Conference- The Next Generation of Biofuels, Mississippi State University, Jackson, MS, August 2009.
- [8] "Energy Solutions for a Fossil Fuel Deprived Future", Rakesh Agrawal, Pioneers in Energy Lecture, Purdue University, West Lafayette, IN, September 2009.
- [9] "More Liquid Fuel from Biomass", Rakesh Agrawal, Indo-US Workshop on Climate and Energy Futures, Chennai, India, October 2009.
- [10] "Transportation Fuel Solutions Using Renewable Energy", Rakesh Agrawal, RTI Fellows Symposium, RTI International, Research Triangle Park, NC, November 2009.
- [11] "Solar Based Sustainable Energy Solutions", Rakesh Agrawal, Maddox Solar Energy Series, Whitacre College of Engineering at Texas Tech University, February 2010.
- [12] "Solar Based Sustainable Energy Solutions", Rakesh Agrawal, Plenary Lecture, 2nd International Symposium on Sustainable Chemical Product and Process Design (ISSCPPE), Hangzhou, China, May 2010.
- [13] "Coal and Biomass to Liquid Fuel Synthesis for Aerospace Engines," Anup Sane, Rohan Gejji, and Indraneel Sircar, Poster Presentation, 5th Annual Frontiers in Bioenergy Symposium, Purdue University, West Lafayette, IN, May 2010.
- [14] "Transportation Fuel Solutions using Renewable Energy", Dharik Mallapragada, EPFL, Lausanne, Switzerland, September 2010.
- [15] "Chemical Engineering in a Solar Energy Driven Sustainable Future", Rakesh Agrawal, PPG Foundation Keynote Address, 32nd Annual Chemical Engineering Graduate Student Association Symposium, Carnegie Mellon University, Pittsburgh, PA, October, 2010.
- [16] "Solar Based Sustainable Energy Solutions", Rakesh Agrawal, Pirkey Lecture, University of Texas, Austin, TX, November 2010.

- [17] "Solar Based Sustainable Energy Solutions", Rakesh Agrawal, Invited keynote address, AIChE annual meeting, Salt Lake City, UT, Nov 2010.
- [18] "Design and Construction of an Optically-Accessible Coal Gasifier for CO₂ Reduction using Excess H₂," Sircar, I., Gejji, R., Sane, A., Blunck, D., Meyer, S., and Gore, J. P., Proc. 49th AIAA Aerospace Sciences Meeting, Orlando, FL, January 2011.
- [19] "Multiphysics Modeling of Coal Gasification Processes in a Perfectly-stirred Reactor with Detailed Gas-Phase Chemistry," L. Qiao, J. Xu, A. Sane, J. Gore, Proc. 49th AIAA Aerospace Sciences Meeting, Orlando, FL, January 2011.
- [20] "Transportation Fuel Solutions Using Solar Energy", Rakesh Agrawal, Helmholtz-Zentrum Berlin für Materialien und Energie, Berlin, Feb 2011.
- [21] "Coal Gasification and its Impact on Domestic Energy Security," Indraneel Sircar, Poster Presentation, 2011 Next Generation Scholars, Purdue University, West Lafayette, IN, February 2011.
- [22] "Chemical Engineering in a Solar Energy Driven Sustainable Future", Rakesh Agrawal, IIT Kanpur, March 2011.
- [23] "An experimental study of a superheated H₂-O₂ steam generator," Gejji, R., Sane, A., Rankin, B., Sircar, I., Meyer, S., and Gore, J. P., Proc. 7th US Joint Combustion Meeting of the Combustion Institute, Georgia Institute of Technology, Atlanta, GA, March 2011.
- [24] "Multiphysics Modeling of Coal Gasification Processes in a Perfectly-stirred Reactor with Detailed Gas-Phase Chemistry," L. Qiao, J. Xu, A. Sane, J. Gore, Proc. 7th US Joint Combustion Meeting of the Combustion Institute, Georgia Institute of Technology, Atlanta, GA, March 2011.
- [25] "Design and Testing of a High Pressure and Temperature, Optically Accessible, Entrained Flow Coal Gasifier," Sircar, I., Gejji, R., Sane, A., Blunck, D., Meyer, S., and Gore, J. P., Proc. ASME/JSME 8th Thermal Engineering Joint Conference, Honolulu, HI, March 2011.
- [26] "Chemical Engineering in a Solar Energy Driven Sustainable Future", Rakesh Agrawal, Hugh M. Hulburt Memorial Lecture, Northwestern University, Evanston, IL, April 2011.
- [27] "Energy Systems Analysis for a Renewable Transportation Sector", Rakesh Agrawal, Navneet R. Singh and Dharik S. Mallapragada, Proceedings 21st European Symposium on Computer Aided Process Engineering-ESCAPE-21, Porto Carras, Chalkidiki, Greece, May 2011
- [28] "Catalytic Hydropyrolysis – it Really is Rocket Science", Fabio H. Ribeiro, 6th Frontiers in Bioenergy: United States-Brazil Symposium on Sustainable Bioenergy, West Lafayette, IN, May 2011.
- [29] "Optically Accessible Entrained Flow Steam Gasifier," Indraneel Sircar and Anup Sane, Invited Presentation, NETL Multiphase Flow Workshop, Coraopolis, PA, August 2011.
- [30] "Direct Production of Molecules in the Fuel Range by Selective Tailoring of Biomass Fast Pyrolysis", Fabio H. Ribeiro, Piotr Gawecki, W. Nicholas Delgass, Rakesh Agrawal, Andrew Smeltz, Matthew R. Hurt, David J. Borton II, Nelson R. Vinuesa, Hilkka I. Kenttamaa, Nicholas J. Nugent and William E. Anderson, IDECAT/JCAT Conference on Catalysis, Bertinoro, Italy, September 2011.
- [31] "Tunable Diode Laser Absorption Diagnostics and Gas Composition Analysis of Reaction Progress in a Laboratory-Scale Entrained-Flow Gasifier," Sane, A., Sircar, I., R., G., Rankin, B., Guildenbecher, D., Naik, S., Lucht, R., and Gore, J., 2011 International Pittsburgh Coal Conference, Pittsburgh, PA, September 2011.

- [32] “Optically Accessible, Entrained-Flow, Steam Drive Coal and Biomass Gasifier,” Indraneel Sircar and Anup Sane, Poster Presentation, Shell Energy Day, Purdue University, West Lafayette, IN, September 2011.
- [33] “Optically Accessible, Entrained-Flow, Steam Drive Coal and Biomass Gasifier,” Indraneel Sircar and Anup Sane, Poster Presentation, China-US 2011 Joint Symposium: Prospects and Challenges of Growing the Biology Based Economy, Purdue University, West Lafayette, IN, September 2011.
- [34] “Chemical Engineering in a Solar Energy Driven Sustainable Future”, Rakesh Agrawal, Hess Lecture, Department of Chemical Engineering, University of Virginia, October 2011.
- [35] “Chemical Engineering Innovation Needs for a Future Solar Economy”, Rakesh Agrawal, Plenary Lecture, 61st Canadian Chemical Engineering Conference, London, Ontario, Canada, October 2011.
- [36] “Novel Pathways for Biomass-to-Liquid Fuel Production”, Rakesh Agrawal, In session honoring Professor Santosh K. Gupta, AIChE Annual Meeting, Minneapolis, MN, October 2011.
- [37] “High-Pressure Fast-Pyrolysis and Fast-Hydropyrolysis for Conversion of Biomass to Liquid Fuels”, Vinod K. Venkatakrishnan, Andrew Smeltz, Sergey Semikolenov, Fabio H. Ribeiro, W. Nicholas Delgass, Rakesh Agrawal, AIChE Annual Meeting, Minneapolis, MN, October 2011.
- [38] “Direct Production of Molecules in the Fuel Range by Selective Tailoring of Biomass Fast Pyrolysis”, Piotr Gawecki, Fabio H. Ribeiro, W. Nicholas Delgass, Rakesh Agrawal, Andrew Smeltz, Matthew R. Hurt, David J. Borton II, Nelson R. Vinueza, Hilkka I. Kenttamaa, Nicholas J. Nugent and William E. Anderson, AIChE Annual Meeting, Minneapolis, MN, October 2011.
- [39] “Multiphysics Modeling of Coal Gasification Processes in a Perfectly-stirred Reactor with Detailed Gas-Phase Chemistry,” L. Qiao, J. Xu, A. Sane, J. Gore, Fall Technical Meeting, Western States Section of the Combustion Institute, University of Riverside, CA, October 2011.
- [40] “Multiphysics Modeling of Coal Gasification Processes in a Perfectly-stirred Reactor with Detailed Gas-Phase Chemistry,” L. Qiao, J. Xu, A. Sane, J. Gore, Fall Technical Meeting, Eastern States Section of the Combustion Institute, University of Connecticut, CT, October 2011.
- [41] “Novel Pathways for Biomass-to-Liquid Fuel Production”, Rakesh Agrawal, Plenary Lecture, 6th Sino/US joint conference, Beijing, China, November 2011.
- [42] “Optically Accessible, Entrained-Flow, Steam Drive Coal and Biomass Gasifier,” Indraneel Sircar, Poster Presentation, Ecological Sciences and Engineering Symposium: 7 Billion People – 7 Grand Challenges, Purdue University, West Lafayette, IN, November 2011 (Awarded 2nd place).
- [43] “An Experimental Study of a H₂-O₂ Flame based Superheated Steam Generator for Coal Gasification”, Gejji, R., Sane, A., Sircar, I., Rankin, B., Meyer, S., and Gore, J.P., 2012, 50th AIAA 2012 Aerospace Sciences Meeting, January 2012.
- [44] “A Study of Biomass Gasification with Hot CO₂, Steam and Excess Hydrogen,” Sane, A., Sircar, I., Gore, J. P., Submitted for the 34th International Symposium on Combustion, Jul 29 – Aug 3, 2012.

Conference Papers Indirectly Supported by the AFOSR Grant

- [45] “Dual-pump CARS measurements in a gas turbine combustor facility using the NASA 9-point lean direct injector,” Thariyan, M. P., Bhuiyan, A. H., Chai, N., Naik, S. V., Lucht, R. P., and Gore, J. P., Proc. 48th AIAA Aerospace Sciences Meeting and Exhibit, Orlando, FL, January 2011.

- [46] "Temperature and CO₂ measurements in a high-pressure, lean direct injector combustor using dual-pump CARS," Thariyan, M. P., Bhuiyan, A. H., Naik, S. V., Gore, J. P., and Lucht, R. P., Proc. Spring Technical Meeting of Central States Section of the U. S. Sections of the Combustion Institute, Champaign, IL, March 2010.
- [47] "Dual-pump CARS and OH-PLIF measurements at elevated pressures in a gas turbine combustor facility," Thariyan, M. P., Bhuiyan, A. H., Naik, S. V., Gore, J. P., and Lucht, R. P., Proc. 27th AIAA Aerodynamic Measurement Technology and Ground Testing Conference, Chicago, IL, June 2010.
- [48] "Characterization of methane-air and hydrogen-air flames using stereoscopic particle imaging velocimetry (SPIV) and coherent anti-Stokes Raman scattering (CARS)," Satija, A., Panda, P., Wagh, Y., Naik, S. V., Gore, J.P., and Lucht, R. P., Proc. 7th Joint Meeting of the U.S. Sections of the Combustion Institute, Atlanta, GA, March 2011.
- [49] "Temperature and CO₂ measurements in a high-pressure, lean direct injector combustor using dual-pump CARS," Thariyan, M. P., Bhuiyan, A. H., Naik, S. V., Gore, J. P., and Lucht, R. P., Proc. 7th Joint Meeting of the U.S. Sections of the Combustion Institute, Atlanta, GA, March 2011.